

MASSES, RADII, AND DENSITIES OF 52 PLANETS FROM *KEPLER* [†]

GEOFFREY W. MARCY¹, HOWARD ISAACSON¹, JASON F. ROWE², JON M. JENKINS³, STEPHEN T. BRYSON², STEVE B. HOWELL², NATALIE M. BATALHA², DAVID W. LATHAM⁸, LESLIE ROGERS²², THOMAS N. GAUTIER III⁶, DAVID CIARDI¹⁴, DEBRA A. FISCHER¹⁹, RONALD L. GILLILAND¹⁰, HANS KJELDSSEN¹², JØRGEN CHRISTENSEN-DALSGAARD^{12,13}, DANIEL HUBER², BILL CHAPLIN⁴¹, SARBANI BASU¹⁹, LARS A. BUCHHAVE¹¹, SAMUEL N. QUINN⁸, WILLIAM J. BORUCKI², DAVID G. KOCH², ROGER HUNTER², DOUGLAS A. CALDWELL³, JEFFREY VAN CLEVE³, ANDREW W. HOWARD²⁹, REA KOLBL¹, LAUREN M. WEISS¹, SARA SEAGER¹⁶, TIMOTHY MORTON²², JOHN ASHER JOHNSON²², SARAH BALLARD²⁹, CHRIS BURKE³, WILLIAM D. COCHRAN⁷, MICHAEL ENDL⁷, MARK E. EVERETT³⁵, JACK J. LISSAUER², ERIC B. FORD²⁰, GUILLERMO TORRES⁸, FRANCOIS FRESSIN⁸, TIMOTHY M. BROWN⁹, JASON H. STEFFEN¹⁷, DAVID CHARBONNEAU⁸, GIBOR S. BASRI¹, DIMITAR D. SASSELOV⁸, JOSHUA WINN¹⁶, JESSIE CHRISTIANSEN², ELIZABETH ADAMS⁸, ANDREA DUPREE⁸, DANIEL C. FABRYCKY¹⁸, JONATHAN J. FORTNEY¹⁸, JILL TARTER³, MATTHEW J. HOLMAN⁸, PETER TENENBAUM³, AVI SHPORER^{9,23}, PHILIP W. LUCAS²⁴, WILLIAM F. WELSH²⁵, JEROME A. OROSZ²⁵, ALAN BOSS²⁶, EDNA DEVORE³, ALAN GOULD²⁷, ANDREJ PRSA²⁸, ERIC AGOL²⁹, THOMAS BARCLAY³¹, JEFF COUGHLIN³¹, ERIK BRUGAMYER³³, CHRISTOPHER HENZE², FERGAL MULLALLY³, ELISA V. QUINTANA³, AVI SHPORER^{22,39}, MARTIN STILL³¹, SUSAN E. THOMPSON³, DAVID MORRISON², JOSEPH D. TWICKEN³, JEAN-MICHEL DÉSERT⁸, JOSH CARTER²⁰, JUSTIN R. CREPP³⁴, GUILLAUME HÉBRARD^{42,43}, ALEXANDRE SANTERNE^{44,45}, CLAIRE MOUTOU⁴⁴, CHARLIE SOBECK², DOUGLAS HUDGINS⁴⁶, MICHAEL R. HAAS²,

Draft version May 28, 2013

ABSTRACT

We report multiple Doppler shift measurements, spanning four years, of 22 *Kepler* Objects of Interest (KOIs) that host 52 candidate planets, 42 of which transit the host star, with most being smaller than 3× the size of Earth. We combine the Doppler measurements with the *Kepler* brightness measurements of the host stars during planet transits to constrain the masses, radii, and orbits of the 42 planets. High resolution optical spectroscopy of the 22 host stars, combined with stellar evolution models, and seismology analysis for 11 of them, yield accurate stellar radii and masses to yield precise planet properties. Among the 42 *Kepler* transiting planet candidates, eight are identified here for the first time from *Kepler* photometry. For 15 KOIs, the Doppler measurements exhibit periodicities having the same period and orbital phase as revealed by the planet-transit light curve, providing both support for the existence of the planet and a measurement of the planet’s mass. For the remaining planets we provide either marginal mass constraints (under 2-sigma) or upper limits to their masses and densities, often ruling out a solid rock interior. We assess the probability of false positives for each planet candidate by using a model of the Milky Way Galaxy including binary star occurrence, bolstered by a suite of observational diagnostics including a spectroscopic search for neighboring stars, adaptive optics, speckle interferometry, light curve analysis, and astrometric displacements in and out of transit (centroids). The resulting false positive probability is less than 1% for all but two of the planets, namely KOI-104 and KOI-1612. For KOI-104, its RV periodicity is consistent with the transit-based orbit, rendering it also likely to be a real transiting planet. This false-positive analysis suggests that all but one of the 52 candidates are highly likely to be real planets. For the multi-planet systems, false positives are even less likely, due to the improbable spatial alignment of a star having a real transiting planet with a fake-planet scenario. The masses, radii, and incident stellar fluxes of the planets are correlated, yielding statistical Mass-Radius relations. None of the planets above 2.0 Earth-radii have high enough densities to have purely solid interiors. Similarly, the planets with densities above 6 g/cc, and hence plausible rocky, all have radii below 2 R_{\oplus} . *Thus, rocky planets have radii predominantly less than twice the size of Earth.* However, some planets smaller than twice that of Earth have densities lower than 5 g cm⁻³, implying significant amounts of low density material, presumably hydrogen, helium, and/or water. Considering the ensemble of planets, increasing masses are associated with decreasing densities, in agreement with Weiss et al. (2013). This decrease in planet density with increasing planet mass implies that planet interiors typically contain more low density material (H, He, and/or water) with increasing mass, shedding light on planet formation physics.

Subject headings: planetary systems — stars: individual (*Kepler*) — techniques: photometry, radial velocity

¹ University of California, Berkeley, CA 94720

² NASA Ames Research Center, Moffett Field, CA 94035

³ SETI Institute/NASA Ames Research Center, Moffett Field, CA 94035

⁴ San Jose State University, San Jose, CA 95192

⁵ Lowell Observatory, Flagstaff, AZ 86001

⁶ Jet Propulsion Laboratory/Caltech, Pasadena, CA 91109

⁷ University of Texas, Austin, TX 78712

⁸ Harvard-Smithsonian Center for Astrophysics, 60 Garden Street, Cambridge, MA 02138

⁹ Las Cumbres Observatory Global Telescope, Goleta, CA 93117

¹⁰ Center for Exoplanets and Habitable Worlds, The Pennsylvania State University, University Park, 16802

¹¹ Niels Bohr Institute, Copenhagen University, Denmark

1. INTRODUCTION

Our Solar System contains no planets with sizes between 1.0 and $3.8 R_{\oplus}$, bracketed by Earth and Uranus, a size gap that offers a clue about the conditions and processes of planet formation. Even Uranus and Neptune with sizes $3.8\text{-}4.0 R_{\oplus}$ seem fortuitously tuned in hydrogen and helium content relative to the gas-poor terrestrial planets and the two jovian planets that experienced run-away gas accretion (Goldreich et al. 2004; Morbidelli 2013). Thus it was surprising to discover that the most numerous planets around other stars have radii $1\text{-}4 R_{\oplus}$ (Borucki et al. 2010, 2011; Batalha et al. 2013), a size domain expected to be nearly deserted (Ida & Lin 2010; Mordasini et al. 2012).

The great population of sub-Neptune size exoplanets had been revealed first by precise Doppler surveys of solar-mass stars within 50 pc that discovered an increas-

ing number of planets with smaller masses, from 1000 M_{\oplus} down to $\sim 5 M_{\oplus}$ (Howard et al. 2011; Mayor et al. 2011). Independently, the NASA *Kepler* telescope finds that 85% of its transiting planet “candidates” have radii less than $4 R_{\oplus}$ (Batalha et al. 2013). Over 80% of these small planet candidates are actually planets (Morton & Johnson 2011; Fressin et al. 2013) securing the reality of this large population (but see Santerne et al. (2012) for Jupiter-size planets). No detection bias favors the discovery of small planets over large ones, reinforcing the reality of this numerous population of $1\text{-}4 R_{\oplus}$ planets that greatly outnumbers the larger planets. Thus, an overwhelming majority of planets orbiting within 1 AU of solar-type stars are smaller than $4 R_{\oplus}$ (the size of Uranus and Neptune), both in the vicinity of the Sun and in the *Kepler* field of view located slightly above the plane of the Milky Way Galaxy.

Measuring the occurrence of planets as a function of planet radius and orbital period requires a correction of the *Kepler* data for detection biases including those due to photometric noise, orbital inclination, and the completeness of the detection pipeline of the *Kepler* planet search. Three such efforts show that the number of planets orbiting within 0.25 AU of solar type stars rises rapidly with decreasing planet radius from $15 R_{\oplus}$ to $2 R_{\oplus}$ (Howard et al. 2012; Fressin et al. 2013; Petigura et al. 2013). Further corrections for photometric SNR and software completeness shows that the occurrence of planets remains at a (high) constant level for sizes of 2 to $1 R_{\oplus}$, with $\sim 15\%$ of FGK stars having a planet of $1\text{-}3 R_{\oplus}$ within 0.25 AU (Fressin et al. 2013; Petigura et al. 2013).

This prominent population of $1\text{-}4 R_{\oplus}$ planets raises profound questions about their chemical composition, interior structure, formation processes, and their gravitational interactions with other planets (Seager et al. 2007; Fortney et al. 2007; Zeng & Seager 2008; Rogers et al. 2011; Zeng & Sasselov 2013; Lissauer et al. 2012; Fabrycky et al. 2012). The relative amounts of rock, water, and H/He gas remain poorly known, and there are likely to be different admixtures of those three ingredients both as a function of planet mass and from planet to planet at a given mass.

These $1\text{-}4 R_{\oplus}$ planets pose a great challenge for the theory of planet formation as do Venus/Earth and Uranus/Neptune, with ratios of rock to light material not close to the cosmic abundances. However new ideas are emerging about the formation of such neptune-mass planets and sub-neptunes involving variations on the theme of core-accretion theory (Chiang & Laughlin 2012; Mordasini et al. 2012). Particularly intriguing is the notion that the hundreds of exoplanet candidates identified by *Kepler* offer, as an ensemble, a measure of the mass densities of protoplanetary disks during planet formation, as revealed by the distribution of the planet-candidates themselves, leading to a theory of *in-situ* formation of sub-neptunes within 0.5 AU of the host star (Chiang & Laughlin 2012). Support for these models comes from the observed low densities of small exoplanets that agree with the gas-to-rock predictions, and from the relations of incident flux to gas content both predicted and observed (Lopez et al. 2012; Weiss et al. 2013). These models and associated predictions of *in situ* formation of mini-neptunes and “super-Earths” can be tested

¹² Aarhus University, DK-8000 Aarhus C, Denmark

¹³ High Altitude Observatory, National Center for Atmospheric Research, Boulder, CO 80307

¹⁴ NASA Exoplanet Science Institute/Caltech, Pasadena, CA 91125

¹⁵ National Optical Astronomy Observatory, Tucson, AZ 85719

¹⁶ Massachusetts Institute of Technology, Cambridge, MA, 02139

¹⁷ Northwestern University, Evanston, IL, 60208, USA

¹⁸ University of California, Santa Cruz, CA 95064

¹⁹ Yale University, New Haven, CT 06510

²⁰ University of Florida, Gainesville, FL 32611

²¹ Orbital Sciences Corp., NASA Ames Research Center, Moffett Field, CA 94035

²² California Institute of Technology, Pasadena, CA 91109

²³ Department of Physics, Broida Hall, University of California, Santa Barbara, CA 93106

²⁴ Centre for Astrophysics Research, University of Hertfordshire, College Lane, Hatfield, AL10 9AB, England

²⁵ San Diego State University, San Diego, CA 92182

²⁶ Carnegie Institution of Washington, Dept. of Terrestrial Magnetism, Washington, DC 20015

²⁷ Lawrence Hall of Science, Berkeley, CA 94720

²⁸ Villanova University, Dept. of Astronomy and Astrophysics, 800 E Lancaster Ave, Villanova, PA 19085

²⁹ University of Hawaii, Honolulu, HI

³⁰ Department of Astronomy, Box 351580, University of Washington, Seattle, WA 98195, USA

³¹ Bay Area Environmental Research Institute/ Moffett Field, CA 94035, USA

³² Vanderbilt University, Nashville, TN 37235, USA

³³ McDonald Observatory, University of Texas at Austin, Austin, TX, 78712, USA

³⁴ University of Notre Dame, Notre Dame, Indiana 46556

³⁵ NOAO, Tucson, AZ 85719 USA

³⁶ Southern Connecticut State University, New Haven, CT 06515 USA

³⁷ MSFC, Huntsville, AL 35805 USA

³⁹ Las Cumbres Observatory Global Telescope, Goleta, CA 93117, USA

⁴⁰ Max Planck Institute of Astronomy, Koenigstuhl 17, 69115 Heidelberg, Germany

⁴¹ School of Physics and Astronomy, University of Birmingham, Birmingham B15 2TT, UK

⁴² Institut d’Astrophysique de Paris, UMR7095 CNRS, Université Pierre & Marie Curie, 98bis boulevard Arago, 75014 Paris, France

⁴³ Observatoire de Haute Provence, CNRS/OAMP, 04870 Saint-Michel-l’Observatoire, France

⁴⁴ Aix Marseille Université, CNRS, LAM UMR 7326, 13388, Marseille, France

⁴⁵ Centro de Astrofísica, Universidade do Porto, Rua das Estrelas, 4150-762 Porto, Portugal

⁴⁶ NASA Headquarters, Washington DC

[†] Based in part on observations obtained at the W. M. Keck Observatory, which is operated by the University of California and the California Institute of Technology.

with accurate measurements of planet masses and radii. Measurements of planet masses for transiting planets that already have measured radii can constrain the mean molecular weight, internal chemical composition, and hence formation mechanisms for 1-4 R_{\oplus} planets (Seager et al. 2007; Zeng & Seager 2008; Zeng & Sasselov 2013; Rogers et al. 2011; Chiang & Laughlin 2012). Mass measurements have been made for only a handful of small planets. Two linchpins are GJ 436 b and GJ 1214 b (Maness et al. 2007; Gillon et al. 2007; Torres et al. 2008; Charbonneau et al. 2009) with radii of 4.21 and 2.68 R_{\oplus} , respectively, masses of 23.2 and 6.55 M_{\oplus} , respectively, and resulting bulk densities of 1.69 and 1.87 g cm^{-3} , respectively. Their densities are slightly higher than those of Uranus and Neptune (1.266 and 1.631 g cm^{-3}), but well below that of Earth at 5.5 g cm^{-3} , indicating that the two exoplanets are composed of silicates, iron/nickel, and significant amounts of material less dense than rock, presumably H, He, and water (Figueira et al. 2009; Rogers & Seager 2010a). Somewhat larger is Kepler-18 c with a radius of 5.5 R_{\oplus} and a mass of only 17.3 M_{\oplus} , implying quite low density (Cochran et al. 2011). Similarly, HAT-P26 of 6.3 R_{\oplus} has low density (Hartman et al. 2011). One wonders if these securely measured low (sub-rock) densities are representative of planets of size 2.0-4.5 R_{\oplus} in general, and hence representative of the chemical composition of such planets.

Secure masses and radii have been measured for several other 2-4 R_{\oplus} exoplanets, including the five planets around Kepler-11, GJ 3470 b, 55 Cnc e, and Kepler-68 b (Lissauer et al. 2013; Bonfils et al. 2012; Demory et al. 2013, 2011; Gilliland et al. 2013). All of these planets have densities less than 5 g cm^{-3} and some under 1 g cm^{-3} , indicating a significant amounts of light material (H/He, water) mixed with some rock/Fe. (The uncertainties for 55 Cnc e admit the possibility this 2.1 R_{\oplus} planet could be pure rock.) In contrast, the two planets with radii less 2 R_{\oplus} , namely CoRoT 7b and Kepler-10b, both have measured densities of 6-10 g cm^{-3} (Queloz et al. 2009; Batalha et al. 2011). Thus, below 2 R_{\oplus} some planets have densities consistent with solid rock and iron-nickel.

To quantify this transition to rocky planets, one may use the extant empirical relation between density and planet mass that has been discovered for the planets smaller than 5 R_{\oplus} : $\rho = 1.3M_p^{-0.60}F^{-0.09}$, where ρ is in g cm^{-3} , M_p is in M_{\oplus} , and F is the incident stellar flux on the planet in $\text{erg s}^{-1} \text{cm}^{-2}$ (Weiss et al. 2013). The Weiss et al. relation shows that planets with masses over $\sim 2 M_{\oplus}$, (equivalently with radii over 1.5 R_{\oplus}) have typical densities less than 5.5 g cm^{-3} and hence typically contain significant amounts of light material (H/He, water). *Thus, the transition from planets containing significant light material to those that are rocky occurs at planet radii near 1.5 R_{\oplus} , i.e. masses near 2 M_{\oplus} ,* based on the current handful of planets in that size domain. The transition depends slightly on incident stellar flux. This appearance of rocky planets below masses of 2 M_{\oplus} is a major result from current *Kepler* exoplanet observations (Weiss et al. 2013). However, this Weiss et al. relation, and the predicted discontinuity to rocky planets at 1.5 R_{\oplus} , is based on the measured masses and radii of only a handful of planets. It surely requires both confirmation and quantification, by measuring the masses and

radii of more small exoplanets. Models of planet formation would be greatly informed by correlations found between the rocky and volatile nature of the planets and the masses and metallicities of their host stars (Buchhave et al. 2012; Latham & Buchhave 2012; Johnson et al. 2007).

Here we report measured masses, radii, and densities (and upper limits) for 42 planet candidates contained within 22 bright *Kepler* Objects of Interest (KOIs) from Batalha et al. (2013). We carried out multiple Doppler-shift measurements of the presumed host stars using the Keck 1 telescope. From the spectroscopy, and Doppler measurements, we compute self-consistent measurements of stellar and planet radii, employing either stellar structure models or asteroseismology measurements from the *Kepler* photometry. We also search for (and report) non-transiting planets revealed by the precise radial velocities

2. VETTING AND SELECTION OF 22 TARGET KOIS

This paper contains the results of extensive precise RV measurements of KOIs made by the *Kepler* team during the nominal NASA mission from launch 2009 March to 2012 November, with a few RVs obtained the next spring. During that time the *Kepler* team carried out an extensive and iterative program to identify planet candidates. Initial identification of the KOIs from the photometry has been extensively described elsewhere, notably by Caldwell et al. (2010); Jenkins et al. (2010b,a); Van Cleve & Caldwell (2009); Argabright et al. (2008), with summaries in Borucki et al. (2010). The KOIs identified in these searches are most recently captured in Batalha et al. (2013).

We carried out a follow-up observing program ("FOP") and a vetting, certification program ("TCERT") designed to both distinguish planet candidates from false positives and to measure properties of the planets and their host stars. Detailed descriptions of the components of these programs can be found in (Gautier et al. 2010; Borucki et al. 2011; Batalha et al. 2013). In brief, KOIs were included as planet candidates based on simple (often eye-ball) diagnostics involving inspection of *Kepler* light curves, approximate position stability in and out of transit (within ~ 1 arcsec), and lack of obvious eclipsing binary signatures such as secondary eclipses, including "odd-even" occurrence of transit depths. No non-*Kepler* observations were included in this initial identification of the KOIs.

The *Kepler* team's TCERT and FOP committees identified KOIs worthy of follow-up observations designed both to weed out false positives and to better measure the planet properties through superior knowledge of host star properties, notably radii. Various types of follow-up observations of some, but not all, of the ~ 2300 KOIs had been carried out by the time of their publication (Borucki et al. 2011; Batalha et al. 2013). The 22 KOIs reported here were selected by the TCERT committee for intense RV follow-up after extensive follow-up observations, described below.

KOIs were systematically observed with a variety of ground-based observations, and they had their *Kepler* light curves and astrometric integrity scrutinized, by a variety of techniques to vet them for planet status and to measure their radii more precisely. Here we summarize the key reconnaissance efforts that were carried out on

over 1000 KOIs from which the 22 KOIs presented here were selected.

In brief, each KOI had its light curve scrutinized and position measured (Section 2.1) to alert us to angularly nearby stars (within 2 arcsec) in the photometric aperture. We carried out adaptive optics (AO) imaging and speckle interferometry (Section 2.2.2 and Section 2.2.1) to hunt for neighboring stars. Upon passing those gates, we carried out high-resolution, low SNR echelle spectroscopy to measure atmospheric stellar parameters, magnetic activity, and rotational Doppler broadening to detect binaries and assess suitability for precise RV measurements. As described below, these follow-up observations revealed no evidence of a nearby eclipsing binary for any of the 42 candidate transiting planets described here. Below is a summary of the nature of these vetting actions performed on all 22 KOIs.

2.1. Data Validation

Photometric signals that mimic planet transits are identified by the *Kepler* Transit Planet Search (TPS) in the long cadence photometry. All "threshold crossing events" (TCEs) are judged regarding plausible planet origin by the quality of the fit of the predicted light curve from the transit-planet model to the observed photometry, and by a search for astrometric displacements of the photocenter between times in and out of transit. Actual transiting planets should exhibit photometry that is well fit, within errors, by a transiting planet model and they should show insignificant astrometric displacement during transit. Such "Data Validation" (DV) techniques are described in Batalha et al. (2010, 2011); Bryson et al. (2013). These DV tests have undergone improvements and automation during the past three years Wu et al. (2010); Bryson et al. (2013). All 22 KOIs in this work passed their DV tests, conferring KOI status on them as continued planet candidates. Details on the nature of DV criteria for each KOI are given below in Section 7.

2.2. Follow-Up Reconnaissance Spectroscopy

We carried out "reconnaissance" high resolution spectroscopy, with $R \sim 50000$ and $\text{SNR} = 20 - 100$ per pixel for each of the 22 target KOIs, with two primary goals, searching for false positives and refining the stellar parameters. For all 22 KOIs, we obtained one or two such reconnaissance spectra using one of four facilities: the McDonald Observatory 2.7m, the Lick Observatory 3m, the Tillinghast 1.5m on Mt. Hopkins, and the 2.6m Nordic Optical Telescope.

Of foremost importance was to detect angularly nearby stars that, themselves, might be eclipsed or transited by a companion star or planet, the light from which would be diluted by the primary star mimicking a transiting planet around it. With a typical spectrometer slit width of 1 arcsec, stellar companions within 0.5 arcsec would send light into the slit, allowing detection. A cross correlation of the spectrum was performed, usually with a solar template, to detect stellar companions separated by more than $\sim 10 \text{ km s}^{-1}$ in radial velocity and brighter than $\sim 5\%$ of the primary in optical flux. Also, a second reconnaissance spectrum was obtained to detect radial velocity variation above a threshold of $\sim 0.5 \text{ km s}^{-1}$, indicating the presence of an eclipsing binary. None of the 22 KOIs in this paper showed any sign of any neighboring

star within the limit specified above. This absence of a secondary spectrum and of RV variations (confirmed by the precise RVs with 2 m s^{-1} precision) for all 22 KOIs rules out a large portion of parameter space for possible false positives in the form of a nearby star that itself dims periodically. As described in Section ??fpp1, a further analysis of the Keck-HIRES spectra taken later with *high SNR* further ruled out stellar companions within 0.5 arcsec down to optical flux levels of 1% of the primary star.

The reconnaissance spectra were also analyzed to measure the properties of the host star more precisely than was available in the *Kepler* Input Catalog (KIC). The spectra were analyzed by comparing each one to a library of theoretical stellar spectra, e.g., Buchhave et al. (2012). This "recon" analysis was done with a step size between individual library spectra of 250 K for T_{eff} , 0.5 dex for $\log g$, 1 km s^{-1} for $v \sin i$, and 0.5 dex in metallicity([m/H]). This process yielded approximate values of T_{eff} (within 200K), $\log g$ (within 0.10 dex), and $v \sin i$ (within 2 km s^{-1}), for the primary star of the KOI, all being valuable for deciding whether the KOI was suitable for follow-up precise RV observations. Only stars cooler than 6100K on the main sequence with $v \sin i < 5 \text{ km s}^{-1}$ are suitable for RV measurements with precision of $\sim 2 \text{ m s}^{-1}$. All relevant details about the reconnaissance spectroscopy for each KOI are given in Section 7.

2.2.1. Speckle Imaging

Speckle imaging of each of the 22 KOIs was obtained using the two-color DSSI speckle camera at the WIYN 3.5-m telescope on Kitt Peak, with technical details given in Howell et al. (2011); Horch et al. (2009). The speckle camera simultaneously obtained 3000 images of 40 msec duration in two filters: *V* (5620/400Å) and *R* (6920/400Å). These data yielded a final speckle image for each filter. Section 7 describes the results of the speckle observation for each KOI noting if any other sources appeared.

The speckle data for each star allowed detection of a companion star within the 2.76×2.76 arcsec field of view centered on the target. The speckle observations could detect, or rule out, companions between 0.05 arcsec and 1.5 arcsec from each KOI. The speckle images were all obtained with the WIYN telescope during seeing of 0.6 - 1.0 arcsec. The threshold for detection of companion stars was a delta magnitude of 3.8 mag in the R band and 4.1 mag in V band, relative to the brightness of the KOI target star. For KOI-292 the detection threshold was somewhat compromised by a stellar companion 0.36" away from the primary and 2.7mags fainter. These speckle observations showed that none of the other 22 KOIs in this work had a detected companion by speckle, thus ruling out a major domain of parameter space for possible false positives (stars with transiting companions).

2.2.2. AO Imaging

Near-infrared adaptive optics imaging was obtained for all 22 KOIs to detect stellar companions that might be the source of the periodic dimming (a false positive). Seeing-limited imaging, obtained with various telescopes at both optical and IR wavelengths, informed us of companions located more than 2 arcsec from the primary

KOI star. Seeing-limited J-band Images from UKIRT were particularly useful (Lawrence et al. 2007). In addition we examined optical seeing-limited images from the Keck-HIRES guide camera for each of the 22 KOIs, and we provide those images herein, below. The strength of AO imaging is detection of companions located between 0.2 - 2.0 arcsec of the KOI primary star. The goal was to detect nearby stars that might potentially have an eclipsing companion or a transiting planet that might mimic a transiting planet around the primary star, i.e. a false positive.

Three AO instruments were used in the near IR on three different telescopes, namely the MMT telescope on Mt. Hopkins (ARIES), the 5m telescope on Mt. Palomar (PHARO), and the 3m telescope at Lick Observatory (IRCAL), each described briefly below (Hayward et al. 2001; Troy & Chanan 2003; Adams et al. 2012). The Lick IRCAL AO system, built by Claire Max and James R. Graham, is described in detail at

astro.berkeley.edu/~jrg/ircal/spie/ircal.html

The MMT ARIES camera achieves near diffraction-limited imaging, with typical PSF FWHM of $0''.25$ in the J-band and $0''.14''$ in the Ks band, yielding Strehl ratios of 0.3 in Ks and 0.05 in J band (Adams et al. 2012). While guiding on the primary star, a set of 16 images, on a four-point dither pattern was acquired for each KOI. Full details and a description of calibration and reduction of the images is described by Adams et al. (2012)

Some of the KOIs were observed with the Palomar 5m PHARO camera observed KOIs in both the Ks and J infrared bands using a 5-point dither pattern with integration times between 1.4 and 70 seconds, depending on the target brightness. The AO system used the primary star itself, not a laser, to guide and correct the images, achieving a best resolution of $0''.05$ at J and $0''.09$ in the Ks band, with Strehl ratios of 0.10-0.15 in J and 0.35-0.5 in Ks. Typical detection thresholds were 7 mag at a separation of 0.5 arcsec and 9.3 mag at 1.0 arcsec (3-sigma upper limits in flux).

The remaining KOIs were observed with the Lick Observatory 3-m telescope and high resolution camera, "IRCAL". Observations were made in Natural Guide Star (NGS) mode, allowing the AO system to guide on the target star. This mode of observing allows stars as faint as KepMag = 13.5 to be observed. Typical Strehl ratios of ??? were achieved under average seeing of ????. Exclusion limits down to a delta magnitude of ?? are typically achieved. Background sky emission in the J-band is typically 16.0 magnitudes per square arcsecond. The K-band background sky emission is 10.3 magnitudes per square arcsecond, making K-band observing difficult. Typically only J-band images were taken. [David Ciardi can potentially fill in the blanks here].

Details of companions found within $6''$ of each of the 22 KOIs are given in Section 7 and also in (Adams et al. 2012). Those KOIs exhibiting a companion star were KOIs: 108, 122, 123, 148, 153, 261, 283, and 292. The following KOIs have no stellar companions within 6 arcsec: 41, 69, 82, 104, 116, 244, 245, 246. KOIs 299, 305, 321, 1442, and 1925 were not listed in Adams et al. (2012).

For each KOI, we describe in Section 7 the specific AO observation obtained. Any KOI with a neighboring star located within 2 arcsec that had more than 1% the flux

of the primary star at optical wavelengths was rejected as a suitable candidate for precise RV measurements due to the contamination of light from that nearby star and due to the possible false positive. The 21 of the 22 KOIs in this paper were devoid of such bright, troublesome companions. KOI-292 was dropped from our target list when the nearby companion was identified.

2.3. Selecting the 22 KOIs

The selection criteria adopted by the *Kepler* Project TCERT committee for precise RV follow-up observations changed during the first three years of the mission. Initial criteria emphasized the desire to verify the planet-nature of the KOIs. This effort favored large planets with sizes above $4 R_{\oplus}$ and short-period orbits that might yield a detectable RV variation in the host star to check the existence of *Kepler* transiting planets. RV detections of large planets around Kepler 4, 5, 6, 7, and 8 followed from this prioritization. After the successes of the first six months of the *Kepler* mission, the criteria shifted toward verifying and measuring the masses of the smaller planets, $2-5 R_{\oplus}$, and multiple planets, if they were likely to be detected with RVs. Resulting RV detections included Kepler 10, 11, 18, 20, 22, 25, and 68 yielding constraints on the masses of planets.

During the second and third years of the nominal *Kepler* mission, i.e. 2010 and 2011, the TCERT prioritization shifted toward a desire to verify and measure masses of KOIs having even smaller radii, below $3 R_{\oplus}$ and down to $1.0 R_{\oplus}$. Obviously such small planets are expected to have low masses, inducing small RV amplitudes in their host star. We carried out careful, optimized selection of these suitable KOIs for RV work.

Among the selection criteria was a brightness limit, $\text{Kepmag} < 13.5$, to permit Poisson-limited signal-to-noise ratios near 100 per pixel within a 45 minute exposure with the Keck-HIRES spectrometer. Such exposures gave a photon-limited Doppler precision of 2 m s^{-1} . Another selection criteria included $T_{\text{eff}} < 6100\text{K}$ (based on reconnaissance spectra) to promote numerous, narrow spectral lines. Another criterion was rotational $v \sin i < 5 \text{ km s}^{-1}$ (also based on reconnaissance spectra) to limit rotational Doppler broadening of the lines that otherwise would degrade Doppler precision. The *Kepler* TCERT committee further selected KOIs for which the planet radius, coupled with a rough estimate of planet density for that radius, yielded a predicted planet mass that would induce an RV amplitude greater than 1.0 m s^{-1} , making an RV detection plausible in the face of pervasive astrophysical "jitter" of 1 m s^{-1} for G and K dwarfs (Isaacson & Fischer 2010). The density assumptions were simplistically based on the planets in our solar system along with the few known small exoplanets, notably GJ436b, GJ1214b, and Kepler-10b. We simply assumed a rocky constitution and density of $\sim 5.5 \text{ g cm}^{-3}$ for planets smaller than $2 R_{\oplus}$. We assumed densities of 2 g cm^{-3} for planets of $2-5 R_{\oplus}$, and we assumed densities of 1 g cm^{-3} for planets larger than $5 R_{\oplus}$. These density assumptions allowed the *Kepler* TCERT to choose KOIs whose planets might meet the detection criteria noted above, including a prospective RV amplitude above 1 m s^{-1} . The selection process was imperfect and biased as the assumed stellar parameters and planet densities were only approximately known and the target KOIs

were tuned to domains of planet radius and detectability. This paper contains a report on the 22 KOIs selected by the process described above. These 22 KOIs were selected for precise RV follow-up observations during the nominal *Kepler* mission and have not been published to date, except for Kepler-68 (KOI-246) for which we provide an update to its interesting long-period, non-transiting planet. This sample of 22 KOIs contains neither a random selection of KOIs nor a defined distribution of any parameters. They were selected during three years of ever-evolving criteria, as described above. The planet masses were unknown at the time of target selection, except for estimates based on measured planet radii and guesses of density. *However, for each KOI the measured planet mass provides an unbiased sampling of planet mass for a particular planet radius.* We could not have selected KOIs biased toward high or low planet masses for a given planet radius, as we had no such mass indicator. Thus, the RVs for each KOI provide one unbiased sampling of the distribution of planet masses for its specific planet radius.

In general, the distribution of planet masses for a given planet radius is likely to be a function of orbital period and the type of star. The distribution of planet masses surely depends on planet radius, stellar mass, orbital semi-major axis and eccentricity, and on the chemical and thermodynamic properties of the protoplanetary region where they form. Thus, the measured planet masses and radii here inform only one plane of a multi-dimensional space that characterizes planet properties. Interestingly, the typical planet density may decrease dramatically with increasing planet radius due to an increasing admixture of light building material (H, He, water) (Weiss et al. 2013). Average planet masses may *decrease* with increasing planet radii (even discontinuously) within some domains of planet size, especially at the transition from rocky to volatile-rich planets near $2 R_{\oplus}$. For example, planets of $1.8 R_{\oplus}$ may typically be less massive than those of $1.5 R_{\oplus}$ if typical densities decrease with increasing radius, a possibility we hope to test with this present work.

3. STELLAR CHARACTERIZATION

For each of the 22 KOIs, we obtained an optical "template" spectrum using the Keck telescope and its HIRES echelle spectrometer with no iodine gas in the light path. Each spectrum spanned wavelengths from 3600-8000 Å, with a spectral resolution of $R=60000$ and typical SNR per pixel of ~ 200 . These template spectra were analyzed with the standard LTE spectrum synthesis code, SME (Valenti & Piskunov 1996; Valenti & Fischer 2005; Fischer & Valenti 2005) to yield values of T_{eff} , $\log g$, and [Fe/H] accurate to 50K, 0.1 dex, and 0.05 dex, respectively, with slight differences in precision due to SNR and spectral type. Values of $\log g$ are somewhat more uncertain for $T_{\text{eff}} > 6100$ K where the magnesium b triplet lines become increasingly less sensitive to stellar surface gravity.

For 11 KOIs an asteroseismic signal was detected in the *Kepler* photometry, namely for KOIs 41, 69, 108, 122, 123, 244, 245, 246, 321, 1612 and 1925. For those 11 KOIs the output stellar parameters from the SME analysis, namely T_{eff} , $\log g$, and [Fe/H], were fed into the asteroseismology analysis as priors, which, along with

stellar evolution models, yielded a more precise measure of stellar radius and mass, and hence of surface gravity. This more accurate surface gravity was frozen and fed back into an SME analysis of the spectrum, allowing a redetermination of T_{eff} and [Fe/H] without the usual covariances with $\log g$. The resulting values of T_{eff} and [Fe/H] were then fed back to an asteroseismology analysis as before, achieving an iterative convergence quickly (Huber et al. 2013; Gilliland et al. 2013). The resulting uncertainties in stellar radius are between 2 and 4% (Huber et al. 2013). Stellar parameters for these 11 KOIs with asteroseismology are reported in Table 1.

For the remaining 11 KOIs that offered no asteroseismology signal, we determined the stellar mass and radius from the SME spectrum analysis combined with the Yonsei-Yale stellar structure models (Yi et al. 2001; Demarque et al. 2004). The SME output values of T_{eff} , $\log g$, and [Fe/H] map to a unique stellar mass and radius for stars on the main sequence and subgiant branch where all 22 KOIs reside. The best-fit Yonsei-Yale stellar structure model was identified by incrementally varying the mass, age, and metallicity of the assumed star and noting the difference between the associated values of T_{eff} , $\log g$, and [Fe/H] and those found from the SME analysis, minimizing the chi-square statistic, and producing a posterior distribution of stellar radius, mass, [Fe/H], luminosity, age, and mean stellar density. See Borucki et al. (2013) for details. For the mild subgiants, the output SME stellar parameters may correspond to regions of the HR diagram where some convergence of the evolutionary tracks occurs, leaving greater uncertainties in the resulting stellar mass and radius, e.g., (Batalha et al. 2011). Any such uncertainties are duly noted and included in the subsequent analysis of the properties of the planets.

The resulting determinations of stellar masses and radii for the 22 KOIs (with or without asteroseismology) are employed as priors in a self-consistent Markov-Chain Monte Carlo (MCMC) analysis of the *Kepler* transit light curves and Keck RVs. Final stellar parameters are determined by self-consistent fits of the *Kepler* light curve and RVs to a model of a planet transiting its host star (see below). The MCMC analysis employs the input stellar parameters from above as priors. The *Kepler* transit light curve shape and orbital period (notably transit duration) implicitly further constrain the stellar density and hence further constrain stellar radius and mass. By solving for all stellar (and planet) parameters simultaneously, and by constraining the fit with priors on T_{eff} , $\log g$, and metallicity, along with Yonsei-Yale stellar isochrones, we obtain final values of stellar radius and mass, along with planet parameters. Excellent discussions of the iterative convergence of spectroscopic and asteroseismology results, along with self-consistent light curve analysis is provided by Torres et al. (2012); Gilliland et al. (2013); Borucki et al. (2013). The final values of all stellar parameters are listed in Table 1. In the following sections, these stellar parameters are used, along with the *Kepler* photometry, RVs, and stellar structure models, to derive the properties of the 42 planet candidates, listed in Table 2 and the false positive probabilities(FPP) list in Table 3 and discussed in Section 6.

4. KECK-HIRES PRECISE VELOCITY MEASUREMENTS

We observed the 22 KOIs with the HIRES spectrometer at the Keck Observatory from 2009 July to 2013 May, obtaining 20-50 RV measurements for each of them during that time span. The setup used for the RV observations was the same as used by the California Planet Search (CPS) (Marcy & Butler 1992a; Marcy et al. 2008) in which RVs were measured for over 2000 nearby FGKM stars, $V < 10$ mag, demonstrating a typical RV precision of 1.5 m s^{-1} (RMS) on all time scales, from minutes to years (Howard et al. 2010). For those bright stars, the photon-limited RV precision and the typical RV fluctuations (jitter) from complex gas flows in the photosphere were matched at $\sim 1.5 \text{ m s}^{-1}$. For the Doppler measurements of the KOIs our setup of the Keck-HIRES spectrometer was nearly the same, including a slit width of 0.87 arcsec, yielding a resolving power of $R \approx 60,000$ between wavelengths 3600 and 8000 Å. The typical exposure times were 10 and 45 minutes (for Kepmag = 10-13), resulting in a signal to noise (SNR) ratio between 70 and 200 per pixel, depending on the brightness of the target. As a benchmark, at Kepmag=13.0, the typical exposure was 45 minutes, giving SNR=75 per pixel, and each pixel spanned $\sim 1.3 \text{ km s}^{-1}$. With such exposures, photon statistics of the observed spectrum, along with the comparable SNR of the comparison template spectrum, limited the RV precision to $\sim 2 \text{ m s}^{-1}$, slightly greater than typical jitter and systematic errors of $\sim 1 \text{ m s}^{-1}$ from both. Indeed, KOIs yielding non-detections typically have an RMS of the RVs of $\sim 3 \text{ m s}^{-1}$, as shown in Tables 4 - 25. We note that at SNR=70 uncertainties in wavelength scale are estimated to be less than 0.5 m s^{-1} due to the wavelength information contained in thousands of iodine lines, making wavelength errors a minor source of error compared to the astrophysical jitter of 1.5 m s^{-1} .

The raw reduction of the CCD images followed the standard pipeline of the CPS group, but with the addition of sky subtraction made possible by the use of a 14 arcsec long slit. The spectra were obtained with the iodine absorption cell in front of the entrance slit of the spectrometer, superimposing iodine lines directly on the stellar absorption line spectrum, providing both the observatory-frame wavelength scale and the instrumental profile of the HIRES spectrometer at each wavelength (Marcy & Butler 1992b). The Doppler analysis was the same as that used by the CPS group (Johnson et al. 2010). "Template" spectra obtained without iodine gas in the beam were used in the forward modeling of spectra taken through iodine to solve simultaneously for the wavelength scale, the instrumental profile, and the RV in each of 718 segments of length 80 pixels corresponding to $\sim 2.0 \text{ \AA}$ depending on position along each spectral order. The internal uncertainty in the final RV measurement for each exposure is the weighted uncertainty in the mean RV of those 718 segments, the weights of which are determined dynamically by the RV scatter of each segment relative to the mean RV of the other segments. The resulting weights reflect the actual RV performance quality of each spectrum segment. The template spectra are also used in spectroscopic analysis to determine stellar parameters, as described above.

The typical long exposures of 10-45 minutes and modest SNR of the stellar spectra imply that night sky emission lines and scattered moonlight may significantly con-

taminate the spectra. To measure and remove the contaminating light we use the C2 decker on HIRES which projects to $0''.87 \times 14''.0$ on the sky. The C2 decker collects both the stellar light and night-sky light simultaneously. The star was guided at the center of the slit while the sky light passes through the entire 14 arcsec length of the slit. The sky contamination is thus simultaneously recorded with the stellar spectrum at each wavelength in the regions above and below each spectral order, beyond the wings of the PSF of the star image projected onto the CCD detector. The "sky pixels" located above and below each spectral order provide a direct measure of the spectrum of the sky and we subtract that sky light on a column by column basis (wavelength by wavelength). When the seeing is greater than $1''.5$ (which occurs less than 10% of the time at Mauna Kea), we do not use the C2 decker but instead use a slit of dimensions $0''.87 \times 3''.5$ (B5 decker) and we observe only bright stars, Kepmag < 11 , with exposure times of ~ 10 min to avoid sky contamination.

Observations of KOIs acquired in 2009 did not employ the C2 decker leaving no ability to perform sky subtraction, resulting in additional RV errors from scattered moonlight. We quantified these RV errors by studying the contamination seen in long-slit spectra and by comparing the scatter in the RVs during 2009 (no sky subtraction) to the RVs obtained in later years (with sky subtraction), permitting us to compute the additional RV errors incurred in 2009. In typical gibbous moon conditions with light clouds, the moon light contributed 1-2% of the light of a Kepmag=13 star (depending on wavelength due to Rayleigh scattering) within a projected ~ 4 arcsec extraction width of each spectral order. Under such gibbous conditions, the moonlit sky at Mauna Kea is apparently 19th mag per square arcsec in V band. Increasing amounts of cirrus clouds will scatter more moon light into the slit but will transmit less star light, thereby increasing the relative amount of contamination of the stellar spectrum. We found that RV errors of up to 10 m s^{-1} occurred during 2009, depending on the amount of contamination and the relative radial velocity of the stellar spectrum and the scattered solar spectrum from the moon. Employing sky subtraction with the C2 decker yielded RV precision as if no sky contamination occurred, as the observed RV scatter does not depend on the phase or presence of the moon. For stars brighter than Kepmag=11 the sky subtraction made no difference in RV precision as moon light was apparently negligible.

The measured RVs for each of the 22 KOIs are listed in Tables 4 - 25, and plots of the RVs for each of the 42 planet candidates, phased to the final orbit (see next section), are shown in Figures 23d - ??d. In the Tables 4 - 25 holding the RVs, the first column contains the julian date when the star light arrived at the solar system barycenter (BJD) based on the measured photon-weighted mid-time of the exposure. The second column contains the relative RV (with no defined RV zero point) in the frame of the barycenter of the solar system. Only the changes with time in the RVs are physically meaningful for a given star, not the individual RV values. The absolute radial velocities can easily be determined relative to the solar system barycenter, but only with an accuracy of $\sim 50 \text{ m s}^{-1}$ (Chubak et al. 2012). The third column contains the RV uncertainty, which includes both the internal un-

certainty (from the uncertainty in the mean Doppler shift of 718 spectral segments) and an approximate jitter of 2 m s^{-1} (from photospheric and instrumental sources) based on hundreds of stars of similar FGK spectral type (Isaacson & Fischer 2010). The actual jitter may have values between $1\text{-}3 \text{ m s}^{-1}$ for individual stars, but the actual photospheric fluid flows for any particular star and the detailed systematic RV errors are both difficult to estimate with any accuracy better than 1 m s^{-1} . The jitter is added in quadrature to the internal uncertainty for each RV measurement. The actual uncertainties are surely non-Gaussian from both the photospheric hydrodynamics and from systematic errors in the Doppler analysis, and they are likely to be temporally coherent with separate power spectra. Such error distributions are difficult to characterize precisely.

5. PLANET CHARACTERIZATION

We determine the physical and orbital properties of all 42 planet candidates around the 22 KOIs by simultaneously fitting *Kepler* photometry and Keck RVs with an analytical model of a transiting planet (Mandel & Agol 2002). In these models, we adopted the mass, radius, and the mean density of the host star as determined by either the SME analysis of the high resolution spectrum from the Keck Observatory or from an accompanying asteroseismology analysis, both methods described above in §3. The models assume Keplerian orbits with no gravitational interactions between the planets of the multiple-planet systems. This non-interaction assumption is adequate to yield parameters as accurate as the limited time series permits, as any precession or secular resonances will create detectable effects only after a decade at least. The parameters in the model include the stellar density (frozen from the SME or asteroseismology analysis), a mean photometric flux, an RV zero-point, the time of one transit (T_0), orbital period (P), impact parameter (b), the scaled planet radius (R_p/R_*), and RV amplitude (K).

We use the fourth-order non-linear parameterization of limb-darkening also described by Mandel & Agol (2002) with coefficients ($c_1 = 1.086, c_2 = -1.366, c_3 = 1.823, c_4 = -0.672$) calculated by Claret & Bloemen (2011) for the *Kepler* bandpass. We simultaneously fit all measurements with a model using a Markov-Chain-Monte-Carlo (MCMC) routine that fixes the values of the periods of the transiting planets, along with their transit times, for each KOI. The quoted values of the planet parameters in Table 2 are the values at which the posterior distribution is a maximum, often termed the "mode" of the distribution. For several planets, a non-zero eccentricity is clearly needed to produce an acceptable fit in which cases we also include as parameters the eccentricity and longitude of periape as, $e \cos(\omega)$ and $e \sin(\omega)$. When the eccentricity value is allowed to float for KOI-104, we find a superior fit over the circular model. (See appendix for results from allowing eccentricity to float.)

In all models, we allowed the value of the RV amplitude to be negative as well as positive, corresponding to both negative and positive values of planet mass. Obviously negative mass is not physically allowed. But fluctuations in the RV measurements due to errors may result in RVs that are anti-correlated with the ephemeris of the planet as dictated by the photometric light curve. Fluctuations

can spuriously cause the RVs to be slightly high when they were expected to be low, and vice versa. In such cases, the derived negative mass, and the posterior distribution of masses, is a statistically useful measure of the possible masses of the planet, especially useful when included with the ensemble of masses of other planets and their posterior mass distributions. By allowing planet mass to be negative, we account for the natural fluctuations in planet mass from RV errors. For the planet candidates that yielded less than 2-sigma detections of the RV signal (K is less than 2-sigma from zero) we also compute the positive definite mass for that planet by adopting the median of posterior distribution of masses that are greater than zero. This median of the positive values serves as a useful metric of an "upper limit" to the planet mass. It is unlikely to be more massive than twice this value, but the mass could be as low as zero in principle. We quote both values of planet mass for these non-detections, namely the one that can be negative, useful for planet-ensemble uses, and the one that is positive definite, useful for considering the mass, density, and possible chemical compositions of the individual planet.

In summary, we fit the photometry and RVs with a Mandel & Agol (2002) model by adopting the star's mass and radius based on spectroscopy (SME) and if available on asteroseismology. Model parameters are determined by chi-squared minimization, and we compute posterior distributions using an MCMC parameter search. We derive planet radius, mass, orbital period, ephemeris, and the mean stellar density in the final solution. The final stellar parameters for each star are in Table 1. The final planetary parameters are listed in Table 2, including stellar density from the model. The associated 1-sigma uncertainty for each parameter is computed by integrating the posterior distribution to 34% of its area on either side of the parameter at the peak, and is listed in Table 2.

6. FALSE POSITIVE ASSESSMENTS

As has been well documented (Torres et al. 2011), a series of periodic photometric dimmings consistent with a transiting planet may actually be the result of various astrophysical phenomena that involve no planet at all. Such "false positive" scenarios involve the light from some angularly nearby star located within the (~ 10 arcsec diameter) *Kepler* software aperture that dims with a duration and periodicity consistent with an orbiting object passing in front of the target star. The light from that nearby star may be located within the software aperture of the target star or located just outside that aperture so that the wings of its PSF encroach into the aperture, polluting the brightness measurements. The amount of pollution may vary with quarterly roll of the spacecraft, as the relative positions of stars (and their differential aberration) and aperture shift slightly. The angularly nearby star may be physically unrelated to the target star (in the background or foreground) or it may be gravitationally bound, and the cause of its dimming could be a transiting planet or star.

By considering all astrophysical false-positive scenarios in the direction of the *Kepler* field of view, the probability that a planet candidate is a false positive is calculated to be only $\sim 5\text{-}10\%$ (Morton & Johnson 2011; Fressin et al. 2013) for sub-Jupiter-size planets, representative

of most of the candidates considered in this paper. For Jupiter-size planet candidates the false positive rate is higher, $\sim 35\%$ (Santerne et al. 2012; Fressin et al. 2013) because both brown dwarfs and M dwarfs are roughly the size of Jupiter, allowing them to masquerade as giant planets. The detailed assessment of the false-positive probability (FPP) for any individual planet candidate requires careful analysis. This "planet-validation" process can be aided by the corroborating detection of the planet with some other technique such as with RVs or transit-timing measurements. Validation may also be accomplished by estimating the probability that the planet is real (from measured occurrence rates) and comparing it to the sum of the probabilities of all false-positive scenarios that are consistent with the observations.

6.1. Computing Formal False Positive Probabilities

For each planet candidate in the sample presented in this paper, we calculate the relative probabilities for the signal to be caused by a real transiting planet compared to known false positive scenarios. We employ the procedure described in detail in Morton (2012). This analysis combines a priori astrophysical information about the population of stars in the direction of the target star, including the occurrence and properties of the binary stars and planets. The analysis characterizes each the phase-folded dimming profiles with three parameters, its duration, depth, and "ingress and egress" durations, using the geometrical approximation of a trapezoid. The distribution of properties of the stars and their companions (stellar or planetary) toward the target star within the Milky Way Galaxy inform the probabilities of the false-positive scenarios and their corresponding light curves reduced to a trapezoidal characterization (depth, duration, shape).

All formal calculations here of the false-positive probabilities for angularly nearby stars (that are eclipsed or transited) assume an exclusion radius of 2 arcsec beyond the target star for their location. Any neighboring stars that both dim periodically and are located farther than 2 arcsec from the *Kepler* target star would cause an astrometric shift in photometric centroid position between times "in-transit" and "out-of-transit" as it alternately dims and brightens. The *Kepler* data validation (DV) process routinely checks for such displacements, ruling them false positives. The 2 arcsec exclusion limit adopted here for our formal calculations represents a conservative upper limit to the actual exclusion radius (discussed below). Thus our formal false positive probabilities for background objects are at least 4x larger than would be deduced by adopting the astrometric constraint from the DV report.

We consider all false-positive scenarios that yield a predicted light curve consistent with the observed light curve of the *Kepler* target star. All scenarios contribute to the cumulative probability that one of them might have produced the observed dimming for that KOI (Morton 2012). Additional constraints from follow-up observations, such as from adaptive optics imaging and the spectroscopic search for secondary lines, are not applied at this stage (but see the next subsection). Light curves in the infrared may also be used to inform false positive probabilities (Désert et al. 2012; Cochran et al. 2011; Ballard et al. 2013), but we did not use them here, deferring

such analysis for later papers (Sarah Ballard, personal communication). These additional constraints that often rule out some false-positive scenarios serve to reduce the false positive probability below that reported formally here.

Table 3 presents the results of our formal false-positive calculations (assuming the 2-arcsec exclusion radius). The first column gives the name of the planet candidates (KOI). The second column gives the probability that the target might itself be an eclipsing binary, all less than 0.001 because it is so unlikely that a companion star would eclipse the primary star yielding the short transit duration and small transit depth accomplished by a planet. Columns three, four, and five give the probabilities that the observed light curve is produced by a gravitationally bound (Hierarchical) eclipsing binary (HEB), a background eclipsing binary (BGEB), and a background star orbited by a planet (BGPL), respectively. Column six gives the estimated prior probability for the candidate planet within a 30% range in period and size. Column 7 gives the sum of the false-positive probabilities (in columns 2-5), constituting the final false-positive probability (FPP). More precisely, the FPP is the sum of probabilities in columns 2-5 divided by the sum of those columns plus the probability that it's a planet, which is $1-FPP \approx 1$.

The formal false-positive probabilities (FPPs) are less than 1% for all transiting planet candidates here, except for KOI-82.04, KOI-82.05, KOI-104.01, KOI-108.02, and KOI-1612.01, which have FPPs of 0.025, 0.043, 0.11, 0.020, and 0.39, respectively, as shown in column 7 of Table 3. *We thus find all KOIs in this paper to be formally "validated" as highly likely real planets with a criterion of 1% false-positive probability, except for the five KOIs named above.* For KOI 244.01, the formal FPP is 1.02%, close enough to 1% to be validated. Its FPP falls well below 1% when including its astrometric and follow-up observations).

6.2. Gravitationally Bound Stars with Transiting Planets

In our calculation of the FPP we do not deem as false positives scenarios involving a gravitationally bound companion star transited by a planet. In such systems a real planet does exist, albeit orbiting an unresolved bound companion star. We have considered carefully whether to deem such planets as "real" or "false positives". We find no easy answer. One useful thought experiment involves a bound companion star that is the nearly the same brightness as the primary star. It makes no sense to deem a planet a "false positive" simply because it orbits an infinitessimally fainter companion star. Indeed, that planet-host star may be the "secondary star" only in some bandpasses, thus rendering the planet "real" depending on which bandpass one considers, which is clearly absurd.

Continuing the thought experiment to companion stars that are progressively fainter than the primary leads to no "break point" at which the planet around that companion should be suddenly deemed a "false positive". Therefore, we choose here to deem all planet-candidates orbiting any (unknown) bound star in the system to be a "planet". However, if a planet does orbit a cooler (lower mass) secondary star it must be larger than was inferred

from a model of the planet orbiting the hotter primary star, to yield a final transit depth as observed. Planet occurrence decreases toward larger sizes (Howard et al. 2012), and the contribution of light from any secondary star is diluted by that of the primary star. Therefore, the probability that the transit light curve is caused by a larger planet transiting a fainter secondary star can be estimated, as follows.

Roughly 40% of FGK stars have a companion star beyond 5 AU (remaining undetected) and among those binaries, there is roughly 50% probability that the transiting planet orbits the secondary star. Thus the probability that a KOI consists of a transiting planet orbiting a secondary star is $0.4 \times 0.5 = 0.2$. But as mentioned, the required larger planet (with lower occurrence) and the dilution from the primary star (less detectable) make it less likely that the observed dimming is actually from the secondary star. *Thus the probability that a given planet candidate is actually orbiting a secondary star is well under 20%*. In such cases the planet is larger than given here in Table 2.

6.3. False Positive Probabilities: Precise Centroid Astrometry

The five KOIs with a "formal" FPP above 1% merit more detailed attention to determine if astrometry would reduce the FPP below the formal value. Those five KOIs are 82.04, 82.05, 104.01, 108.02, and 1612.01, with FPPs of 0.025, 0.043, 0.11, 0.020, and 0.39, respectively (see Table 3). The blind 2 arcsec exclusion limit yields a poor, and typically too large, estimate of the probability that a nearby star actually is the cause of the periodic dimming, mimicking a planet. Detailed Data Validation (DV) reports from the *Kepler* Project typically report exclusion limits smaller than a 1 arcsec radius (1/4 the angular area of a 2 arcsec radius circle), making our formal false positive probabilities for background objects typically too large.

For KOIs 82.04, 82.05, 104.01, 108.02, and 1612.01, the DV reports give measured exclusion radii of, 0.89", 0.42", 0.035", 0.04", 2.1", respectively. The first four exclusion radii are considerably less than the 2 arcsec assumed in our formal FPP analysis. We consider those four cases in order.

For KOI-82.04 the exclusion radius from the DV report of 0.89 has the effect of reducing the nominal FPP for background eclipsing binaries and for background stars with transiting planets by a factor that is the ratios of the areas of exclusion circles, from 2.0 to 0.89 arcsec, a factor of 5. This reduces the values of P_{BGEB} (in Table 3) from 2.41e-02 to 0.48e-02. As this was the dominant term in the FPP, the resulting more accurate FPP is 0.6e-2, under 1%. This planet is thus validated (and more so considering effects considered below).

Similarly for KOI-82.05, the nominal FPP of 4.3e-2 is dominated by the prospect of a BGEB with probability of 3.55e-02 assuming a 2 arcsec exclusion radius. With the measured exclusion radius of 0.42" from the DV report, that FPP from an BGEB drops to 0.16e-2, and the FPP of a background star with a transiting planet ("BGPL") in Table 3 drops by the same factor. The resulting more accurate total FPP for KOI-82.05 becomes 0.002, under 1%, thus validating it as a likely planet.

The case for KOI-82.05 is worthy of further comments.

Its light curve is shallow, with resulting photometric noise that allows a wide range of false-positive scenarios, including background eclipsing binaries as indicated in Table 3. That light curve for KOI-82.05 implies a small planet radius of $0.47 R_{\oplus}$ for which we have only poor knowledge of the true occurrence rate that serves as the planet-reality prior. We have likely underestimated the occurrence of such planets due to their difficulty of detection by *Kepler* so far. Work by Petigura et al. (2013) and Fressin et al. (2013) show that the occurrence of such small planets is as high as for planet of $1\text{-}3 R_{\oplus}$, thus raising the planet prior to high levels of 0.1-0.2. This enhanced planet-prior effect reduces the final FPP for both KOI-82.04 and KOI-82.05 to further under 1%.

Furthermore, the formal FPPs for KOI-82.04 and 82.05 should both be reduced by factors of roughly 10 due to their occurrence in a system of five planet candidates. It is easy to show that the probability of a background eclipsing binary that happens to be positioned, by chance, within a 2 arcsec radius of a star that already has 4 transiting planets is extremely low, less than 10^{-4} (Lissauer et al. 2012, 2013). The 2 arcsec-radius cones toward the ~ 10 target stars that harbor four transiting planets occupy such a tiny total solid angle that virtually no background eclipsing binaries are expected to exist behind any of them within the *Kepler* field. Thus, the multi-planet nature of KOI-84 provides a strong argument that both KOI-84.04 and KOI-84.05 are real planets rather than background eclipsing binaries, the dominant FP channel (Table 3). These two planets are thus elevated to false positive probabilities well under 1%, i.e. formally validated.

For KOI-108.02, the dominant false positive scenario is an eclipsing binary gravitationally bound to the *Kepler* target star. We can rule out such eclipsing binaries within 5 AU, from both the absence of a trend in the RVs during three years above $\sim 5 \text{ m s}^{-1}$ (Figure 27c) and from the absence of absorption lines from a secondary star above the 0.3% relative flux level (Figure 5). Any bound eclipsing binaries masquerading as transiting planets around KOI-108 must be farther than 5 AU, a constraint that diminishes the FPP below the nominal 2.0% level by only $\sim 10\%$ from the distribution of binary orbit separations. Interestingly, KOI-108 is a candidate multi-planet system. As argued for KOI-82 above, *Kepler* target stars harboring one transiting planet subtend a very small solid angle of the entire *Kepler* field of view, making it statistically unlikely that a background eclipsing binary is the culprit that explains the transit signal. However, the dominant channel of false positives for KOI-108.02 is a gravitationally bound eclipsing binary for which the argument against a background eclipsing binary has little weight. Thus KOI-82.02 has FPP of $\sim 1.8\%$, making it unlikely to be a false positive, but it does not benefit from the multi-transiting-planet boost.

This revised, total FPP for KOI-108.02 of 1.8% is strictly not high enough to merit formal "validation" as a planet. But this KOI has been subjected to a great battery of other follow-up observations (see below) including adaptive optics imaging, speckle interferometry, spectroscopic searches, and line bisector analysis, none of which revealed any evidence for an EB, bound to the target star or otherwise. Therefore, the 1.8% FPP must be lowered considerably further due to the parameter space

excluded by these follow-up observations. We are not prepared to engage in a full analysis of the false-positive domains excluded by all these follow-up observations. But we feel that the AO and speckle observations for this star, at a distance of 200-300 pc, rule out roughly 50% of the domain of bound eclipsing binaries, thus dropping the 1.8% total FPP to close to 1%, and likely below. We consider the FPP to be so near 1% that it merits formal validation as a likely planet.

For KOI-104.01, the dominant FP scenario is a hierarchical eclipsing binary as seen in Table 3, with a probability of 0.10. The exclusion radius of 0.035 arcsec in the *Kepler* DV report does not lower this probability, thus leaving KOI-104 formally not validated. We discuss the follow-up observations of KOI-104 in Section 6.4 that lower the false-positive probability.

KOI-1612.01 exhibits a V-shaped transit light curve, yielding a nominal FPP of 39.3% (3) stemming primarily from a background eclipsing binary scenario. With its exclusion radius of 2.1 arcsec from the *Kepler* DV report, this planet candidate must remain a candidate, as the background eclipsing binary scenario remains viable with a probability ov 39%.

Finally, we must also consider that some KOIs have exclusion radii larger than 2 arcsec, namely for 69.01 (4.7 arcsec), 1612.01 (2.1 arcsec), and 1925.01 (2.3 arcsec), making the nominal FPPs in 3 overestimated. For KOI-69.01, the nominal FPP of 1.5e-6 is so low that the large exclusion radius of 4.7 arcsec leaves the revised total FPP still well below 1%. For KOI-1612.01, the planet candidate simply gains a slightly higher FPP over the 39% value, reinforcing the uncertain nature of this KOI. For KOI-1925.01, the FPP analysis has not yet been done.

6.4. Improved False Positive Probabilities from Follow-up Observations

To tighten the estimates of the false-positive probabilities for the 42 transiting planet candidates in this paper, we performed a wide variety of follow-up observations, described in Section 2 and its subsections. The follow-up observations include high resolution spectroscopy, adaptive optics imaging (AO), and speckle interferometry, all capable of detecting angularly nearby stars that might be the source of the dimming that mimics a transiting planet around the target star. The AO and speckle techniques detect companions beyond a few tenths of an arcsec while the spectroscopy detects stars located within a few tenths of an arcsec. Thus these three techniques are useful to detect stellar companions located within a few arcsec of the target star, albeit with varying sensitivity. Below we describe the details showing that *none of the 22 KOIs revealed a companion star located within 4 arcsec and within 3 mag of the primary star. Thus the probability of both a background eclipsing binary and a background star with a transiting planet are significantly reduced for all of them, as described below.*

We analyzed the high resolution ($R=60,000$), high signal-to-noise ($\text{SNR} \approx 150$) optical spectra of all 22 KOIs for the presence of absorption lines from any second star besides the identified *Kepler* target star, as described and tested in detail in Kolbl & Marcy (2013). In brief, the entrance slit of the Keck-HIRES spectrometer had a width of 0.87 arcsec, allowing the light from any neighboring stars located within 0.4 arcsec to enter the slit. This of-

fers a detectability of companion stars not afforded by adaptive optics or speckle interferometry (see below). The algorithm fits the observed spectrum of the host star of the multi with the closest-matching member (in a chi-square sense) of our library of 800 AFGKM-type spectra stored on disk, spanning a wide range of T_{eff} , $\log g$, and metallicities. After proper Doppler shifting, artificial rotational broadening, and continuum normalization, and also flux dilution (due to a possible secondary star), that best-fitting primary star is subtracted from the observed spectrum.

The code then takes the residuals to that spectral fit and performs the same chi-square search for a "second" spectrum that best fits those residuals. This approach stems from an Occam's razor perspective, rather than immediately doing a self-consistent two-spectrum fit. The notion is that if one spectrum adequately fits the spectrum, without "need" to invoke a second spectrum, then the spectrum can only be deemed single. A low value of chi-square for the fit of any library spectrum (actually a representative subset of them) to the residuals serves to indicate the presence of a second spectrum. We establish a detection threshold by injecting fake spectra into the observed spectrum and executing the algorithm above to determine the value of chi-square for any relative Doppler shift, ΔRV between the companion star and the primary star that is approximately a 3-sigma detection of the secondary star. Figures 1- 22 show the resulting plot of chi-square vs ΔRV in search of a clear minimum that would signify a second spectrum. The blue and red lines show how low chi-square would be for a companion having 0.3% and 1.0%, respectively, of the optical flux of the primary, based on the injection of fake secondary spectra. None of the 22 KOIs shows evidence of a second star within 0.4 arcsec, at flux thresholds of $\sim 0.3\%$ of the flux of the primary star. There is a severe blind spot for $\Delta RV < 10 \text{ km s}^{-1}$ for which the absorption lines overlap, preventing effective detection of any companion stars. Thus, companion stars orbiting inward of ~ 5 AU are detectable by this technique, but companions farther out will have too small a ΔRV to be seen.

For all 22 KOIs in this paper, we have obtained adaptive optics imaging and speckle interferometry. Figures 23b- 44b show the detectability thresholds for companion stars to all 22 KOIs from these two techniques. None of the 22 KOIs shows a companion star located within 4 arcsec and within 3 mag of the primary star. Thus the probability of a background eclipsing binary is significantly reduced for all of them, as any such a binary must reside within the inner working angle of those techniques, typically a few tenths of an arcsec, depending on wavelength and technique (see Figures 23b- 44b). described above, becomes effective inward of ~ 0.4 arcsec, just where AO and speckle leave off. Thus this suite of techniques offers good coverage of companion stars at nearly all angular separations, except for bound stellar companions orbiting between 5-100 AU within which all of these techniques are poor.

6.5. Large False Positive Probability for KOI-104 and 1612

Two KOIs remain with large FPPs, namely KOI-104 and KOI-1612 worthy of comment regarding both the

astrophysical reason for their high FPP and for the additional observations that bear on (reduce) that probability of a false positive. We noted in ?? that use of the measured exclusion radius from centroidic analysis from the DV report drops the FPP considerably. Here we examine the two remaining cases with FPPs above 1%.

For KOI-104.01, the nominal FPP is 10.5% due largely to its relatively V-Shaped light curve (see Fig 26). The measured exclusion radius of 0.04 arcsec rules out background eclipsing binaries and background stars with transiting planets. But the dominant FP scenario of a bound eclipsing binary system remain possible. Here we consider whether that false positive scenario can be reduced based on follow-up observations.

The RVs for KOI-104 phase well with the ephemeris of the *Kepler* transiting planet (see Figure 26d, at lower right). All FP scenarios that involve a bound eclipsing binary that, when diluted by the primary star, cannot reproduce these phased RV measurements are ruled out. The RVs imply a planet mass of $10.8 M_{\oplus}$, consistent with the measured planet radius of $3.5 R_{\oplus}$. If the implied planet mass had been factors of 3 higher or lower, the planet hypothesis would have been called into doubt. But that was not the case. The phased RVs and the mutually consistent mass and radius for KOI-104.01 immediately rules out all eclipsing binary scenarios that fail to insidiously mimic the signal of the expected planet candidate. We are not prepared to calculate the factor by which eclipsing binaries are less likely as a result of this RV agreement with the *Kepler* transiting planet candidate, but it seems likely that the formal FPP must be reduced well below the nominal 10.5%. The RV phasing and mass agreement suggests (but does not prove) that the planet model is highly favored.

Further, the RVs reveal an outer companion (non-transiting) having $P = 822$ d and $M \sin(i) = 9.2 M_{JUP}$, implying a substellar mass, with an orbital eccentricity of $e=0.35$. Such a companion cannot itself be the cause of the repeated dimming (i.e. if it had a transiting planet) as the substellar mass can't contribute enough light to the total light from the system. More importantly, this orbiting companion around KOI-104 is apparently in a stable, eccentric orbit which surely reduces the probability that a stellar companion resides anywhere within orbital periods up to three times greater, i.e. out to periods of ~ 5 yr. Indeed, our spectra reveal no evidence of secondary lines (see section below). Therefore, all scenarios for a false positive that involve a companion star within 5 AU and a transiting object are ruled out, lowering the FPP further below 10.5%.

In addition, KOI-104 has adaptive optics (AO) images and speckle interferometry, neither of which shows evidence of a stellar companion, restricting further the possibility of a background eclipsing binary. Figure 26b shows the domain of angular distance and relative brightness of any companion that is ruled out. The IR AO images of KOI-104 eliminate the possibility of any neighboring star brighter than 1% the brightness of the primary star beyond 1 arcsec, and eliminate neighboring stars brighter in Ks-band (2.2μ) than 1% of the primary. The speckle observations eliminate companions beyond 0.2 arcsec brighter than 2.5% of the primary. These high contrast imaging efforts are much more restrictive than the 2 arcsec radius blind spot for companion stars as-

sumed by the nominal FPP calculation (SS6.4). The non-detections by high contrast imaging of second stars reduces the probability of a background star (with either a transiting planet or eclipsing star) by a factor of at least 10 (ratio of areas). However, as Table 3 shows, the dominant false positive scenario for KOI-104 is by a hierarchical (bound) stellar companion that are not effectively ruled out by the high contrast imaging. Thus, the FPP for KOI-104 remains formally near 10%, even after including the imaging and centroid analysis.

For KOI-1612.01 the formal FPP is 39% due almost entirely to the chance of a background eclipsing binary (see Table 3). The main reason for this high FPP is that the signal duration is only ~ 1.4 hours, even though the orbital period is 2.4 d orbit around a star of radius $1.23 R_{\odot}$. This observed transit duration is shorter than expected for such a transit and star, unless the impact parameter is near unity which is unlikely. The star field is indeed crowded, and the astrometric centroid diagnostics are understandably ambiguous. This light curve of such short duration could instead be caused by a eclipsing binary around a smaller star in the background. Moreover, the transit light curve for KOI-1612 is shallow, with a fractional depth of only 0.00003 (see Figure 43e), leaving fractional noise high enough to allow a wide variety of false-positive scenarios. We consider KOI-1612.01 to be as likely a false positive as a planet. Statistically, we expect a false-positive frequency of $\sim 5\text{-}10\%$ in our sample of 22 KOIs (Morton & Johnson 2011; Morton 2012; Fressin et al. 2013). Therefore it is not surprising that one member of this sample, KOI-1612, has a 40% probability of being a false positive, as one was expected a priori.

7. INDIVIDUAL KOIS: OBSERVATIONS, ANALYSIS, AND PLANET PROPERTIES

For each KOI, we provide here a detailed description of its *Kepler* light curve, the multiple follow-up observations with chronological reasoning, an overview of the data analysis, and the resulting masses, radii, densities, and orbits of the planets. The ground-based follow-up observations were made by the *Kepler* "Follow-up Observation Program" (KFOP) from 2009-2012, (Gautier et al. 2010) with a few additional observations made during the era after the end of the nominal *Kepler* mission deemed the "Community Follow-up Observing Program" (CFOP). Most of these observations are publicly available on the CFOP website:

cfop.ipac.caltech.edu/home/login.php

We have already summarized the telescopes and instruments that were used to collect high resolution (but low SNR) "reconnaissance" (hereafter "recon") spectra and high resolution imaging in Section 2. Here we summarize the full set of follow-up observations with their chronological rationale and the results for each KOI that led to successive acquisition of diagnostics about the planet and host star.

These observations were used to characterize the planets via their host stars, and to illuminate any false positive scenarios as described in Section 6, such as eclipsing binaries or background stars with transiting planets, that would be spatially blended with the target star. The observations and analysis for the low signal-to-noise, high

resolution advanced “recon” spectroscopy is described in (Buchhave et al. 2012). The high resolution imaging with speckle is described in (Howell et al. 2011), and the adaptive optics (AO) is described in Adams et al. (2012). The methods used to determine the final stellar parameters, using either asteroseismology (Huber et al. 2013) or LTE spectroscopic analysis with the SME code and Yonsei-Yale stellar models (see Section 3) are described for each KOI. The high signal-to-noise (typically 200:1 per pixel), high-resolution ($R = 60,000$) Keck-HIRES optical spectra acquired for each of the KOIs are used to determine the final stellar parameters, found in Table 1. The planet and orbital properties are reported in this section for individual KOIs and compiled in Table 2. The summaries for each KOI below are also intended to provide a snapshot of the observing notes and information available as of May 2013.

7.1. KOI-41

Three transiting planets have been detected by *Kepler* around KOI-41 with orbital periods of 6.9(41.02), 12.8(41.01), and 35.3(41.03) days, having planet radii of 1.3, 2.2, and $1.6 R_{\oplus}$, respectively. After detection of the transiting planets, a recon spectrum was taken at the McDonald 2.7m telescope in June 2009, followed by another at the Tillinghast 1.5m telescope in late June 2009, and both were analyzed with the spectroscopic analysis package, “SPC” Buchhave et al. (2012). The resulting values of T_{eff} and $\log g$ were found to be consistent with those in the *Kepler* Input Catalog (KIC), no large RV variations (over 1 km s^{-1}) were found, and the rotational Doppler broadening, $v \sin i$, was found to be less than 4 km s^{-1} . The Keck-HIRES template spectrum (no iodine in the beam), was analyzed with SME and the output values of T_{eff} and $[\text{Fe}/\text{H}]$ were used to constrain the asteroseismology analysis coupled with stellar interiors modelling to yield stellar mass and radius. A subsequent iteration between SME and asteroseismology brought a quick convergence of stellar mass and radius. The final stellar parameters are $T_{\text{eff}} = 5825 \pm 75 \text{ K}$, $\log g = 4.13 \pm 0.03$, $v \sin i = 3.7 \pm 1.0 \text{ km s}^{-1}$ and $[\text{Fe}/\text{H}] = 0.02 \pm 0.10$. The complete list of final stellar parameters are found in Table 1.

High resolution imaging was acquired in May 2010 with the ARIES AO system on the MMT, under seeing of $0.1''$ in the Ks band and $0.2''$ in the J-band. Speckle imaging was taken at the WIYN telescope in June 2010. (Citations for all instruments are given at the beginning of Section 7.) Neither imaging technique found any nearby companion stars within $6''$ of the primary. Figure 23b shows the limiting magnitudes achieved with each high resolution imaging method. Figure 23a shows a seeing limited image of the field of view of the HIRES guide camera.

The low rotational line broadening ($v \sin i$) and the lack of nearby stellar companions made KOI-41 a high quality target for precise radial velocity (RV) measurements with Keck-HIRES, which began 29 July 2009 and span 1221 days (Figure 23c), garnering 44 precise RVs. The RVs show a weak correlation with the ephemeris of the 6.9d transiting planet identified by *Kepler*, limiting the planet mass to be less than $9.6 M_{\oplus}$ at the one sigma level. This upper limit to the planet mass corresponds to a bulk density of the planet of 20.5 g cm^{-3} . Since this density is

greater than any known material the limit is not physically meaningful. Additional RV observations could push this limit lower.

The RVs also do not correlate with the ephemeris of the 12.8 day transiting planet from *Kepler* photometry, but the upper limits to the planet mass are physically meaningful. The one sigma upper limit to the mass is $4.8 M_{\oplus}$, corresponding to a bulk density of 2.0 g cm^{-3} . If this planet consists of large amounts of dense material, such as iron with an expected density near 10 g cm^{-3} , the RV signal would have been much larger and we would have detected it. Instead, this planet must consist of a large portion of lighter materials. These measurements are consistent with the trend of planet radii greater than $2.0 R_{\oplus}$ having low density ($< 3.0 \text{ g cm}^{-3}$). The RVs also do not correlate with the 35 day planet ephemeris. The peak value in the posterior distribution of the planet mass is below zero, meaning that the measured mass is consistent with zero. The one sigma upper limit on the planet mass is $1.7 M_{\oplus}$ and 1.9 g cm^{-3} . Figure 23d shows the phased RVs for each planet.

The full set of RVs are plotted in Figure 23c and listed in Table 4, along with chromospheric R'_{HK} values measured from the same spectra as the RVs, making them simultaneously obtained.

7.2. KOI-69

KOI-69 has one transiting planet with a period of 4.7 days and a radius of $1.5 R_{\oplus}$. A linear trend of 10 m/s/year is seen in the RVs, and over the course of 3 years the RVs show no departure from a straight line. Follow up recon spectroscopy commenced in August 2009 at McDonald 2.7m and the 2.6m Nordic Optical telescope. Moderate signal-to-noise spectra were acquired, yielding spectral parameters found with SPC consistent with the values in the KIC. The $v \sin i$ was measured to be $< 2 \text{ km s}^{-1}$, consistent with a slowly rotating main sequence star, and no RV variation was seen between the two spectra at the 500 m s^{-1} level. SME analysis on the Keck-HIRES template spectrum showed the star to be slightly cooler than the KIC and recon-determined parameters. Final stellar parameters including stellar mass and radius were calculated using asteroseismology with SME values used as input parameters, along with the usual iteration between the two. The final stellar parameters are $T_{\text{eff}} = 5669 \text{ K}$, $\log g = 4.47$ and $[\text{Fe}/\text{H}] = 0.02$. Table 1 holds the final stellar parameters including stellar mass and radius.

Speckle imaging was first obtained in October 2009 and a binary companion was suggested $0.05''$ away with a delta magnitude of 1.4. Two additional speckle images were taken and the secondary star was not detected. A warning of this companion appears in Table 3 of Borucki et al. (2011) but should be disregarded. Adaptive optics imaging in May 2010 at MMT-ARIES confirmed no secondary stars were present from $1''$ - $6''$ of the primary, but the putative $0.05''$ companion would have fallen within the inner working angle of ARIES. The field of view near this KOI is shown in a Keck-HIRES guide camera, which is a seeing limited image shown in Figure 24a. Limits on companions from the high resolution imaging are displayed in Figure 24b.

Keck-HIRES precise RVs span 1132 days, from July 2009 to September 2012 (Figure 24c). The most promi-

inent feature in the RVs is the 10m/s/year linear trend. Since we see no curvature, we can declare that the orbital period of the companion causing the linear trend is longer than the time baseline of nearly four years. The most likely orbital companion is an M-dwarf orbiting beyond 5 AU. The non-transiting planet has a designation of 69.10 and we place lower limits on the mass and period ($M > 2 \text{ MJUP}$ and $P > 3 \text{ yr}$) in Table 1.

We place upper limits on the mass of the transiting planet at $4.4 M_{\oplus}$, which corresponds to a bulk density of 7.2 g cm^{-3} . This is only an upper limit because the median value of the posterior distribution of the MCMC analysis of the planet mass is near zero, and the value is consistent with zero at the two sigma level. The phase folded RV curve shows the K-amplitude of $1.05 \pm 0.8 \text{ m s}^{-1}$ (Figure 24d), not significant at better than 1-sigma. The full set of RVs is plotted versus time in Figure 24c and listed along with R'_{HK} activity values in Table 5.

7.3. KOI-82

The five planets in this system have periods of 5.2 (82.05), 7.1 (82.04), 10.3 (82.02), 16.1 (82.01) and 27.5 (82.03) days and have corresponding radii of 0.5, 0.6, 1.0, 2.2 and $0.9 R_{\oplus}$. Due to their very small transit depths of only 41 and 65 parts ppm, 82.05 and 82.04 were detected last. Their numbering reflects their order of discovery of course, not their orbital period.

Recon spectroscopy was first acquired with the Lick 3m telescope in August 2009. Two spectra taken four days apart gave stellar values in agreement with the KIC value for T_{eff} , but the value of $\log g = 5.0$ conflicted with the KIC $\log g$ value of 4.0. The final stellar parameters determined with SME analysis combined with stellar models and light-curve fits are $T_{\text{eff}} = 4903 \pm 44 \text{ K}$, $\log g = 4.61 \pm 0.03$ and $[\text{Fe}/\text{H}] = 0.02 \pm 0.10$. The final $\log g$ value and stellar mass changed the KIC value of stellar radius from $1.8 R_{\odot}$ to $0.73 R_{\odot}$. The initial values of planet radii were likewise reduced by a factor of 2.5.

Due to the intense interest in the system of five small planets, and the recon derived stellar parameters that differed greatly from the KIC values, high resolution spectra were taken at Keck/HIRES as well as FIES to confirm the stellar properties. Several trials of SME analysis and SPC analysis were made to robustly confirm the T_{eff} , $\log g$, and $[\text{Fe}/\text{H}]$. In the end all analyses agreed within one sigma errors, given above.

Standard follow-up with speckle imaging in June 2010 and ARIES AO observations in September 2010 found no stellar companions within their detection domains, supporting the notion that the transits occur on the primary star or a bound companion star. Figure 25a shows a seeing limited image of the field of view from the Keck-HIRES guider image. Figure 25b shows the limiting magnitudes achieved with each imaging method.

With five transiting planets in orbits less than 25d and planet radii less than $2.5 R_{\oplus}$, KOI-82 is a densely packed, rich system of small planets. The RV time baseline of nearly 900 days shows only a 4.3 m s^{-1} scatter prior to fitting the orbits with circular models (Figure 25c), covering many orbits of even the longest period planet in the system. We fit all five planets simultaneously with circular orbits and find the 16-day planet (KOI-82.01) shows the strongest coherence with the RVs.

We measure the planet mass at $8.9 \pm 2.0 M_{\oplus}$ and a density of $4.7 \pm 1 \text{ g cm}^{-3}$. The RV semi-amplitude, K , is $2.8 \pm 0.6 \text{ m s}^{-1}$, the largest for any planet in the system. The four remaining planets in the system are below the current RV detection threshold, and we report one sigma upper limits to their masses in Table 2. With the three year time baseline, we constrain the presence of non-transiting planets out to 5AU with masses down to one Jupiter mass. No detectable periodic signals are seen in the residuals to the five planet fit. The full set of RVs are listed, along with their R'_{HK} activity values, in Table 6.

7.4. KOI-104

The single transiting planet orbiting KOI-104 has a period of 2.5 days and radius of $3.5 R_{\oplus}$. It resides in a multiple planet system, as precise RVs reveal the presence of a non-transiting planet(104.10) with a period of 821 ± 3 days and $M \sin i$ of $10.2 \pm 0.6 \text{ MJUP}$. Before the non-transiting planet was detected, we acquired the usual suite of follow up observations. Recon spectroscopy was first done with the 2.6m Nordic Optical Telescope in August 2009. The three spectra that were acquired showed no radial velocity variation above the errors of 200 m s^{-1} , indicating the host star to be a slowly rotating cool dwarf.

Initial photometric analysis based on KIC stellar parameters yielded a star and planet radius smaller by 20% than the final planet radius. The slowly rotating K-type host star was recognized as ideal for precise RV spectroscopy. SME analysis of the HIRES template spectrum and comparison to Yonsei-Yale stellar models refined the stellar properties to be $T_{\text{eff}} = 4781 \pm 78 \text{ K}$, $\log g = 4.59 \pm 0.04$ and $[\text{Fe}/\text{H}] = 0.34 \pm 0.04$, confirming the stellar parameters determined from the recon analysis. The final planet radius is $3.5 R_{\oplus}$, stemming from our usual MCMC modeling of light-curve and RVs and after adopting the final stellar radius. KOI-104 was analyzed by (Muirhead et al. 2012), but the parameters were found to be very uncertain with their method, which is best for mid to late M dwarfs having $\text{Teff} < 4000 \text{ K}$. The final stellar parameters can be found in Table 1.

The "V-shaped light curve" led the KFOP to adopt caution regarding the planet interpretation. The Kepler photometric diagnostics suggested a chance that this was a blend of two or more stars. Speckle imaging revealed no companions within its limits. Subsequent AO observations taken at Palomar further limited the presence of stellar companions to within $1.0''$ away from the primary. The concerns regarding the V-shaped transit and possible blend of other stars cause the nominal false positive probability to be 10%, as described in detail in Section ??.

As described there, the RV detection of the 2.5d planet is consistent with a transiting planet, limiting the plausible false-positive scenarios that would insidiously mimic both the light curve and RVs of a transiting planet. For a detailed description of the FPP for this KOI, see Section 6.5.

A seeing limited image of the field of view from the Keck-HIRES guider is found in Figure 26 while Figure 26b shows the limiting magnitudes achieved with each high resolution imaging method. No stellar companions were found.

The first Keck-HIRES RV was acquired on 30 June 2010. The long baseline of the RVs, spanning 800 days (Figure 23c), was vital for mapping out the orbit of the non-transiting planet. The precise RVs are in phase with the transiting planet in a circular orbit, and we measure the planet mass to be $10.8 \pm 1.4 M_{\oplus}$. The transiting planet mass, combined with the planet radius measurement from *Kepler* yields a bulk density of $1.45 \pm 0.3 g cm^{-3}$, which is consistent with theoretical expectations by Lopez et al. (2012), and suggests a low density planet with a large fraction of volatiles by volume. While the planet radius and mass quoted above stems from a circular orbit model, the transiting planet appears to be in a non-circular orbit, despite its short period. It is one of the few cases in which a non-zero eccentricity is clearly called for, allowing a better fit to the RV data, than the circular orbit (See Appendix). The higher RV variation is due to the non-transiting planet, and we measure $M \sin i$ of that planet to be $10.2 \pm 0.6 M_{JUP}$. This planet also has a non-circular orbit and we measure the eccentricity to be $e=0.38$. The phase folded RV curves are shown in Figure 26d.

The eccentricity of the short period planet is unusual. Perhaps the non-transiting planet is pumping the eccentricity of the transiting planet. It is worth noting that there is only one transiting planet, perhaps because the non-transiting planet has scattered other planets out of the original protoplanetary plane. The most likely $M \sin i$ for the non-transiting planet $10 - 20 M_{JUP}$, and the actual planet mass is probably higher because we only know $M \sin i$, not the true mass. The full set of RVs are listed, along with R'_{HK} values, in Table 7.

7.5. KOI-108

The two planets around KOI-108 have periods of 16.0(108.01) and 180(108.02) days with planet radii of 3.4 and $5.1 R_{\oplus}$, respectively. Follow-up observing at the McDonald 2.7m in August 2009 were found to be in marginal agreement with the KIC estimates of T_{eff} and $\log g$. SME analysis was conducted on a Keck-HIRES template spectrum. The results were used as initial conditions in the asteroseismology analysis, which determined the final stellar parameters, most notably increasing the stellar radius by 25% from the KIC radius to $1.43 R_{\odot}$. The derived stellar parameters are $T_{\text{eff}} = 5845 \pm 88$, $\log g = 4.16 \pm 0.04$, and $[\text{Fe}/\text{H}] = 0.07 \pm 0.1$. The small number of RV measurements in 2012 is due to the refined stellar parameters, which increased the planet radii to $> 3.0 R_{\oplus}$, above our target range of planet radii.

Adaptive optics imaging was acquired in the J-band at Palomar Observatory and two nearby stars were found $2.44''$ and $4.87''$ from the primary, both are 7.2 magnitudes fainter than the primary. No companion stars were found within the limits of speckle imaging, taken in June 2010, which probes from $0.05''$ to $1.4''$ from the primary. During Keck-HIRES observations, the $4.87''$ stellar companion was purposely kept out of the HIRES slit, however the $2.76''$ companion was not visible on the HIRES guider and may have inadvertently fallen into the slit of the spectrometer. The HIRES slit is only $0.87''$ wide, so for most orientations of the rotating HIRES field of view (due to use of the image rotator) the star would not fall in the slit. If it did, then the flux would be $> 1/700$ the brightness of the primary. Figure 27a shows a seeing limited

image of the field of view of the HIRES guider camera. Figure 27b shows the limiting magnitudes achieved with each high resolution imaging method.

The second transit of the 180d planet was found only after a full year of Kepler data was analyzed. Upon discovery of the first transit event of the 180d planet, centroid analysis was conducted and found the flux weighted centroid shift offset from the primary star by $0.7''$ at the two sigma level. After more Kepler photometry was processed and analyzed, the offset was not confirmed, and the centroid analysis was found to be consistent with a transit on the target star.

The time baseline for the RVs spans 735 days (Figure 27c). The RV signal correlates with the orbital period of 16 days for the inner planet. The nominal mass of the 15 day planet is measured to be $18.7 \pm 4.6 M_{\oplus}$, corresponding to a bulk density of $2.2 \pm 0.6 g cm^{-3}$ when combined with the planet radius of $3.4 R_{\oplus}$. The RV signal has a semi-amplitude of $3.7 \pm 0.9 m s^{-1}$, a strong detection by our standards in this paper. Since RV measurements are planned to occur at the predicted times of quadrature, the phase coverage of the RVs is poor, and the eccentricity is not well constrained, leading us to conduct these fits using circular orbits. The peak of the posterior distribution of the 180 day planet is negative, and the interpretation is that the results are consistent with zero, and the upper limits on this non-detection are not physically meaningful (a planet cannot have negative mass). Poor phase coverage of the RVs for this long period planet make upper mass limits even less robust. The full set of RVs are listed, along with their R'_{HK} activity values in Table 8.

7.6. KOI-116

With four transiting planets with very small transit signals, KOI-116, *Kepler* was slow to discover the full quartet of planets. The final makeup of the system is four planets with periods of 6.2(116.03), 13.6(116.01), 24.0(116.04) and 43.8(116.02) days and planet radii equal to 0.8 , 2.5 , 0.95 and $2.6 R_{\oplus}$, respectively. The first two planets were discovered with three months of Kepler data, the third required quarters 1-6 of Kepler data, and the fourth was discovered with quarters 1-8 of Kepler data. The longer time baselines of the *Kepler* photometry are required to find such small signals. Ground based follow-up observing started with acquisition of Recon spectra with the 2.6m Nordic Optical Telescope in August 2009 and the McDonald 2.7m in September 2009. These spectra agreed with the T_{eff} from the KIC, but modified the $\log g$ from 4.0 to 4.5, placing this star on main sequence, not slightly evolved. The main effect of this change in gravity is the decrease of the stellar radius by 50% compared to the KIC value to $1.04 R_{\odot}$. The planet radii were likewise decreased from $5 R_{\oplus}$, to their final values stated above and in Table 2. SME analysis on a HIRES template spectrum was used in combination with Yonsei-Yale stellar isochrones to determine the final stellar parameters of $T_{\text{eff}} = 5858 \pm 98 K$, $\log g = 4.407 \pm 0.14$, and $[\text{Fe}/\text{H}] = -0.12 \pm 0.1$. (Table 1).

To complete the suite of follow-up observing, speckle imaging at WIYN taken in June 2010 and AO observation taken at ARIES in Ks band in late 2010, both showed no companion stars within their detection limits. Figure 28a shows a seeing limited image of the field of

view of the HIRES guide camera. Figure 28b shows the limiting magnitudes achieved with each high resolution imaging method.

While precise RV monitoring started in 2010, the discovery of the fourth planet, and the adjustment of all four planet radii to values below $2.5 R_{\oplus}$ lead to increased cadence in the 2012 observing season. The RV baseline of 1073 (Figure 28c) reveals no non-transiting planet signals or linear trends. The 6d(.03) and 24d(.04) planets have RV signatures below the detection threshold of the RVs, the K-amplitude values from the 4 planet fit is consistent with zero and the upper limits are quite weak. The 13 day planet, with radius of $2.5 R_{\oplus}$, shows a modest correlation with the RVs that allows us to determine a mass value of planet mass = $10.4 \pm 3 M_{\oplus}$, corresponding to a $3.3 \pm 1.6 g cm^{-3}$. The 43 day planet, with a radius of $2.6 R_{\oplus}$, shows a weaker correlation with the RVs, and we are able to measure the mass of $11.2 \pm 6 M_{\oplus}$, density = $3.1 \pm 2.1 g cm^{-3}$. The 13 day planet has a slightly better than 2-sigma detection, while the 43 day planet is slightly less than a 2-sigma detection. While we cannot place strong upper limits on the mass of the two sub-earth radius planets, the RVs are completely consistent with the four planet system. The phase folded RV curves for each planet are shown in Figure 28d. The full set of RVs are listed, along with their R'_{HK} activity values in Table 9.

7.7. KOI-122

KOI-122 is a single planet system, in which the sole planet orbits its host star in 11.5 days and has a radius of $3.4 R_{\oplus}$. The first follow-up observations were two spectra taken in August of 2009 at the McDonald 2.7m. Compared to the KIC values, the T_{eff} measurement agrees with the KIC value, but the $\log g$ value differs significantly. The final stellar radius of $1.41 R_{\odot}$ is 75% larger than the KIC value. SME performed on a Keck-HIRES spectrum, combined with asteroseismology (Huber et al. 2013) provides the final $\log g$ has a value of 4.17 ± 0.04 , $T_{\text{eff}} = 5858 \pm 98$ and $[\text{Fe}/\text{H}] = -0.12 \pm 0.1$. The corresponding adjustment to the planet radius (originally $1.9 R_{\oplus}$), moved this KOI out of our target range of planet radii, which is focused on planets smaller than $2.5 R_{\oplus}$. Precise determination of the stellar radius is critical to the final planet mass and density determination. For example, by combining the planet radius from 2009 with the current mass measurement leads to a planet of density = $24 g cm^{-3}$, while the asteroseismically determined value of planet radius, combined with the RV mass measurement shows this planet to be low density ($< 2.0 m s^{-1}$).

Follow-up imaging with the WIYN telescope in August 2009 found no stellar companions, but AO imaging at Palomar in June 2010 revealed a single companion star $4.1''$ from the primary that is 6.5 magnitudes fainter in the J-band. Centroid analysis of this target rules out the possibility of the transit occurring on the companion star. Figure 29a shows a seeing limited image of the field of view of the HIRES guide camera. Figure 29b shows the limiting magnitudes achieved with each high resolution imaging method.

The precise RV baseline from Keck-HIRES spans 1078 days has an RMS of $5.1 m s^{-1}$ (Figure 29c). After fitting the single planet, of radius = $3.4 R_{\oplus}$, to the RVs

we strongly detect the mass to be $13.0 \pm 2.9 M_{\oplus}$ with a corresponding density of $1.7 \pm 0.4 g cm^{-3}$. The density determination is consistent with that found in Table 4 of Lopez et al. (2012). The RV detection is significant, and the low density requires the planet to consist of a large fraction of volatiles by volume.

The full set of RVs are listed, along with their R'_{HK} activity values in Table 10.

7.8. KOI-123

The KOI-123 planetary system consists of two transiting planets with orbital periods of 6.5(123.01) and 21(123.02) days and radii of 2.4 and $2.5 R_{\oplus}$, respectively. Two spectra were acquired at the McDonald 2.7m in August 2009. No RV variation of order $500 m s^{-1}$ was seen over the 18 days between the two observations, and the T_{eff} and $\log g$ values agree, within errors, with the KIC values. The rotational velocity of $4 km s^{-1}$ showed this to be a good target to follow-up with precise RVs. The template spectrum from Keck-HIRES was used to determine the stellar parameters with SME, which are used as inputs to the asteroseismology analysis. The final stellar parameters are $T_{\text{eff}} = 5952 \pm 75$, $\log g = 4.21 \pm 0.04$, and $[\text{Fe}/\text{H}] = -0.08 \pm 0.1$. The stellar parameters from the KIC, recon spectra, and SME/asteroseismology are all in agreement, and no large modifications to the stellar radius, and subsequently, the planet radii, were needed.

In September 2009 AO imaging at Mt. Palomar detected two stellar companion in the J-band, located $2.03''$ and $5.27''$ away from, with delta magnitudes of 7.4 and 8.1. Speckle imaging was acquired in June 2010, and no additional companions were found. The two companions found with AO are beyond the detection limits of speckle. Centroid analysis of the *Kepler* photometry excludes the possibility that the transits fall on either of the known companion stars. Figure 30a shows a seeing limited image of the field of view of the HIRES guide camera. Figure 30b shows the limiting magnitudes achieved with each high resolution imaging method.

The 1100 day precise RV baseline shows a $7.1 m s^{-1}$ RMS (Figure 30c), and the RVs do not correlate in phase with either planet (Figure 30d). We provide mass measurements, which serve more as mass limits, for each planet. The nominal planet masses are $1.3 \pm 5.4 M_{\oplus}$ and $2.2 \pm 7.8 M_{\oplus}$ for the inner and outer planets respectively. The correspondingly low density limits of $0.3 \pm 2 g cm^{-3}$ and $0.6 \pm 2.3 g cm^{-3}$ are consistent with zero, however the upper mass limits for the 21 day planet suggest a composition of mostly rocky material is very unlikely. Such a planet would have a mass that is easily within the detectability of the measurements in hand. The density determinations are not inconsistent with the Lopez et al. (2012) results, but with the current uncertainties, a proper comparison must wait.

The full set of RVs are listed, along with their R'_{HK} activity values in Table 11.

7.9. KOI-148, Kepler-48

This four planet system, has three transiting planets with orbital periods of 4.8(148.01), 9.7(148.02) and 43(148.03) days with radii equal to 1.9 , 2.7 and $2.0 R_{\oplus}$, respectively and one non-transiting planet with an orbital period of 972 days(148.10) and minimum mass of $M \sin i = 2.1 \pm 0.08 M_{JUP}$. Follow-up observations of this

system began with the acquisition of three recon spectra from the Lick 3m and McDonald 2.7m. The spectral analysis of the recon spectra conducted with SPC found this star to be a slowly rotating main sequence K0 star, confirming the KIC parameters and adding the knowledge of $v \sin i < 2 \text{ km s}^{-1}$. When we started collecting precise RVS with Keck-HIRES, SME analysis was conducted on the template spectrum. When combined with Yonsei Yale stellar isochrones, SME found $T_{\text{eff}} = 5194 \pm 43$, $\log g = 4.49 \pm 0.05$ and $[\text{Fe}/\text{H}] = 0.17 \pm 0.04$. Final stellar parameters are listed in Table 2.

High resolution imaging at WIYN using the speckle camera found no stellar companions. Adaptive optics imaging at Mt. Palomar probed the field of view beyond the speckle imaging revealing four companions within 6" of the primary. They are as follows: 2.44" away and delta magnitude of 4.9, 4.32" away and delta magnitude of 3.3, 4.39" and delta magnitude 7.3, and 5.89" away delta magnitude of 7.0. These observations were conducted in the J-band and probe down to a Kepler Magnitude of 20.7(Adams et al. 2012). All of these companion stars are identifiable in the Keck guide camera and care was taken keep these stars from entering the slit during precise radial velocity observations, however line bisector variations of a few observations suggest that the nearest companion could have lied along the slit on three occasions [Geoff, Do we need to consider this further?]. Centroid analysis of the Kepler photometry definitively shows that the transits occurred on the primary star, and not on any of the companion stars. Figure 31a shows a seeing limited image of the field of view from the Keck guide camera. Figure 31b shows the exclusion limits from the high resolution imaging analysis.

This three transiting planet system was observed with Keck/HIRES starting in August 2009(Figure 31c). The initial epochs in summer 2009 would prove vital for detecting the non-transiting planet in a nearly 3-year orbit. Further radial velocity measurements will more tightly constrain the orbital parameters of the non-transiting planet, which will likewise improve the transiting planet masses.

The 4.7 and 9.7d planets have been shown to be gravitationally interacting, in a 2:1 mean motion resonance, as measuring by their TTVs (Steffen et al. 2013; Wu & Lithwick 2012). Steffen et al. (2013) performs a stability analysis to calculate the possibility of these two inner planets as false positives, leading to a FPP of less than 10^{-3} . This agrees with the Morton (2012) analysis listed in Section 2.3 and Table 3. The planet in the 43d period does not gravitationally interact with the inner planets in a way that leads to a detectable signal. The masses of the two interacting planets have been measured with TTVs, but with a different stellar parameters and different planet radii, making a direct comparison here difficult.

The maximum mass for KOI-148.01 and KOI-148.02, as allowed by the stability analysis are several jupiter masses each. These mass values are further constrained with a TTV analysis which results in maximum masses of 17.2 ± 3.9 and $10.1 \pm 3.5 M_{\oplus}$, for 148.01 and 148.02, respectively. Radial velocity measurements currently find the masse of $3.9 \pm 1.9 M_{\oplus}$ and $14.9 \pm 2.9 M_{\oplus}$. Phase folded RV curves for each planet are shown in Figure 31d. Radial velocities constrain the mass of .01 more

tightly than TTV analysis. The mass determined for KOI-148.02 is consistent between the two methods within errors. A joint analysis using both TTVs and radial velocities would likely constrain the masses even more.

After the second observing season, a linear trend in the RVs was detected. After the third year of observing the RV trend turned over and the period of the non-transiting planet was known to within a factor of two. Only after the fourth year of observations and a full orbit of the non-transiting planet had occurred, was the period known to better than 10%. The existing 10% uncertainty in the non-transiting planet makes it more difficult to precisely fit the transiting planets. As the orbital parameters, especially eccentricity, of the non-transiting planet are further constrained with more observations, the masses of the inner planets will be more tightly constrained.

The full set of RVs are listed, along with their R'_{HK} activity values in Table 12.

7.10. KOI-153

This three planet system has two transiting planets with orbital periods of 8.9(153.01) and 4.7(153.02) days with radii equal to 2.2 and $1.8 R_{\oplus}$ and a non-transiting planet detected with RVs with a period of 16.4 ± 0.8 [double check period] days and $M \sin i = 30 \pm 4 M_{\oplus}$ [double check mass]. Recon spectra of this system were taken at the 2.6m Nordic Optical Telescope and McDonald 2.7m in August and September 2009. Using SPC, stellar parameters of T_{eff} and $\log g$ were confirmed to be within the errors of the KIC values, and no large RV scatter was found. This star was confirmed to be a slowly rotating K3V star, making it a good for precise RVs with Keck-HIRES. The main drawback of this KOI is its faintness of Kepmag = 13.5. The final stellar parameters, determined with SME and reference to Yonsei-Yale isochrones determined the stellar radius to be 30% less than the KIC value, with an equal decrease in the determination of the planet radii. The final stellar parameters are $T_{\text{eff}} = 4725 \pm 44\text{K}$, $\log g = 4.64 \pm 0.03$ and $[\text{Fe}/\text{H}] = 0.05 \pm 0.04$.

Speckle imaging at the WIYN in June 2010 found no companions within its limits. Adaptive optics imaging taken with ARIES in the 2011 observing season found one companion within 6.0". It was found in both the Ks and J bands at 5.14" from the primary with delta magnitudes of 8.1 and 8.3 respectively. Seeing on the night of this observation was only 0.3", slightly greater than the 0.1" observing conditions for most KOIs observed with ARIES. Figure 32a shows a seeing limited image of the field of view of the HIRES guide camera. Figure 32b shows the limiting magnitudes achieved with each high resolution imaging method.

We detect the 4.7 day transiting planet and the non-transiting planet with precise RVs that span a baseline of 832 days(Figure 32c). The 8.9 day transiting planet is not detected and we provide an upper limit to its mass. We find the mass of the 4.7d planet to be $7.1 \pm 3.3 M_{\oplus}$, and $6.6 \pm 3 g \text{ cm}^{-3}$. The upper limit to the 8.9d planet is difficult to interpret because the peak in the posterior distribution is -2.7 m s^{-1} . If the posterior distribution peaks near zero for K-amplitude or mass, then upper limits are calculated as the one sigma away from the mean in the positive direction. When the peak in the

posterior distribution of K-amplitude is negative, the interpretation is difficult because a value that is one-sigma from the median can still be negative. The reader should keep this in mind when interpreting the mass limit of the 89d planet. In determining the properties for the non-transiting planet, we searched for periodicities in the RVs that correspond the five highest peaks in the periodogram. The best fit period for a non-transiting planet is 16.4 days, with an uncertainty of only 0.02 days. The small uncertainty is a tribute to the long time baseline of the RVs. The best fit minimum mass of the 16.4 day planet is $M \sin i = 30.0 \pm 4 M_{\oplus}$. Inclusion of the non-transiting planet in the RV fit reduces the RMS to fit by a non-negligible amount, showing that the fit is better with the non-transiting planet included.[more needs to be said about the eccentricity limits on the .10 planet]

The full set of RVs are listed, along with their R'_{HK} activity values in Table 13.

7.11. KOI-244, Kepler-25

This three planet system has two transiting planets with orbital periods of 12.7(244.01) and 6.2(244.02) days with planet radii equal to 5.2 and 2.7 R_{\oplus} and a non-transiting planet in a period of 123 ± 2 days and minimum mass of $M \sin i = 90 \pm 14 M_{\oplus}$. Follow-up observations were begun with the acquisition of two recon spectra at the McDonald 2.7m and one at FLOW, all in March 2010. The stellar parameters determined from these spectra agree, within errors, with the KIC values. This is a non-typical RV target in the sense that with a $v \sin i = 10 \text{ km s}^{-1}$, and $T_{\text{eff}} = 6270\text{K}$. It is rotating faster and has a higher temperature than we normally choose to observe. Brightness(KepMag = 10.7) plays a role in choosing to observe this star, and its fast rotation increases the chance of measuring a Rossiter-McLaughlin signal. The final stellar parameters, which basically agreed with the KIC values, were obtained using SME conducted on a Keck-HIRES spectrum. SME results were combined with asteroseismology analysis and the detection of solar like oscillations were used to determine the stellar properties (Huber et al. 2013). The final stellar parameters are $T_{\text{eff}} = 4725 \pm 44\text{K}$, $\log g = 4.64 \pm 0.03$, and $[\text{Fe}/\text{H}] = 0.05 \pm 0.04$, which are listed in full, in Table 1.

Follow-up imaging conducted at the WIYN and Mt. Palomar found no companions, within limits, from 1" to 6" from the target. While there was once discussion on the CFOP regarding a false positive due to centroid motion for this KOI, further analysis ruled this out to within 2.0" or half a Kepler pixel. The confusion was due to this being a saturated target on the Kepler Field of View. Figure 33a shows a seeing limited image of the field of view of the HIRES guide camera. Figure 33b shows the limiting magnitudes achieved with each high resolution imaging method.

Gravitational interactions between the two inner planets has been evidenced by TTVs and documented by Steffen et al. (2012) and Wu & Lithwick (2012). In his analysis, Steffen et al. (2012) performs a stability analysis of the orbits and uses stability as a proxy for false positive assessment. The false positive probability from the stability analysis is 10^{-3} , compared to 1% and 0.001 from the Morton (2012) method discussed in Section 6, and found in Table 3. The masses are also constrained

by TTVs, but the RVs presented here constrain the mass by a factor of 100 better than the TTVs.

Extensive precise RV follow-up was carried out at Keck-HIRES from 2009 to 2012(Figure 33c), including two separate measurements of the Rossiter-McLaughlin(RM) effect, in which RVs are collected continuously while a planet is simultaneously transiting its host star. The RM results are summarized in (Albrecht et al. 2013) showing the stellar spin axis to be well aligned with the orbital axis. Albrecht et al. (2013) find lambda, the angle between the orbital plane of the transiting planet to the stellar rotation axis to be 2 ± 5 degrees. The RVs taken while the planet was transiting were removed for the RV analysis presented here.

The two transiting planets in the system have been confirmed with TTVs, but the upper limits on the planet masses are not meaningful. With RVs, we can show that both transiting planets are definitively low density. For KOI-244.01 we find a mass = $24.6 \pm 6 M_{\oplus}$, with a corresponding density of $0.0 \pm 0.2 \text{ g cm}^{-3}$. for KOI-244.02 we find a planet mass of 9.6 ± 4.2 and a density of $2.5 \pm 1.1 \text{ g cm}^{-3}$. An additional signal in the radial velocities shows a signal of period 123 days corresponding to a mass of $89 \pm 14 M_{\oplus}$. The orbit of the non-transiting planet is slightly eccentric($\text{ecc} = 0.12$). We have strongly constrained the masses and densities of the transiting planets to be low density, requiring them to consist of large amounts of volatiles.

The full set of RVs, minus the RVs used to measure the Rossiter-McLaughlin effect, are listed, along with their R'_{HK} activity values in Table 14.

7.12. KOI-245, Kepler-37

This three planet system whose planets have orbital periods of 13(244.03), 21(244.02), and 40(245.01) days have corresponding planet radii of 0.303, 0.742 and 1.99 R_{\oplus} , respectively. A detailed analysis of the Kepler light curve, blend scenarios, and asteroseismic analysis of this exceptionally bright (KepMag = 9.7) KOI with a sub-Mercury sized planet can be found in Barclay et al. (2013). We summarize the follow-up observations here and place limits on the planet masses determined from the precise RV observations.

Recon spectra from the McDonald 2.7m and the Tillinghast 1.5m were taken in March and April 2010, respectively. These spectra confirmed the stellar parameters from the KIC, and showed the $v \sin i$ is less than 2.0km/s. SME analysis taken from a Keck-HIRES spectrum also agreed with the KIC parameters, and the final stellar parameters were determined via asteroseismology, with SME T_{eff} and $\log g$ used as inputs. This KOI is the most dense star yet to reveal asteroseismic oscillations, made possible largely by its brightness, and the final stellar parameters are $T_{\text{eff}} = 5417 \pm 75\text{K}$, $\log g = 4.57 \pm 0.05$, and $[\text{Fe}/\text{H}] = -0.32$.

Speckle imaging was acquired at the WIYN telescope and also at the Gemini Telescope. Adaptive optics imaging was taken with ARIES and all three imaging techniques found no stellar companions. Extensive AO observations were also taken with the updated AO system on Mt. Palomar in the K band (actually br-gamma filter). A more thorough analysis that given here is found in (Barclay et al. 2013) where the probability of background stars falling, undetected, into the Kepler aper-

ture, is discussed. We present a seeing limited image of the field of view in Figure 34a and magnitude limiting plots from the high resolution imaging in Figure 34b.

– The precise RVs from Keck-HIRES are unable to determine the planet masses, because they are below the current detection limits. We constrain the mass of the 40, 21, and 13 day planets to be less than $1.3 \pm 1.2, 4.2 \pm 2.7$, and $1.3 \pm 1.1 M_{\oplus}$. The mass for the 40d planet corresponds to a physically meaningful density of $1.0 \pm 0.9 \text{ g cm}^{-3}$, meaning the one sigma upper limit on density is 1.9 g cm^{-3} . The 21 and 13 day planets have unphysical densities. The 862 day baseline for the RV measurements finds no significant periods above the noise, indicating no non-transiting planets are detected.

The full set of RVs are listed, along with their R'_{HK} activity values in Table 15.

7.13. KOI-246, Kepler-68

This three planet system has two transiting planets with orbital periods of 5.4 and 9.6 days and planet radii equal to 2.3 and $0.95 R_{\oplus}$. The non-transiting planet has an orbital period of 579 ± 17 days and mass of $283 \pm 11 M_{\oplus}$. The non-transiting planet orbital parameters are refined over Gilliland et al. (2013) with one additional RV taken in 2013. For a detailed summary of the light curve analysis, asteroseismic analysis, RV analysis, and discussion of false positive scenarios with BLENDER, see Gilliland et al. (2013) Recon spectra were taken at the McDonald 2.7m on 25th March 2010 and 28th March 2010. A spectrum was acquired at Tillinghast 1.5m on 25th March 2010. The near solar values of temperature, $\log g$ and $v \sin i$ listed in the KIC were confirmed by these recon spectra. SME combined with asteroseismology analysis was also used to confirm the near solar values of stellar mass and stellar radius. The final stellar parameters are $T_{\text{eff}} = 5793 \pm 100$, $\log g = 4.28 \pm 0.02$, and $[\text{Fe}/\text{H}] = 0.12 \pm 0.04$.

Speckle imaging at WIYN taken in June 2010 and adaptive optics imaging taken at ARIES, taken in summer 2010 found no companion stars that could cause confusion in the light curve analysis. Figure 35a shows a seeing limited image of the field of view of the HIRES guide camera. Figure 35b shows the limiting magnitudes achieved with each high resolution imaging method.

The precise RVs collected from 2009 to 2013(Figure 35c) constrain the density of the inner most transiting planet quite well, and provide upper limits to the second transiting planet. The strongest periodic signal in the RVs is caused by a non-transiting planet in 1.6 year orbit, with a minimum mass($M \sin i$) of $0.89 \pm 0.03 M_{\text{JUP}}$. During publication of the KOI-246/Kepler-68 results, the period of the non-transiting planet had an alias, as noted by the referee. The single additional RV made in 2013 has shown the true period to be that quoted here and in the Gilliland et al. (2013) results, not the alias. The inner planet has a mass of $7.9 \pm 2.4 M_{\oplus}$ and a density of $3.0 \pm 0.9 \text{ g cm}^{-3}$, placing this KOI in a density region that is sparsely populated. Lopez et al. (2012) lists this star as having a minimum mass of $6.5 M_{\oplus}$ and minimum density of 2.2 g cm^{-3} , values consistent with those found in this work. The full set of RVs are listed, along with their R'_{HK} activity values in Table 16.

7.14. KOI-261

The single planet in this system has a period of 16.2 days and a radius equal to $2.7 R_{\oplus}$. Three recon spectra were taken at the McDonald 2.7m and FLOW in March and April of 2010. Stellar parameters determined from these spectra with SPC agreed in T_{eff} , but the $\log g$ value was off by 0.4 dex from the KIC value. When the $\log g$ was confirmed with SME analysis done with a Keck-HIRES template spectrum, Yonsei-Yale isochrones were used to adjust the stellar radius from its KIC value of 1.9 to $1.0 R_{\odot}$. The planet radius decreased from 6.2 to $2.7 R_{\oplus}$. Further evidence that the stellar radius is near solar, and not near $1.9 R_{\odot}$ is the non-detection of stellar oscillations in the asteroseismic analysis. A typical $1.9 R_{\odot}$ star would have a detectable asteroseismic signal, which was searched for and not detected. The final stellar parameters are $T_{\text{eff}} = 5690 \pm 43$, $\log g = 4.42 \pm 0.08$, and $[\text{Fe}/\text{H}] = 0.04 \pm 0.04$.

High resolution imaging with the WIYN speckle camera in September 2010 detected no stellar companions, but ARIES observations in summer 2010 detected one nearby companion. Near infrared images show a companion $5.4''$ from the primary at a PA=65.2 and delta magnitude of 7.1 in J-band, and 6.8 in Ks band. The estimated Kepler magnitude of the companion is 18.1. Figure 36a shows a seeing limited image of the field of view of the HIRES guide camera. Figure 36b shows the limiting magnitudes achieved with each high resolution imaging method.

– Precise RV follow-up was initiated in July 2010 and 25 RVs have been acquired for a time baseline of 772 days(Figure 36c). The RV detection for this KOI is not significant, and we constrain the K-amplitude to be less than 2.0 m s^{-1} . The mass limit, however, is significant, in that we can constrain the mass to less than $10.6 M_{\oplus}$ and 2.9 g cm^{-3} at the one sigma level. Such a low density requires some contribution from low density materials such as water, hydrogen or helium, contributing to the planet mass - radius diagram. The RVs show signs of possible non-transiting planet with a poorly defined orbital period. One possible period of the non-transiting planet is 8 days, but at low confidence To find a non-transiting planet interior to a transiting planet would be remarkable, and requires additional data in order to be confirmed. With only 25 RVs, the likelihood that the 8d period is an alias of a true period is quite high, and we withhold announcement of a non-transiting planet until the orbital period can be confirmed.

This one planet system is another good point on the M-R diagram. The mass is 7 ± 4 earth masses with a radius of $2.65 R_{\oplus}$. The density is $2.1 \pm 1.2 \text{ g cm}^{-3}$, making the planet definitively gaseous.

The full set of RVs are listed, along with their R'_{HK} activity values in Table 17.

7.15. KOI-283

The two planets in this system have orbital periods of 16.0 and 25.5 days with radii 2.4 and $0.8 R_{\oplus}$. The two recon spectra taken McDonald 2.7m and FLOW are good agreement with each other and with the final T_{eff} , and $\log g$. The KIC T_{eff} agrees with the follow-up observations, but the $\log g$ found with spectroscopy is 0.5 dex larger than the KIC value, resulting in a decrease in stellar radius of 40%. The final T_{eff} and $\log g$ were determined from SME and the stellar mass and radius

were determined using the SME results combined with Yonsei-Yale stellar isochrones, leading to $T_{\text{eff}} = 5685 \pm 44\text{K}$, $\log g = 4.42 \pm 0.08$ and $[\text{Fe}/\text{H}] = 0.12 \pm 0.04$.

Speckle imaging from the WIYN found no stellar companions and the lone stellar companion detected with adaptive optics imaging from Mt. Palomar is six arc seconds away and 8 magnitudes fainter in J-band and Ks-band. Such a companion does not affect the transit signal, as a transit on such a companion would be easily detected with centroid motion analysis of the Kepler photometry. Figure 37a shows a seeing limited image of the field of view of the HIRES guide camera. Figure 37b shows the limiting magnitudes achieved with each high resolution imaging method.

The RV signal spanning 741 days (Figure 37c) for KOI-283 provides both conclusions and puzzles. The conclusions consist of a marginal detection of the 16d planet at $16.1 \pm 3.5 M_{\oplus}$, with a density of $6.0 \pm 2. g \text{ cm}^{-3}$. This planet has a density similar to Earth, although not with high confidence. We find similar results when we fit this planet by itself, or if we fit the second planet simultaneously. However, when we fit both planets together, we find a moderate detection of the second planet, corresponding to a planet mass of $17.8 \pm 5 M_{\oplus}$. With a planet this massive, and a radius of only $0.8 R_{\oplus}$, the density is $157 g \text{ cm}^{-3}$, a non-physical value. No known material has a density this high. Several explanations may explain this result. 1) The 25 day planet is aliasing with the 16d planet and the resulting RV signals cannot be pulled apart. 2) A bound binary star system with the secondary star of lower mass, orbits the primary at 20-25AU. Such a companion would be undetectable with AO(too near the primary), speckle(too faint), or as secondary lines in the HIRES spectrum(inadequate RV difference to distinguish from the primary lines). In this scenario both the transit light curve and Doppler shift come from the planet orbiting the secondary star, with both observables being diluted by the light of the primary star. Such a planet would be much larger than $0.8 R_{\oplus}$. 3) The transit durations suggest that the inner planet orbits the secondary star while the outer planet orbits the primary star.[unfinished].

The full set of RVs are listed, along with their R'_{HK} activity values in Table 18.

7.16. KOI-292

The single transiting planet in this system has 2.6d orbital period, and radius of $1.5 R_{\oplus}$. Follow-up on this KOI began with Recon spectra being taken in March and April 2010 at the McDonald 2.7m telescope. SPC analysis found this star to be a slowly rotating main sequence star, an ideal target for Keck-HIRES. The T_{eff} found with recon was 400K hotter than the final T_{eff} determined by SME combined with Yonsei-Yale isochrones. The final stellar radius is 30% smaller than that found by the KIC. The final stellar parameters are $T_{\text{eff}} = 5779 \pm 44\text{K}$, $\log g = 4.42 \pm 0.08$, and $[\text{Fe}/\text{H}] = -0.20 \pm 0.04$, sub-solar metallicity.

Adaptive optics imaging at Palomar shows a companion star with a separation of $0.36''$ from the primary at a PA = 121.8. The companion was measured to be 2.7 and 2.8 magnitudes fainter than the primary, in the J-band and Ks-band respectively. Speckle imaging revealed no

companions down to a delta magnitude of 3 and 4 in the R-band and V-band, respectively. The non-detection with speckle is likely due to the companion being brighter in the infrared than in the visible, relative to the primary. The companion is listed in Adams et al. (2012), and makes this a less than ideal target for precise RVs due to the contamination of the companion in the spectrum of the primary. Figure 38a shows a seeing limited image of the field of view of the HIRES guide camera. Figure 38b shows the limiting magnitudes achieved with each high resolution imaging method.

This system has an RV trend of 5m/s/year over three years, and after 789 days of RV baseline(Figure 38c), it shows no deviations from a straight line. The companion causing the linear trend likely has a an orbital period longer than the baseline, making the lower limit of the orbital period of the companion 3 years. The RVs are potentially due to the companion found with the AO imaging[Is this true??] Aside from the linear trend, the RVs are consistent with, but not strongly correlated with the transiting planet. We place one-sigma upper limits on the mass of the transiting planet to be $3.5 \pm 1.9 M_{\oplus}$, corresponding to a density of $5.4 \pm 3 g \text{ cm}^{-3}$. The two sigma lower limits are consistent with zero mass, meaning a non-detection at the two-sigma level. The phase folded RV curves are shown in Figure 38d.

The full set of RVs are listed, along with their R'_{HK} activity values in Table 18.

7.17. KOI-299

The transiting planet in two planet system has an orbital period of 1.5 days and a radius of $2.0 R_{\oplus}$. We also detect a non-transiting planet with an orbital period of 22.09 ± 0.04 days and $M \sin i = 32.5 \pm 5 M_{\oplus}$. Before precise RVs were acquired, recon spectra were taken with the McDonald 2.7m in March 2010 and the Tillinghast 1.5m in June 2010. The stellar temperatures found by using SPC to analyze the recon spectra were in agreement with KIC values, but the difference in $\log g$ values resulted in a 40% decrease of the stellar radius, compared to the final stellar radius value. The final stellar parameters of $T_{\text{eff}} = 5589 \pm 43\text{K}$, $\log g = 4.34 \pm 0.10$ and $[\text{Fe}/\text{H}] = 0.18 \pm 0.04$ were found using a Keck-HIRES spectrum, with SME analysis and matching of spectral parameters to Yonsei-Yale isochrones.

Speckle imaging at the WIYN conducted in September 2010 detected no companions within its limits, but no adaptive optics images were taken to rule out even fainter companions. The Keck guider image (Figure 39a) shows no companions from $1.0''$ to $6''$ from the primary, down to a delta magnitude of seven. The exclusion limits on companion stars is shown in 39b. The Keck guider image was not used in this exclusion plot.

The radial velocities, which cover a basline of show a marginal detection of the transiting planet (39c), and a much stronger detection of a non-transiting planet with a period of 22.1 days. We find the mass of the transiting planet to be $3.5 \pm 1.6 M_{\oplus}$ with a density of $2.2 \pm 1.2 g \text{ cm}^{-3}$. Despite the weak detection of the transiting planet, the limits placed on the mass, and hence density of the planet show that the planet must have a large percentage of light weight, volatile material. The one sigma upper limit on the mass is $4.0 M_{\oplus}$, corresponding to limit of $3.3 g \text{ cm}^{-3}$ on the density. Having 21 RVs with

a baseline of 804 days constrains the period of the non-transiting planet quite well, but more measurements are needed to more precisely determine its eccentricity.

The full set of RVs are listed, along with their R'_{HK} activity values in Table 20.

7.18. KOI-305

The single transiting planet in this system with an orbital period of 4.6 days and a radius of $1.5 R_{\oplus}$ shows a strong correlation with precise RVs from Keck-HIRES. Recon spectroscopy of target was initiated in March of 2010 at the McDonald 2.7m. In May 2010, a second recon spectrum was taken at the Tillinghast 1.5m. Both spectra were used to determine T_{eff} and $\log g$. The results from each spectra were consistent with each other, and were in agreement with the KIC values in T_{eff} , and are in marginal agreement with the KIC in $\log g$. No large RV variation was seen, within errors, and the low rotational velocity of the star lead to collection of precise RVs. Once a Keck-HIRES template was taken, SME was used with Yonsei-Yale isochrones to determine the final stellar parameters of $T_{\text{eff}} = 4782 \pm 115\text{K}$, $\log g = 4.61 \pm 0.05$, and $[\text{Fe}/\text{H}] = 0.18 \pm 0.04$. The final stellar radius is 30% smaller than the KIC values.

Speckle imaging taken at the WIYN telescope found no companions within its limits and no further imaging is available. When observing with Keck-HIRES, a guider image was taken. No companions were detected from $2.0''$ out to $4.0''$ within seven magnitudes fainter than the primary, in the R-band. Figure 40a shows a seeing limited image of the field of view of the HIRES guide camera. Figure 40b shows the limiting magnitudes achieved with Speckle imaging.

The RV basline of 791 days(Figure 40c) shows no linear trends or periodicities aside from the transiting planet. This single, $1.5R_{\oplus}$ planet has a mass determined from RVs of $6.2 \pm 1.3M_{\oplus}$. The planet density is $10.8 \pm 2.8 \text{ g cm}^{-3}$, suggesting the planet is similar in density to Kepler-10b, but at a lower significance. The phase folded RV curve is shown in Figure 40d. [add more discussion]

The full set of RVs are listed, along with their R'_{HK} activity values in Table 21.

7.19. KOI-321

The two transiting planets in this three planet system have periods of 2.4 and 4.6 days with radii equal to 1.4 and $0.8 R_{\oplus}$, respectively. A third, non-transiting planet has a period of $28.1 \pm 0.07\text{days}$ and a mass of $21.8 \pm 4.4 M_{\oplus}$. Before the non-transiting planet was detected, and the inner planet's mass was measured, recon spectroscopy was taken at the Tillinghast 1.5m, where the temperature was confirmed to be near the KIC value. The slow rotation of the star was identified and the RV variation was seen to be below 500m/s. The $\log g$ value found by recon, and later refined with SME and asteroseismology analysis, to be larger than the KIC by a significant amount. The discrepancy in $\log g$ from the KIC to the final value resulted in an increase in the stellar, and planet radii, of 30%. The final stellar parameters, although not published in (Huber et al. 2013) were found using similar methods. The SME served as the starting

point of the asteroseismology analysis that lead to $T_{\text{eff}} = 5538 \pm 44\text{K}$, 4.41 ± 0.02 , and $[\text{Fe}/\text{H}] = 0.18 \pm 0.04$.

Imaging including Speckle imaging with WIYN in September 2010 and adaptive optics imaging taken with the Lick 3m in September 2011, found no companions nearby that are contaminating the light curve. Figure 41a shows a seeing limited image of the field of view of the HIRES guide camera. Figure 41b shows the limiting magnitudes achieved with Speckle imaging and the Lick 3m.

Precise RVs taken over 800 days, beginning in July 2010 show two strong signals(Figure 41c). The first has the period of the inner transiting planet. We find a the $1.4 R_{\oplus}$ planet to have a mass of $6.4 \pm 1.4 M_{\oplus}$ with a corresponding density of $11.8 \pm 2.7 \text{ g cm}^{-3}$. Such high density requires a large amount of rocky material. The outer transiting planet is shows no signal in the RVs, so we report an upper limit of no more than $5 M_{\oplus}$, at the one sigma level . The second signal seen in the RVs has a period of 28 days and corresponds to a non-transiting planet with a minimum mass, $M \sin i = 21.4 \pm 4 M_{\oplus}$. [details on eccentricity are needed]

The full set of RVs are listed, along with their R'_{HK} activity values in Table 22.

7.20. KOI-1442

With a period of 0.67 days and a radius of $1.1 R_{\oplus}$, KOI-1442 has similar orbital period to the planet Kepler-10b. However, the RVs provide only upper limits to the transiting planet's mass, and a partial orbit of a non-transiting planet. Follow-up observing began in March 2011 when recon spectra were collected at the McDonald 2.7m. SPC analysis of the spectrum confirmed the T_{eff} and $\log g$ from the KIC. After acquisition of the Keck-HIRES template spectrum, SME analysis was run, and the final stellar parameters were calculated by combining the SME result with Yonsei-Yale isochrones. The final stellar parameters are $T_{\text{eff}} = 5476 \pm 46\text{K}$, $\log g = 4.43 \pm 0.06$ and $[\text{Fe}/\text{H}] = 0.04 \pm 0.003$.

Speckle observing at WIYN in September 2010 did not identify any companion stars within the limits. There is one companion identified in UKIRT images that is outside of the field of view of speckle. The companion star is $2.1''$ to the NE of the primary and roughly 5.3 magnitudes fainter in the Kepler Bandpass. Centroid analysis of the pixel level data constrains the centroid of the planet transit to be within $0.44''$ of the primary, ruling out the possibility that the transits are actually occurring on a nearby star. Figure 42a shows a seeing limited image of the field of view of the HIRES guide camera. Figure 42b shows the limiting magnitudes achieved with speckle imaging.

The most prominent signal in the RVs is a decrease of 200m/s over the 475d baseline(Figure 42c). A slight curvature in the RVs is indicative of a massive body in a orbit of roughly four years, with a mass, $M \sin i 5 M_{\text{JUP}}$. With only one quarter of this potential four year orbit observed, the outer body remains poorly constrained in both orbital period and $M \sin i$. The transiting planet and the non-transiting planet are fit simultaneously, and the poor constraints on the outer body leave the RV signature of the inner planet undetectable. The one sigma upper limit on the mass of the transiting planet is $1.7 M_{\oplus}$. The phase folded RV curves are shown in Figure

42d.

The full set of RVs are listed, along with their R'_{HK} activity values in Table 23.

[Why are cf3.mdchi values so high for this one? median value = 1.27, Is stellar companion in the slit?]

7.21. KOI-1612

The single planet in this system has a period of 2.5d and a radius of $0.82 R_{\oplus}$. This F-type star was first followed up from the ground at the Tillinghast 1.5m where two spectra were taken. SPC determined the stellar parameters to be consistent with the KIC and showed no dramatic RV variation. Before the asteroseismology analysis was conducted in Huber et al. (2013), Bruntt et al. (2012) identified this bright star as having detectable asteroseismic oscillations. We use the SME-asteroseismology values in this work. The $T_{\text{eff}} = 6104 \pm 74$, $\log g = 4.29 \pm 0.03$, and $[\text{Fe}/\text{H}] = -0.20 \pm 0.10$.

Speckle imaging taken at the WIYN in July 2011 found no companion stars within the limits. No adaptive optics imaging was acquired for this star[Double check data from David Ciardi]. Figure 43a shows a seeing limited image of the field of view of the HIRES guide camera. Figure 43b [no guider image yet] shows the limiting magnitudes achieved with speckle imaging.

The first precise RVs were obtained shortly after the recon spectra were taken in May 2011, resulting in an RV baseline of 477 days(Figure 43d). The brightness of the star allowed us to obtain high signal to noise observations($S/N = 200$), similar to those obtained for the standard CPS planet search stars. While we have not directly detected the planet, we place a one sigma upper limit on the mass of the planet equal to $4.3M_{\oplus}$, but the limit on density is too uncertain to provide insight into composition. There are no radial velocity signatures or periodicities that suggest the presence of a non-transiting planet in the system that would predict an RV amplitude greater than 4 m s^{-1} . A longer time baseline of observations will further constrain non-transiting planets. The posterior distribution of expected mass values is well behaved, and peaks near zero, as expected for RVs with well understood, photon limited uncertainties that provide only upper limits on the planet mass. The phase folded RV curve is shown in Figure 43d.

The full set of RVs are plotted in Figure ?? and listed, along with their R'_{HK} activity values, in Table 24.

7.22. KOI-1925

This KOI with a radius of $1.2 R_{\oplus}$ and period of 69 days was first followed up in the 2012 observing season. KOI-1925 is one of Kepler's brightest KOIs(Kepmag = 9.44) with a near earth sized planet. It has well determined parameters from asteroseismology(Bruntt et al. 2012; Huber et al. 2013). This analysis determined that the final value of $\log g$ differed from the KIC value and therefore the stellar radius was adjusted to only 40% of the KIC value. Recon Spectra from the Tillinghast 1.5m were taken and broadly confirmed the analysis of asteroseismology. The final stellar parameters are $T_{\text{eff}} = 5460 \pm 75\text{K}$, $\log g = 4.50 \pm 0.03$ and $[\text{Fe}/\text{H}] = 0.08 \pm 0.10$.

No high resolution of this KOI is available due to its discovery late in the 2012 observing season. [change if David Ciardi is able analyze the data.]

Keck-HIRES RVs taken over 174 days in summer 2012(Figure 44c) all have high signal to noise ratios of 200. This SNR is similar to the typical planet search stars, acquired in roughly ten minute exposures. The planet's expected radial velocity amplitude, assuming some mass-radius relationship, is below our detection threshold. None-the-less, we limit the planet's mass to be less than $8.5M_{\oplus}$ at the one sigma level. Such limits are insufficient to make conclusions about planet composition. With 25 RVs, showing an RMS of only 3.2 m s^{-1} we place upper limits on the mass of the transiting planet, and rule any massive ($m_{\text{simi}} > 30M_{\oplus}$, expected K amplitude = 4.5 m s^{-1}) planets in orbits interior to the transiting planet.

The full set of RVs are plotted in Figure ?? and listed, along with their R'_{HK} activity values in Table 25.

8. DISCUSSION

The mass and radii of the planet studied here were selected for study based on their measured radii alone. The RV measured were continued regardless of the RV signal that emerged. To be sure, the KOIs with clear RV detections attracted more RV measurements to constrain further the measured mass. But the selection of planets, and their appearance among the 22 KOIs here, was made without regard to their mass. Thus the resulting planet masses within a certain range of a priori planet radii represent those of the population of planets in the *Kepler* field. Figure 45 shows a distribution of planet radii in our sample.

As the KOI selection was unbiased with regard to planet mass (we had no prior indicators of mass), this offers an opportunity to measure the average planet mass at a given planet radius, the distribution of planet masses, and the relationship between planet radius and mass with minimal concern about a bias in mass. Figure 46 shows the distribution of planet masses found here. The masses span the range from consistent with zero to M_2 . Figure 47 shows the distribution of planet densities.

We specifically allowed our MCMC analysis to include negative planet masses. Such unphysical masses are a normal product of fluctuations in the RV measurements and their uncertainties. As the each planet's orbital ephemeris was known from the transit light curve, the RVs are expected to be higher than average during specific orbital phases and lower than average during the remaining half. The transit ephemeris leaves little flexibility in expected RV variation as a function of phase, except for the unknown orbital eccentricities, which are probably typically less than 0.3 based on the small exoplanets for which eccentricities have been measured. Thus the ephemeris provides a clear prediction about when in phase the RVs are expected to be higher and lower than average. Any agreement between observed and predicted RV variation leads to a measurement of a positive planet mass.

However, the RVs have uncertainties of several m s^{-1} . If the true RV semi-amplitude, K , of the RVs is smaller than several m s^{-1} (due to small planet mass), fluctuations may result in the measured RVs being high when predicted to be low and vice-versa, simply due to errors. Indeed, for the low density planets, such non-detections of planet mass are expected, in which case RV errors will yield anti-correlated RV with phase and hence apparent

negative value of RV semi-amplitude, K , which translates to a negative planet mass. Statistically, as planet masses are certainly positive, even the RV non-detections will systematically yield slightly positive values of K and mass, if only at levels barely significant given the RV noise. Thus, the observed distribution of implied planet masses from RVs, for a given planet radius, are expected to span a range in general from positive values to negative values, the latter stemming from RV noise. The average planet mass and its distribution (including negative values) is needed to capture the true underlying distribution and average planet mass for a given planet radius. Thus, we report in Table 2 the planet mass corresponding to the peak in the MCMC posterior distribution and the values of mass corresponding to 34% of the integrated area of the distribution on either side representing the "1-sigma" departures from the peak value of planet mass.

Several of the planets studied here have densities above 5.5 g cm^{-3} , greater than that of Earth, making them plausibly rocky. Detailed models of planet interiors, including possible chemical compositions, stratified differentiation, and equations of state are needed to predict the plausible bulk densities associated with planets with a given certain mass. Recent work on the interiors of rocky planets have been carried out by Rogers & Seager (2010a,b); Rogers et al. (2011); Zeng & Sasselov (2013); ?. Several of the planets studied here have densities above 8 g cm^{-3} , suggesting the possibility of chemical compositions enriched in iron and nickel relative to that of the interior of the Earth. Indeed exoplanets such as CoRoT 7b and Kepler-10b have densities near 8 g cm^{-3} suggesting the need for such iron/nickel enrichment relative to Earth. Discussions have ensued about whether iron-rich planets might result, a la Mercury, from giant collisions that strip the silicate and volatile envelopes or instead whether such compositional oddities might result from processes intrinsic to planet formation. Recent work by Wurm et al. (2013) provides an interesting mechanism of photoporetic separation of metals from silicates to form iron-rich planets such as Mercury, CoRoT-7B, Kepler-10b, and the densest planets found at the 2-sigma level here including seven planets, KOI-41.02, KOI-82.02, KOI-82.03, KOI-283.01, KOI-283.02, KOI-305.01, and KOI-321.01.

9. SUMMARY

Kepler was competitively selected as the tenth NASA Discovery mission. Funding for this mission is provided by NASA's Science Mission Directorate. Some of the data presented herein were obtained at the W. M. Keck Observatory, which is operated as a scientific partnership among the California Institute of Technology, the University of California, and the National Aeronautics and Space Administration. The Keck Observatory was made possible by the generous financial support of the W. M. Keck Foundation. Some of the asteroseismology analysis was performed by the Stellar Astrophysics Centre which is funded by the Danish National Research Foundation. The research is supported by the ASTERISK project (ASTERoseismic Investigations with SONG and Kepler) funded by the European Research Council (Grant 267864). W. F. Welsh and J. A. Orosz acknowledge support from NASA through the Kepler Participat-

ing Scientist Program and from the NSF via grant AST-1109928. D. Fischer acknowledges support from NASA ADAP12-0172. O. R. Sanchis-Ójeda & J. N. Winn are supported by the Kepler Participating Scientist Program (PSP) through grant NNX12AC76G. E. Ford is partially supported by NASA PSP grants NNX08AR04G & NNX12AF73G. Eric Agol acknowledges NSF Career grant AST-0645416. We would also like to thank the Spitzer staff at IPAC and in particular; Nancy Silbermann for checking and scheduling the Spitzer observations. The Spitzer Space Telescope is operated by the Jet Propulsion Laboratory, California Institute of Technology under a contract with NASA. The authors would like to thank the many people who gave so generously of their time to make this Mission a success. All *Kepler* data products are available to the public at the Mikulski Archive for Space Telescopes

<http://stdatu.stsci.edu/kepler/>

the spectra and their products are made available at the NExSci Exoplanet Archive and its CFOP website:

<http://exoplanetarchive.ipac.caltech.edu/>

We thank the many observers who contributed to the measurements reported here. We gratefully acknowledge the efforts and dedication of the Keck Observatory staff, especially Scott Dahm, Hien Tran, and Grant Hill for support of HIRES and Greg Wirth for support of remote observing.

This work made use of the SIMBAD database (operated at CDS, Strasbourg, France) and NASA's Astrophysics Data System Bibliographic Services. This research has made use of the NASA Exoplanet Archive, which is operated by the California Institute of Technology, under contract with the National Aeronautics and Space Administration under the Exoplanet Exploration Program. Finally, the authors wish to extend special thanks to those of Hawaiian ancestry on whose sacred mountain of Mauna Kea we are privileged to be guests. Without their generous hospitality, the Keck observations presented herein would not have been possible.

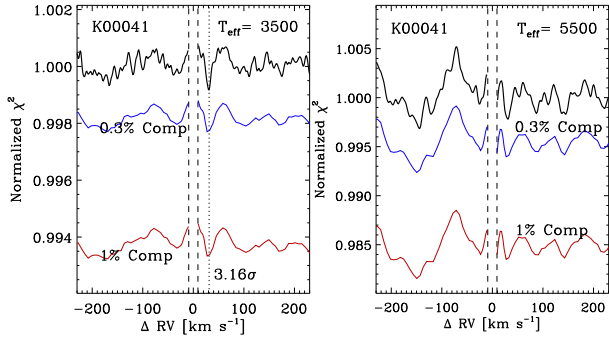


FIG. 1.— Secondary Spectrum Exclusion plot, Version 1, KOI41

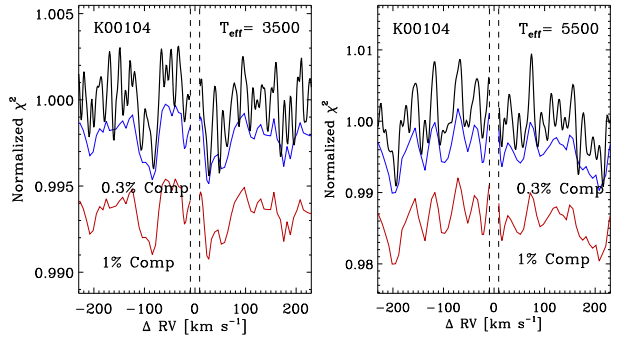


FIG. 4.— Secondary Spectrum Exclusion plot, 104

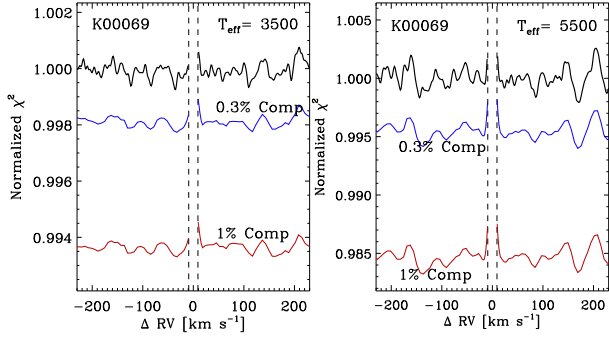


FIG. 2.— Secondary Spectrum Exclusion plot, 69

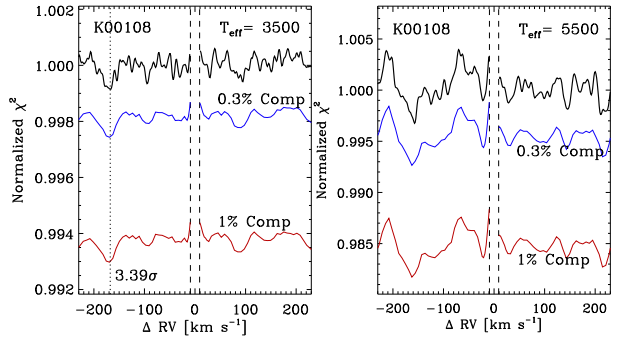


FIG. 5.— Secondary Spectrum Exclusion plot, 108

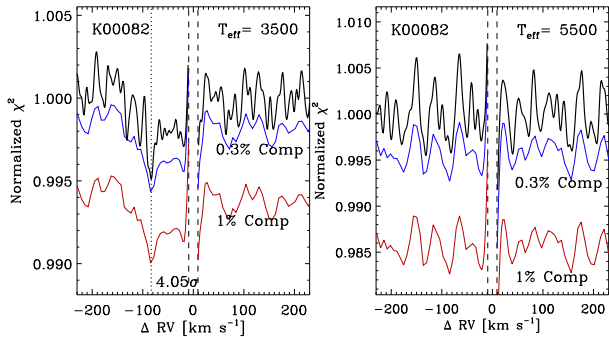


FIG. 3.— Secondary Spectrum Exclusion plot, 82

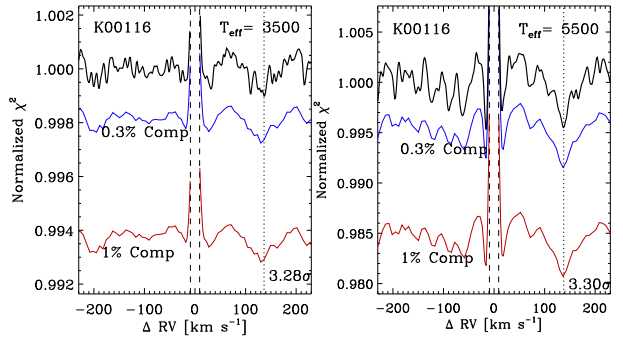


FIG. 6.— Secondary Spectrum Exclusion plot, 116

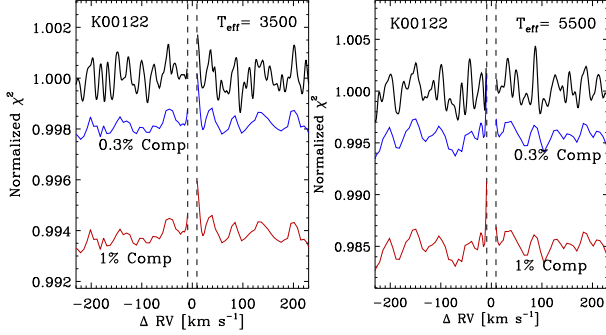


FIG. 7.— Secondary Spectrum Exclusion plot, 122

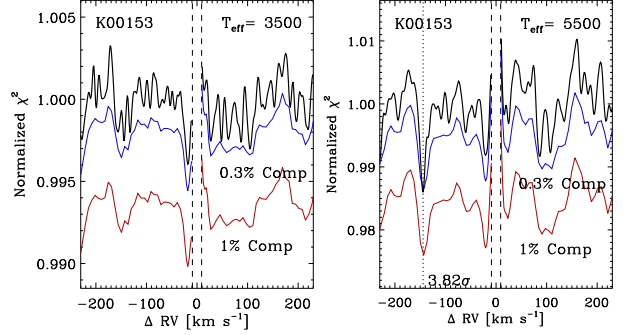


FIG. 10.— Secondary Spectrum Exclusion plot, 153

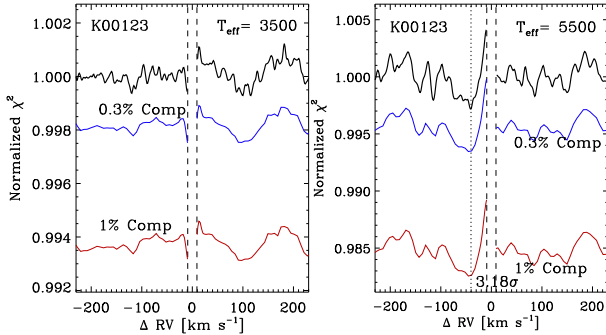


FIG. 8.— Secondary Spectrum Exclusion plot, 123

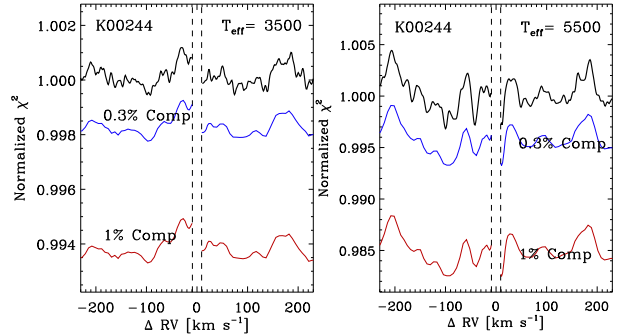


FIG. 11.— Secondary Spectrum Exclusion plot, 244

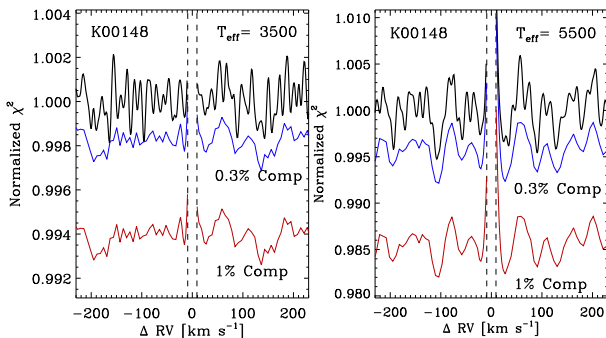


FIG. 9.— Secondary Spectrum Exclusion plot, 148

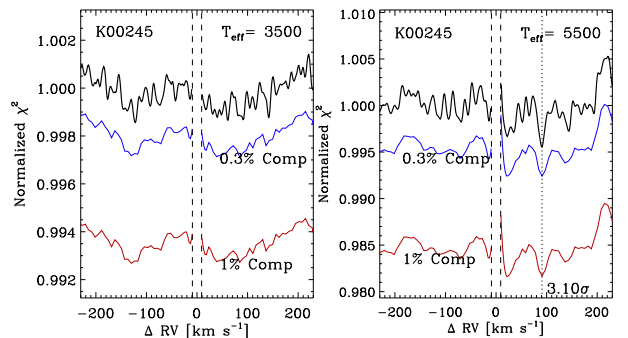


FIG. 12.— Secondary Spectrum Exclusion plot, 245

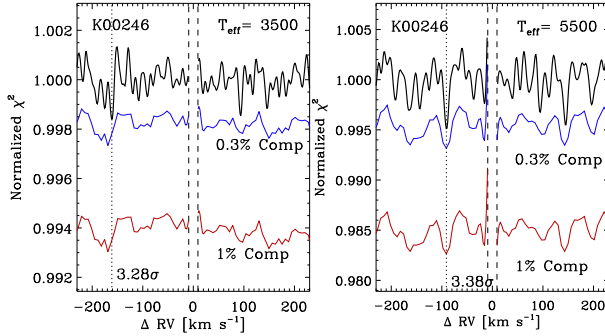


FIG. 13.— Secondary Spectrum Exclusion plot, 246

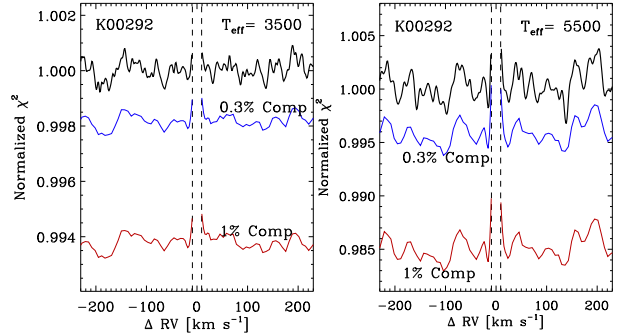


FIG. 16.— Secondary Spectrum Exclusion plot, 292

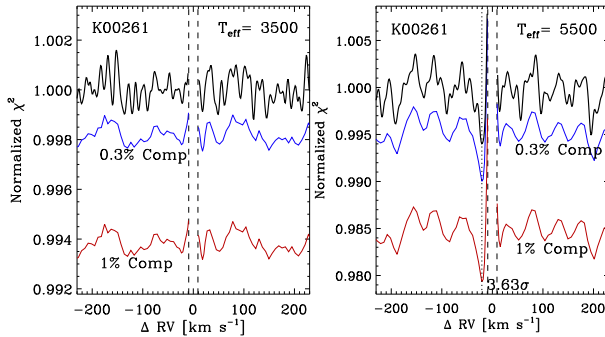


FIG. 14.— Secondary Spectrum Exclusion plot, 261

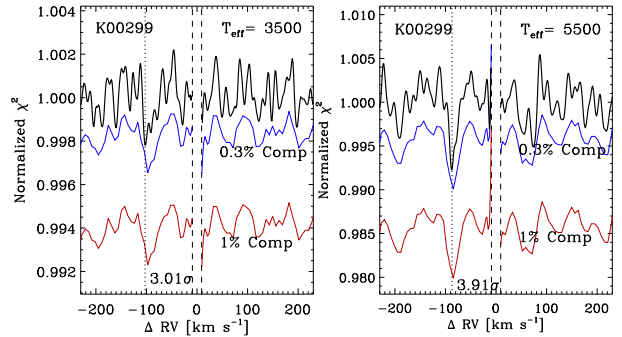


FIG. 17.— Secondary Spectrum Exclusion plot, 299

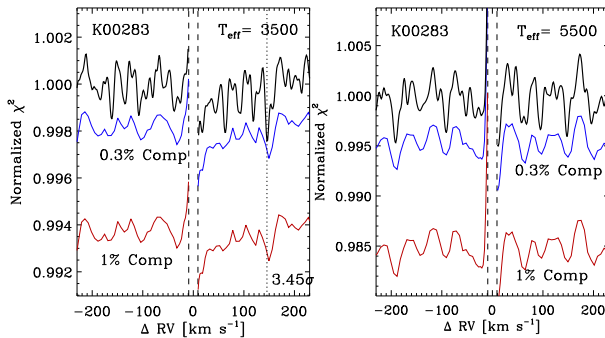


FIG. 15.— Secondary Spectrum Exclusion plot, 283

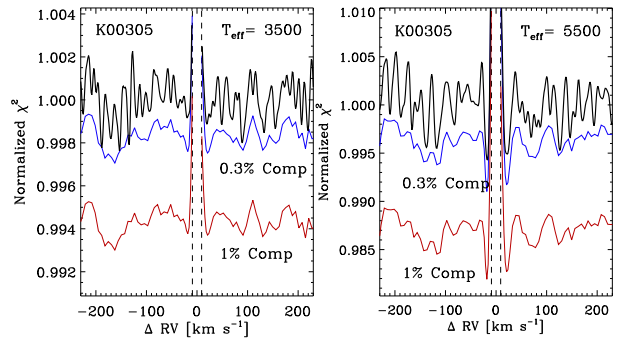


FIG. 18.— Secondary Spectrum Exclusion plot, 305

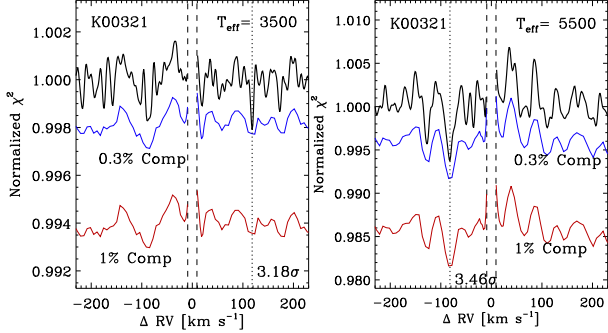


FIG. 19.— Secondary Spectrum Exclusion plot, 321

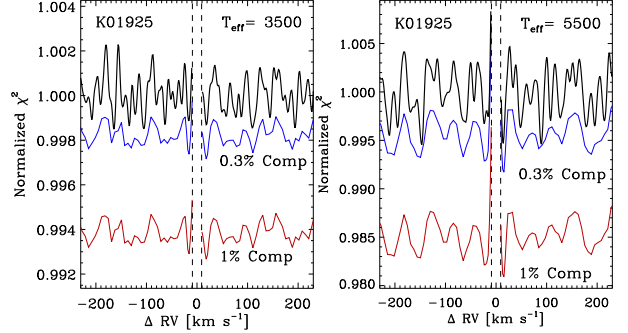


FIG. 22.— Secondary Spectrum Exclusion plot, 1925

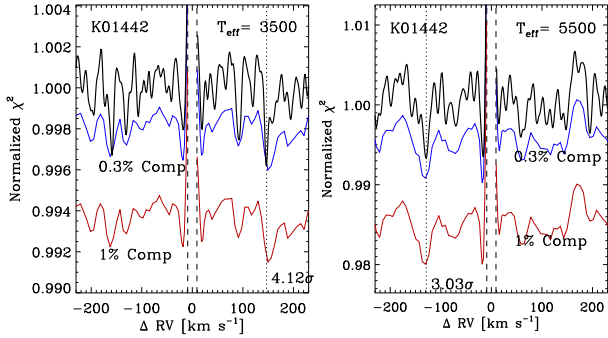


FIG. 20.— Secondary Spectrum Exclusion plot, 1442

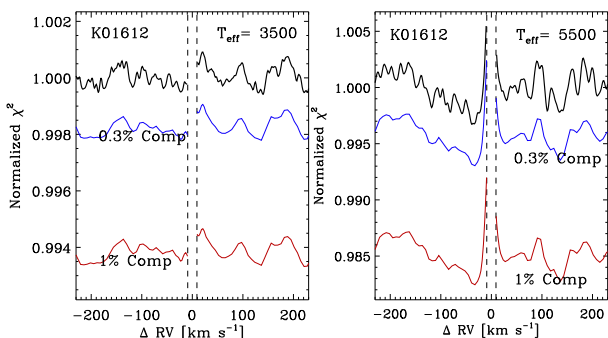


FIG. 21.— Secondary Spectrum Exclusion plot, 1612

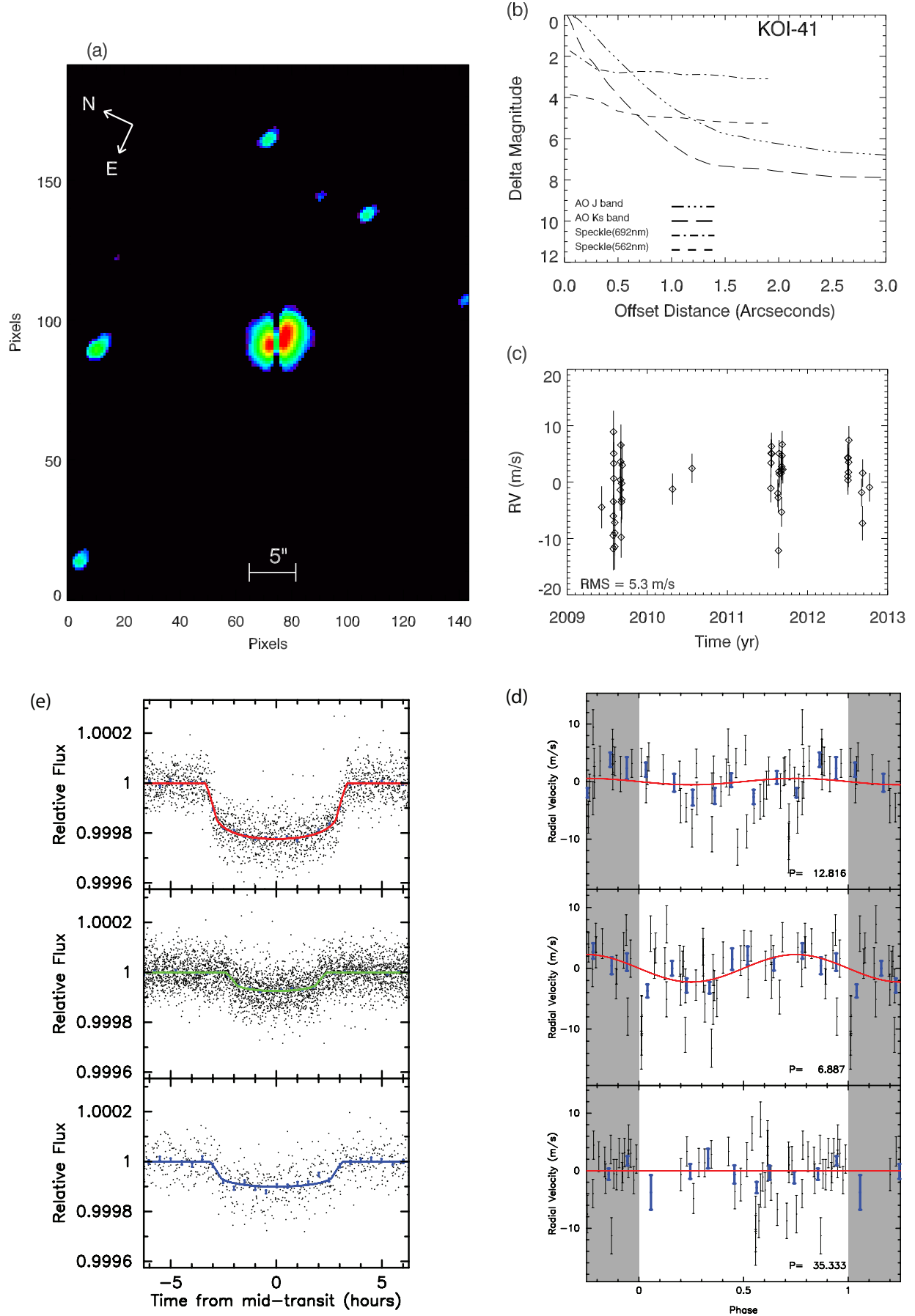


FIG. 23.— a) Keck-HIRES guider image. b) Companion star exclusion plot, c) RV time series, d) Phase folded RV curves for each planet e) Phase folded light curve for the transiting planets.

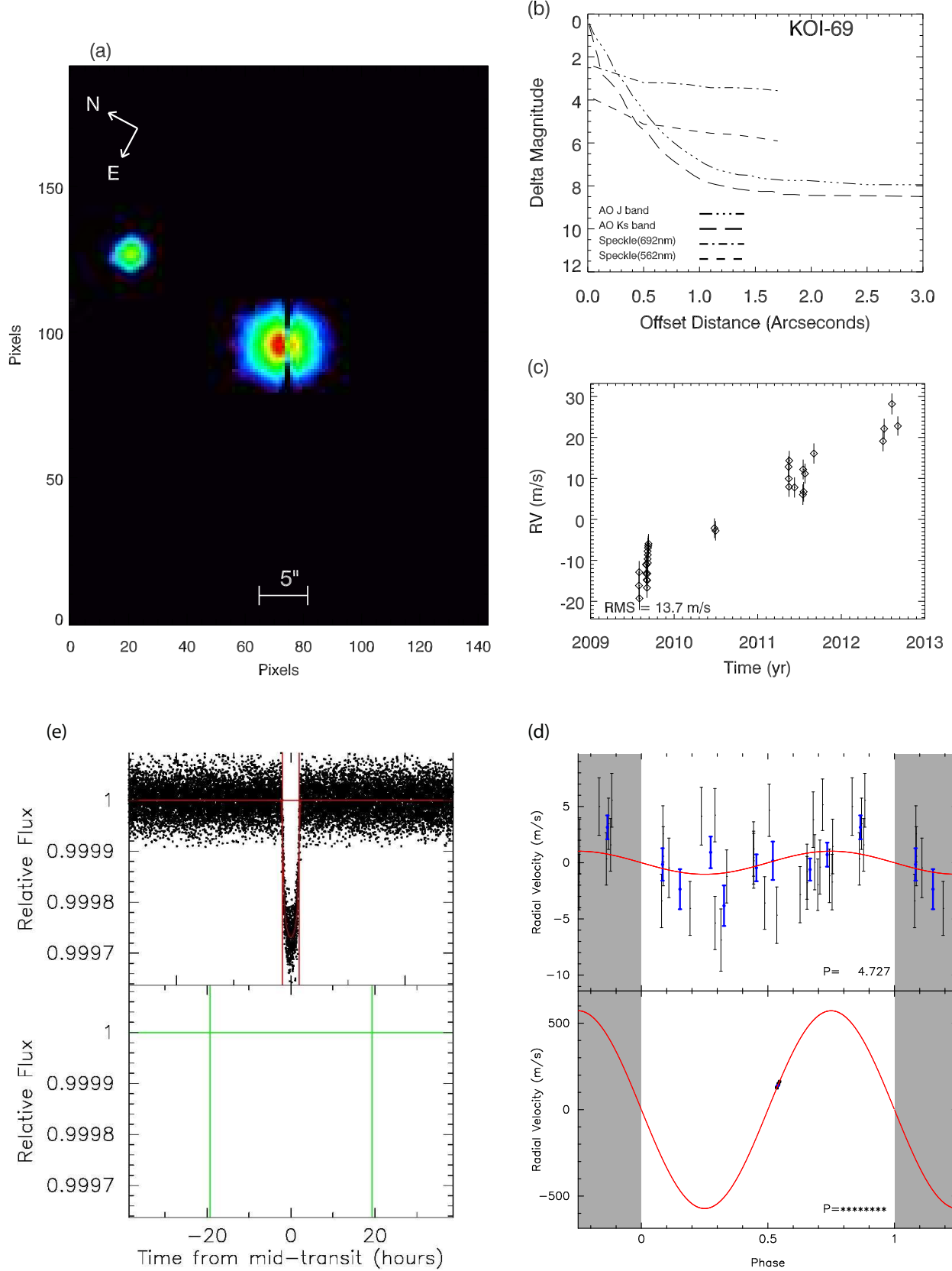


FIG. 24.— a) Keck-HIRES guider image. b) Companion star exclusion plot, c) RV time series, d) Phase folded RV curves for each planet e) Phase folded light curve for the transiting planet, and for non-transiting planets, the light curve phase folded to the non-transiting planet period, showing lack of a transit.

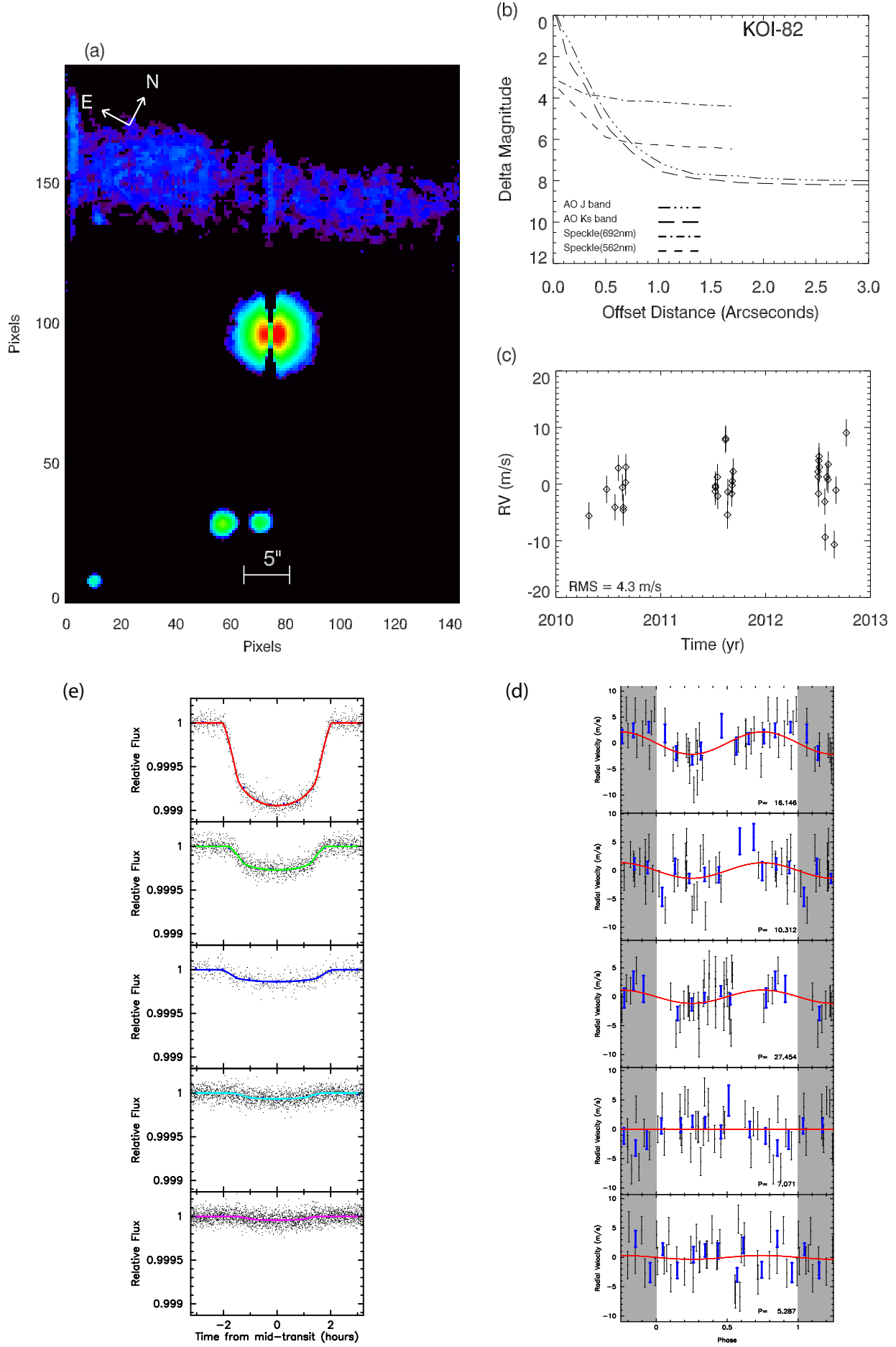


FIG. 25.— a) Keck-HIRES guider image. b) Companion star exclusion plot, c) RV time series, d) Phase folded RV curves for each planet e) Phase folded light curve for the transiting planets.

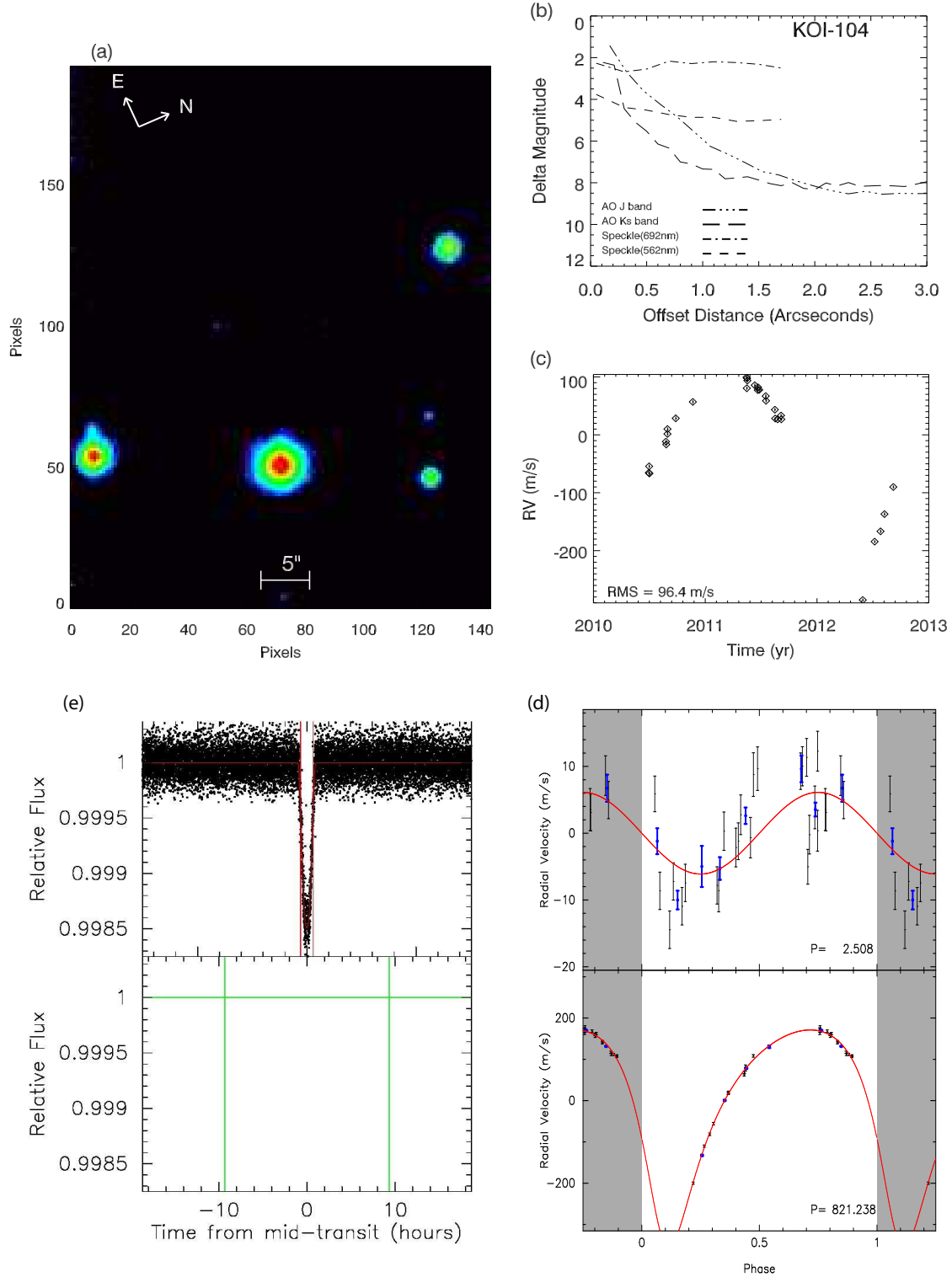


FIG. 26.— a) Keck-HIRES guider image. b) Companion star exclusion plot, c) RV time series, d) Phase folded RV curves for each planet e) Phase folded light curve for the transiting planet, and for non-transiting planets, the light curve phase folded to the non-transiting planet period, showing lack of a transit.

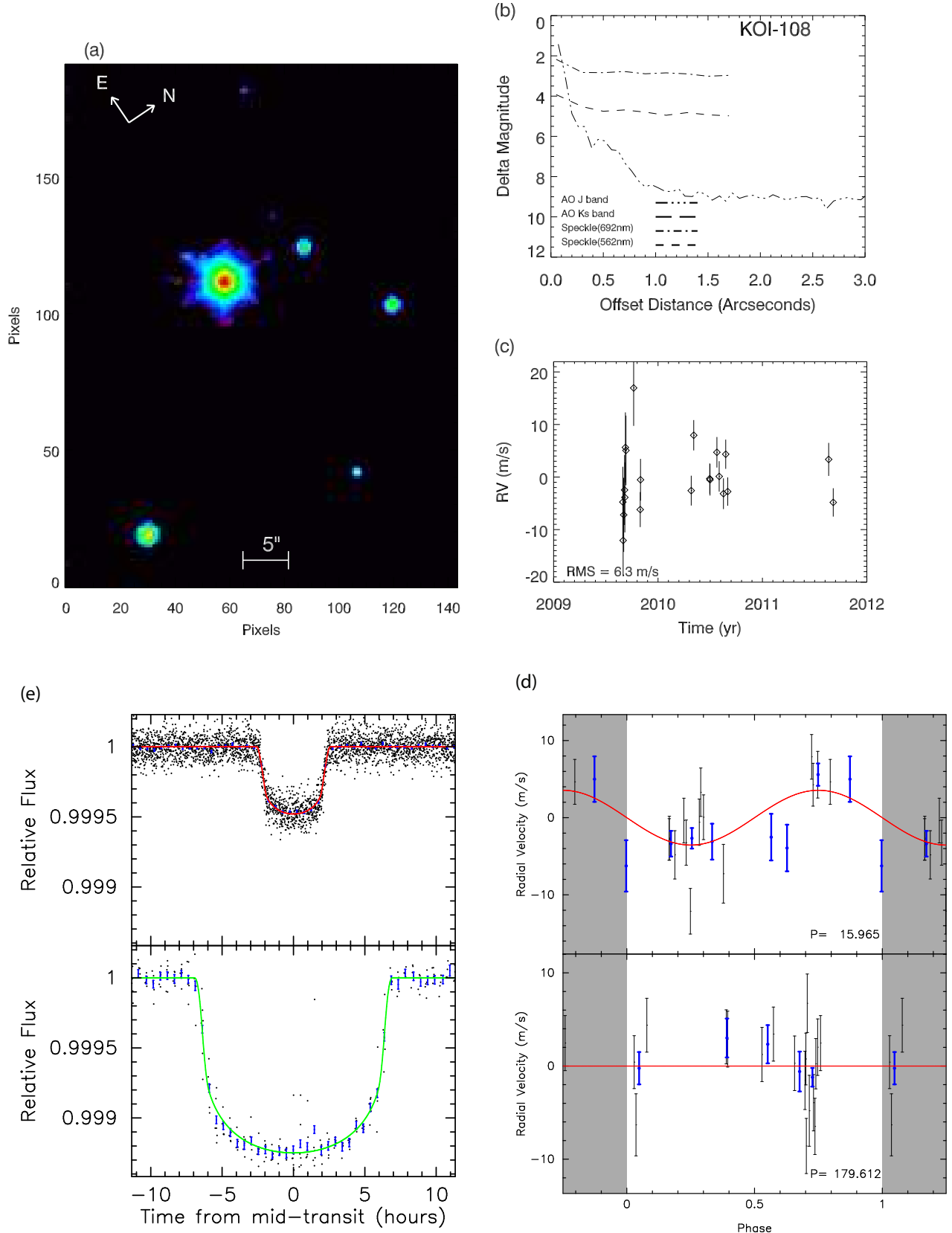


FIG. 27.— a) Keck-HIRES guider image. b) Companion star exclusion plot, c) RV time series, d) Phase folded RV curves for each planet e) Phase folded light curve for the transiting planets.

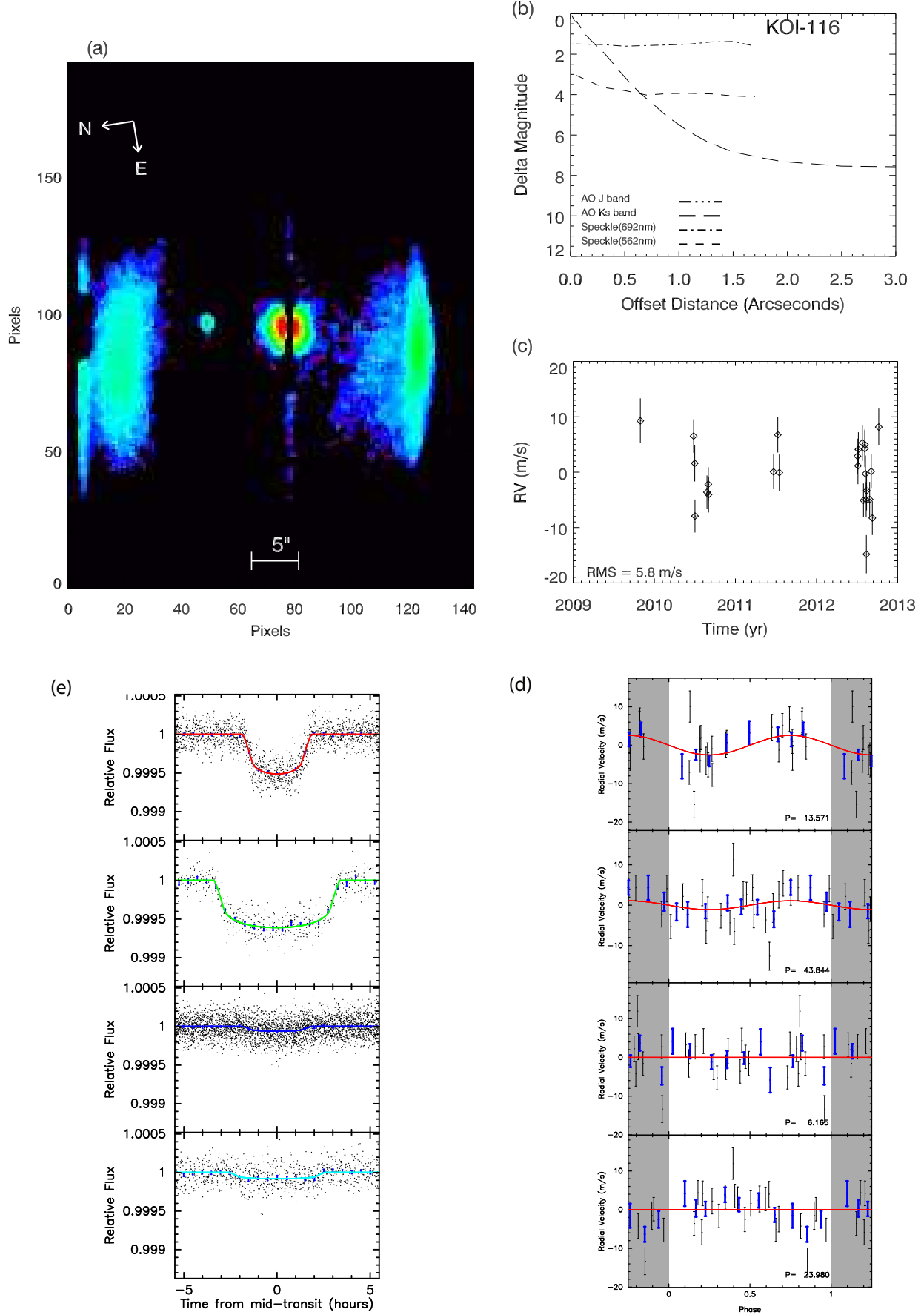


FIG. 28.— a) Keck-HIRES guider image. b) Companion star exclusion plot, c) RV time series, d) Phase folded RV curves for each planet e) Phase folded light curve for the transiting planets.

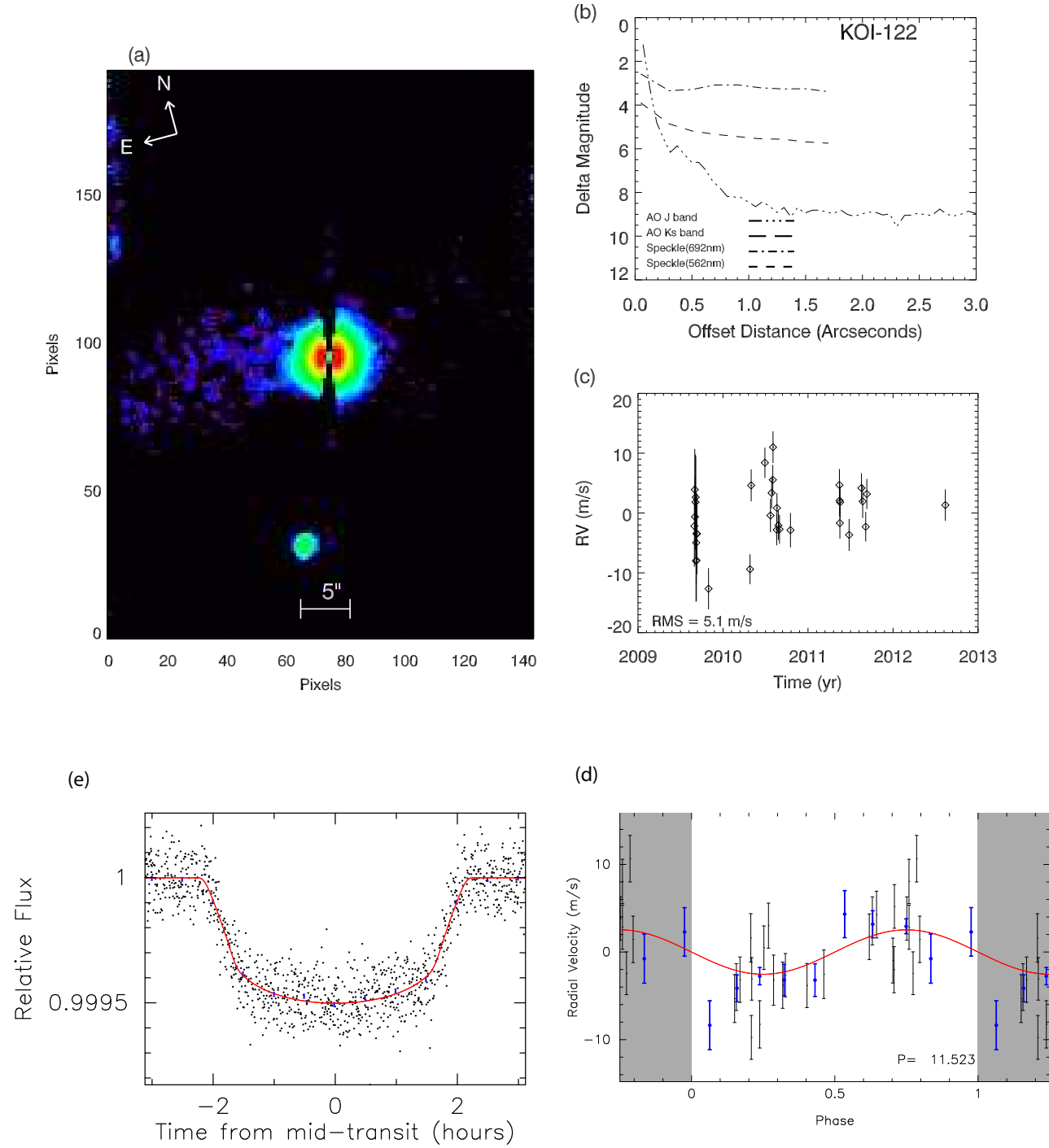


FIG. 29.— a) Keck-HIRES guider image. b) Companion star exclusion plot, c) RV time series, d) Phase folded RV curves for each planet e) Phase folded light curve for the transiting planet.

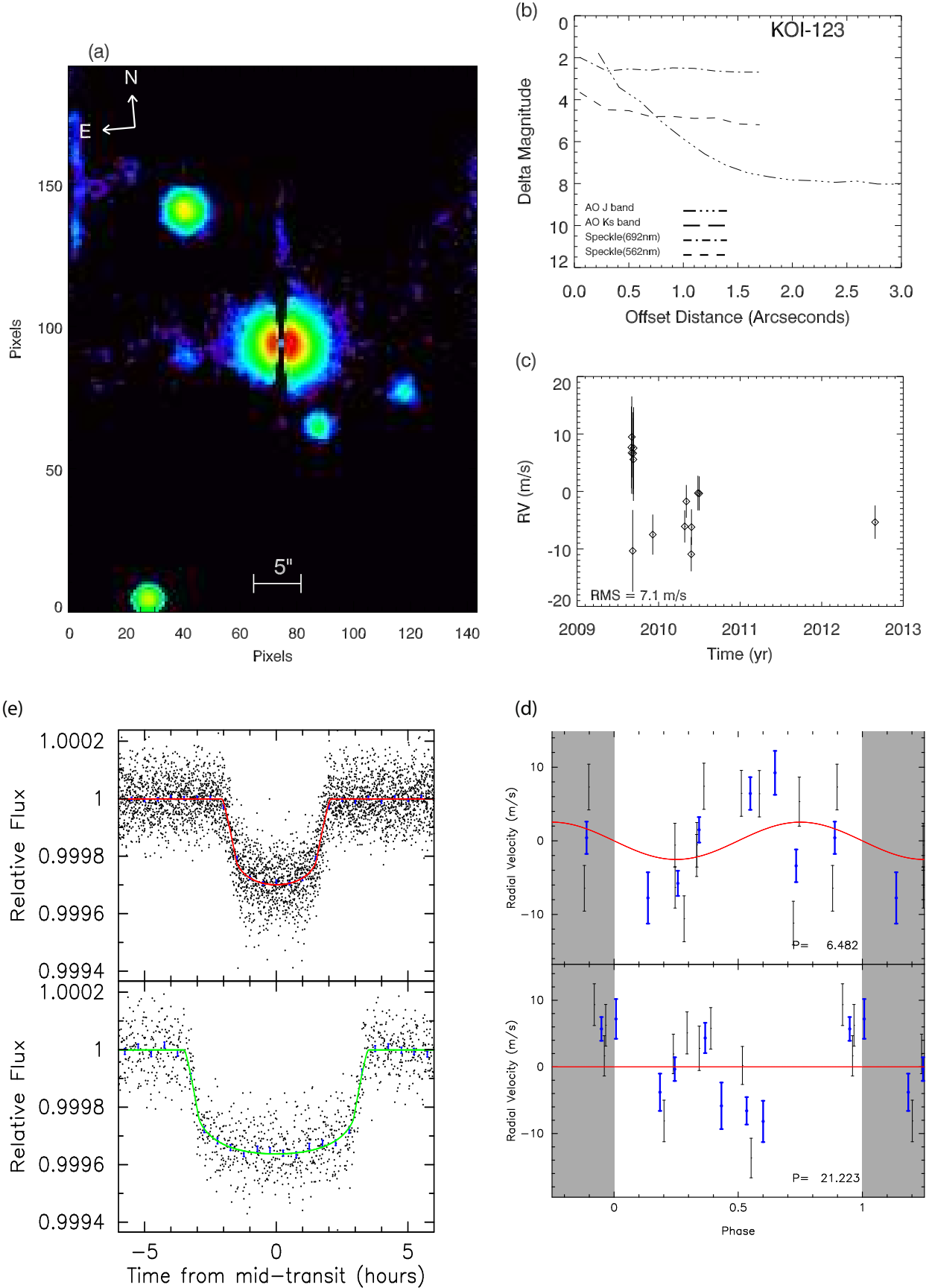


FIG. 30.— a) Keck-HIRES guider image. b) Companion star exclusion plot, c) RV time series, d) Phase folded RV curves for each planet e) Phase folded light curve for the transiting planets.

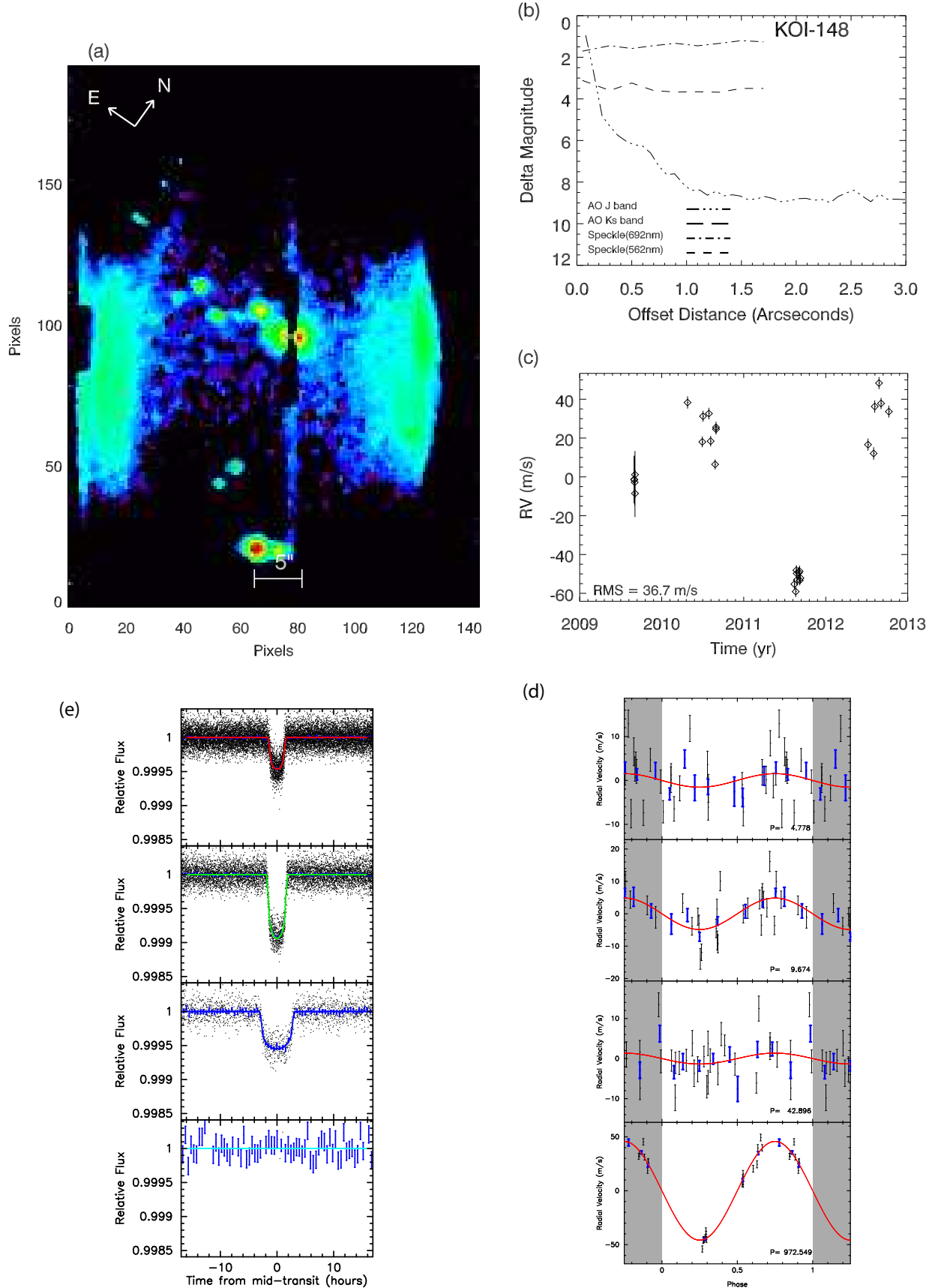


FIG. 31.— a) Keck-HIRES guider image. b) Companion star exclusion plot, c) RV time series, d) Phase folded RV curves for each planet e) Phase folded light curve for the transiting planets, and for the non-transiting planet, the light curve phase folded to the non-transiting planet period, showing lack of a transit.

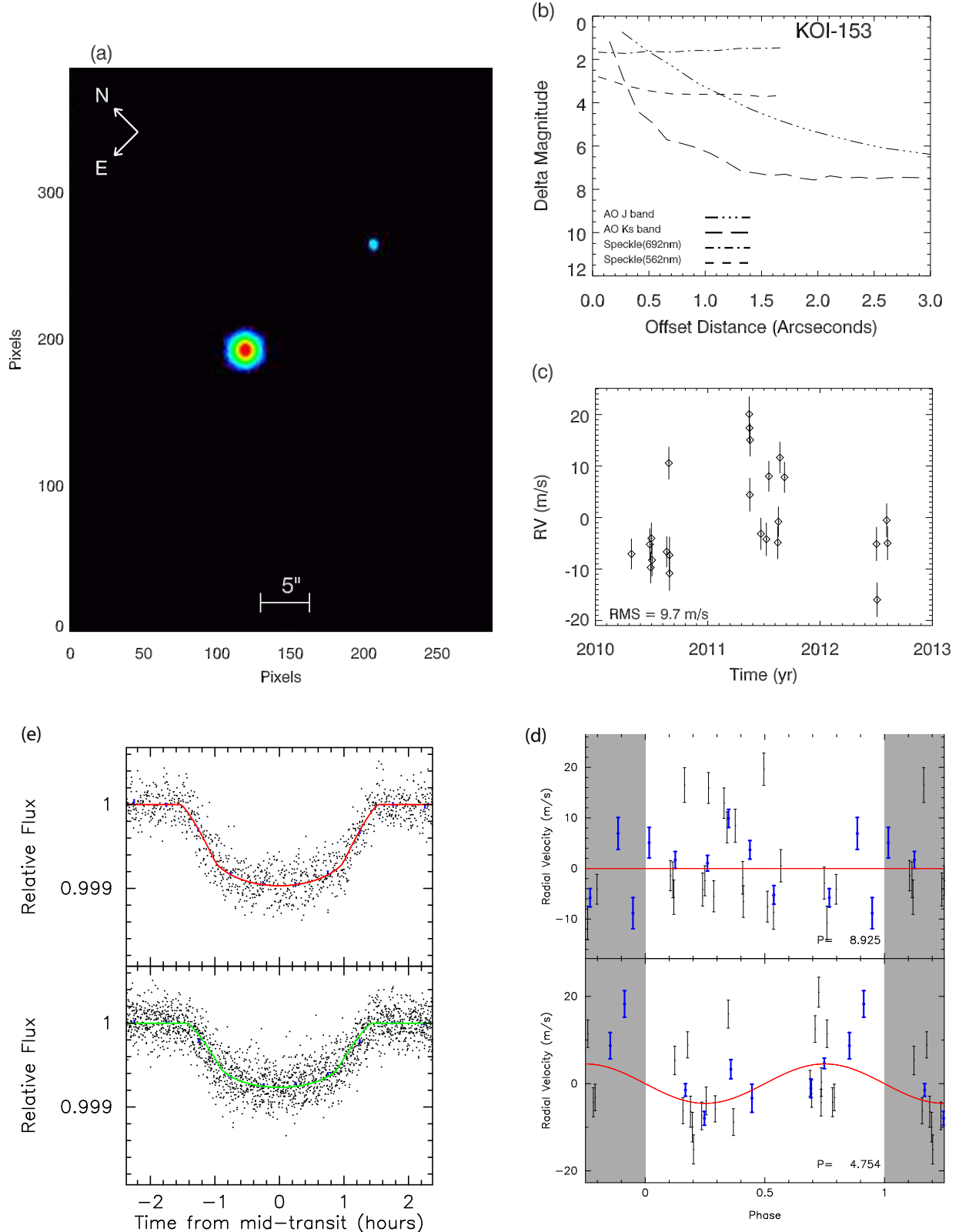


FIG. 32.— a) Keck-HIRES guider image. b) Companion star exclusion plot, c) RV time series, d) Phase folded RV curves for each planet e) Phase folded light curve for the transiting planets, and for the non-transiting planet, the light curve phase folded to the non-transiting planet period, showing lack of a transit.

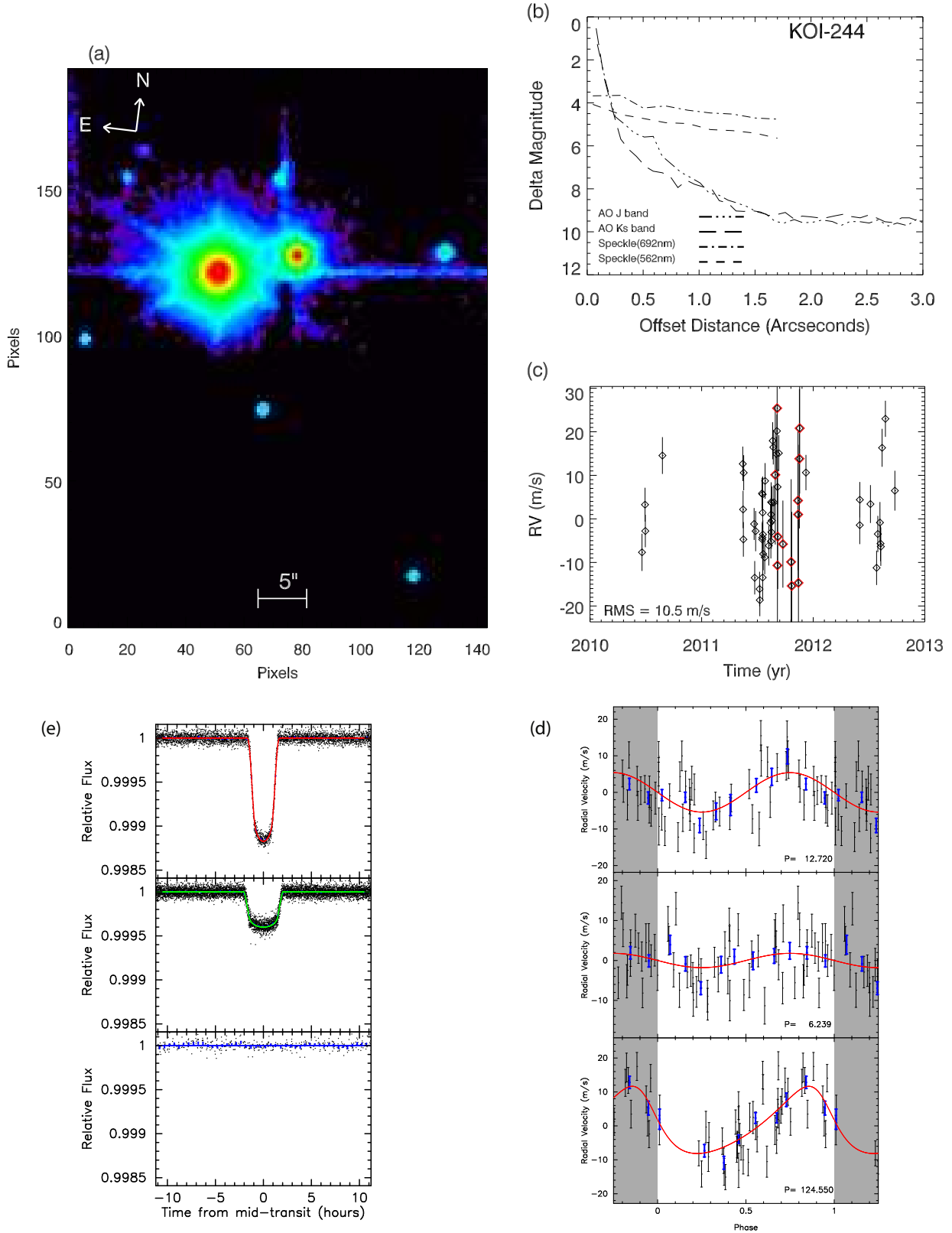


FIG. 33.— a) Keck-HIRES guider image. b) Companion star exclusion plot, c) RV time series, d) Phase folded RV curves for each planet e) Phase folded light curve for the transiting planets, and for the non-transiting planet, the light curve phase folded to the non-transiting planet period, showing lack of a transit. The RVs in red are from SOPHIE

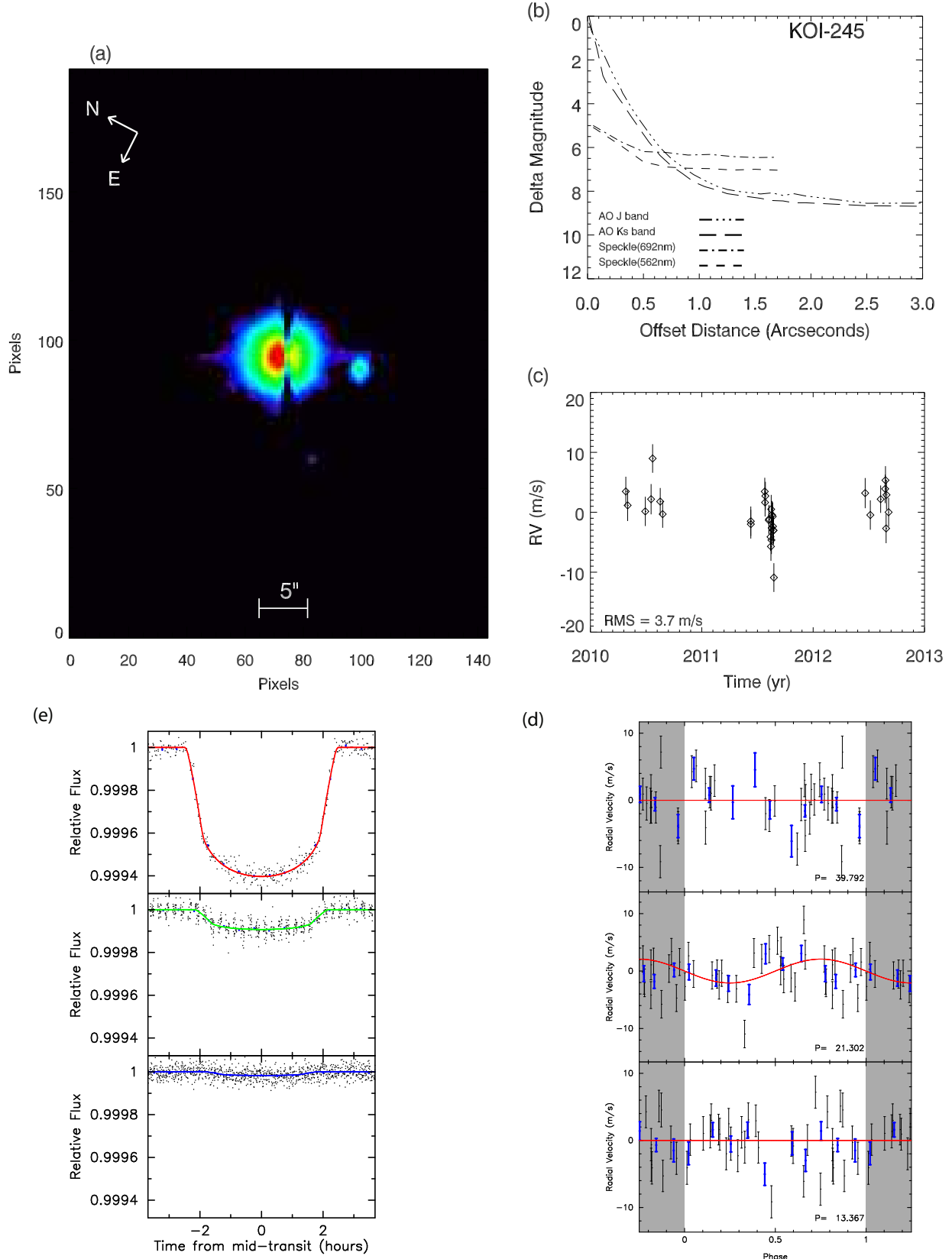


FIG. 34.— a) Keck-HIRES guider image. b) Companion star exclusion plot, c) RV time series, d) Phase folded RV curves for each planet e) Phase folded light curve for the transiting planets.

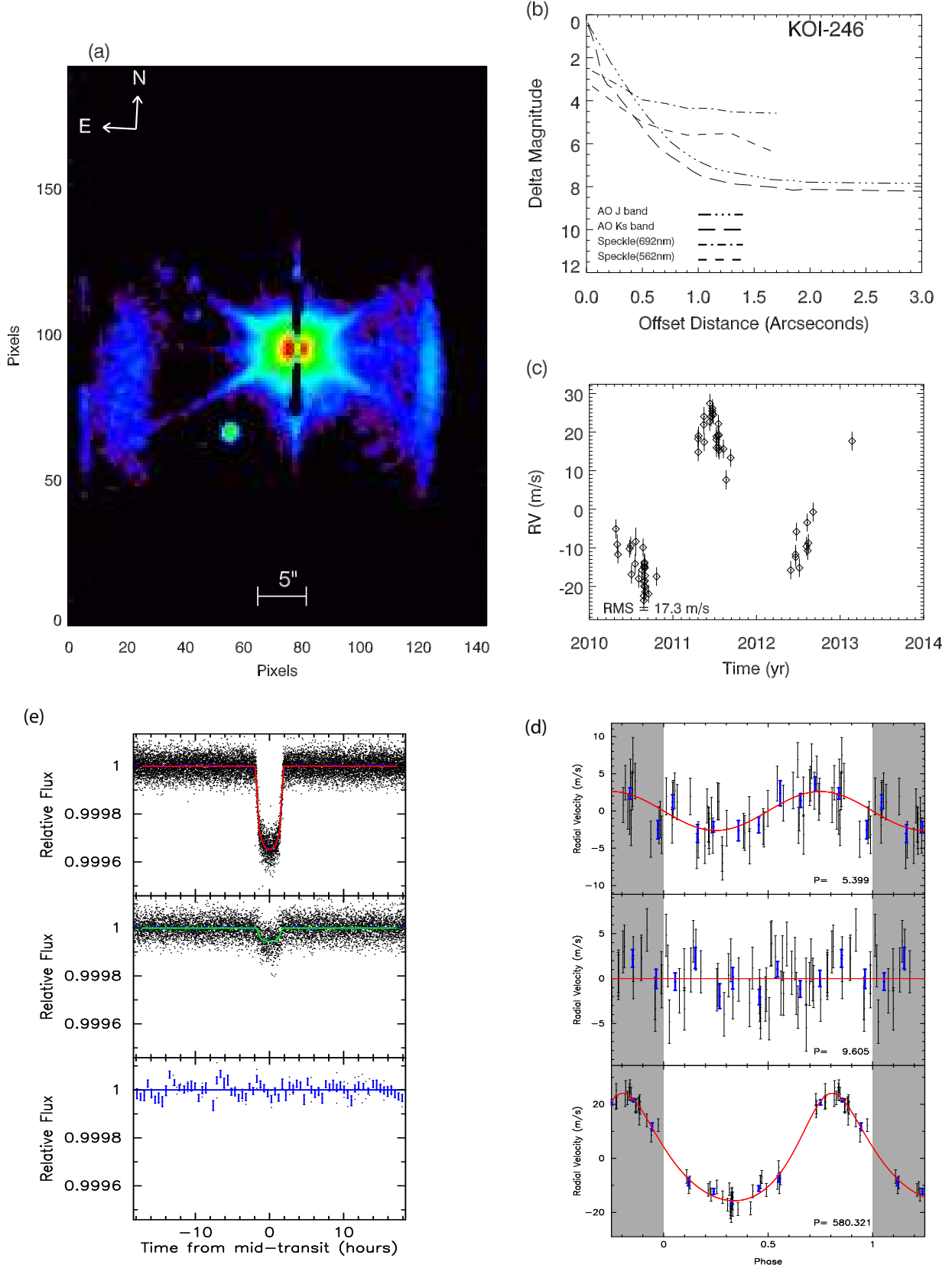


FIG. 35.— a) Keck-HIRES guider image. b) Companion star exclusion plot, c) RV time series, d) Phase folded RV curves for each planet e) Phase folded light curve for the transiting planets, and for the non-transiting planet, the light curve phase folded to the non-transiting planet period, showing lack of a transit.

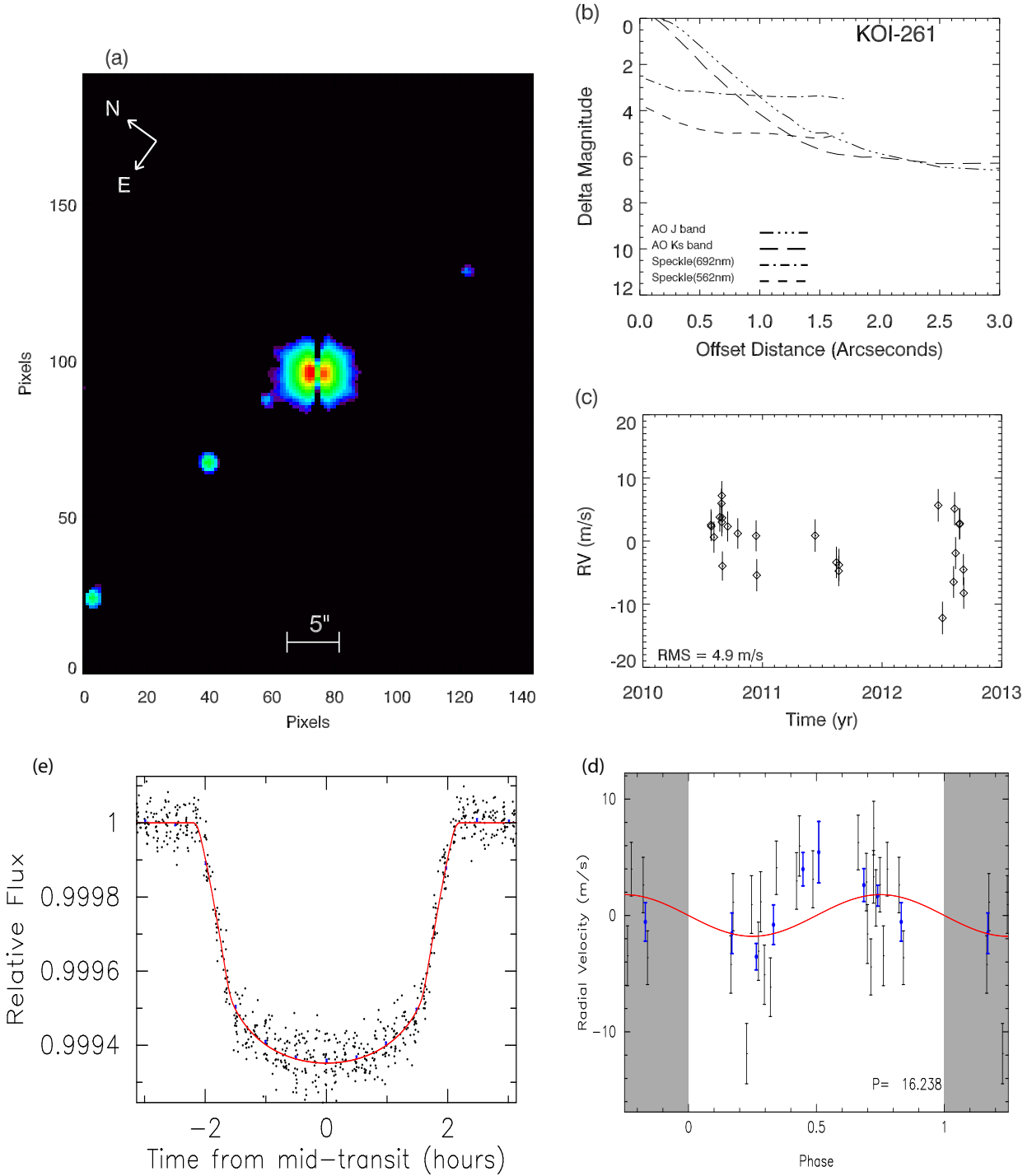


FIG. 36.— a) Keck-HIRES guider image. b) Companion star exclusion plot, c) RV time series, d) Phase folded RV curves for each planet e) Phase folded light curve for the transiting planet.

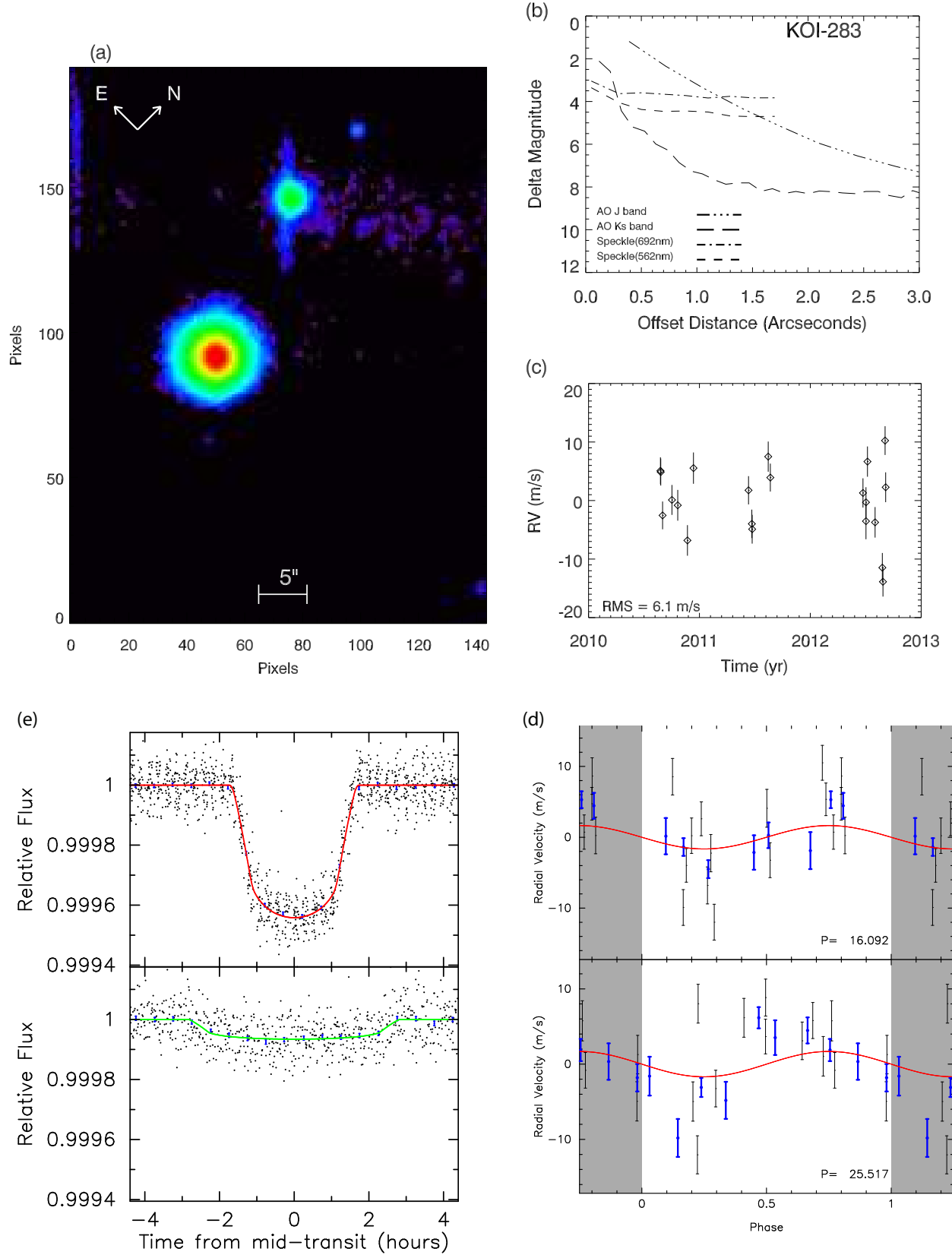


FIG. 37.— a) Keck-HIRES guider image. b) Companion star exclusion plot, c) RV time series, d) Phase folded RV curves for each planet e) Phase folded light curve for the transiting planets.

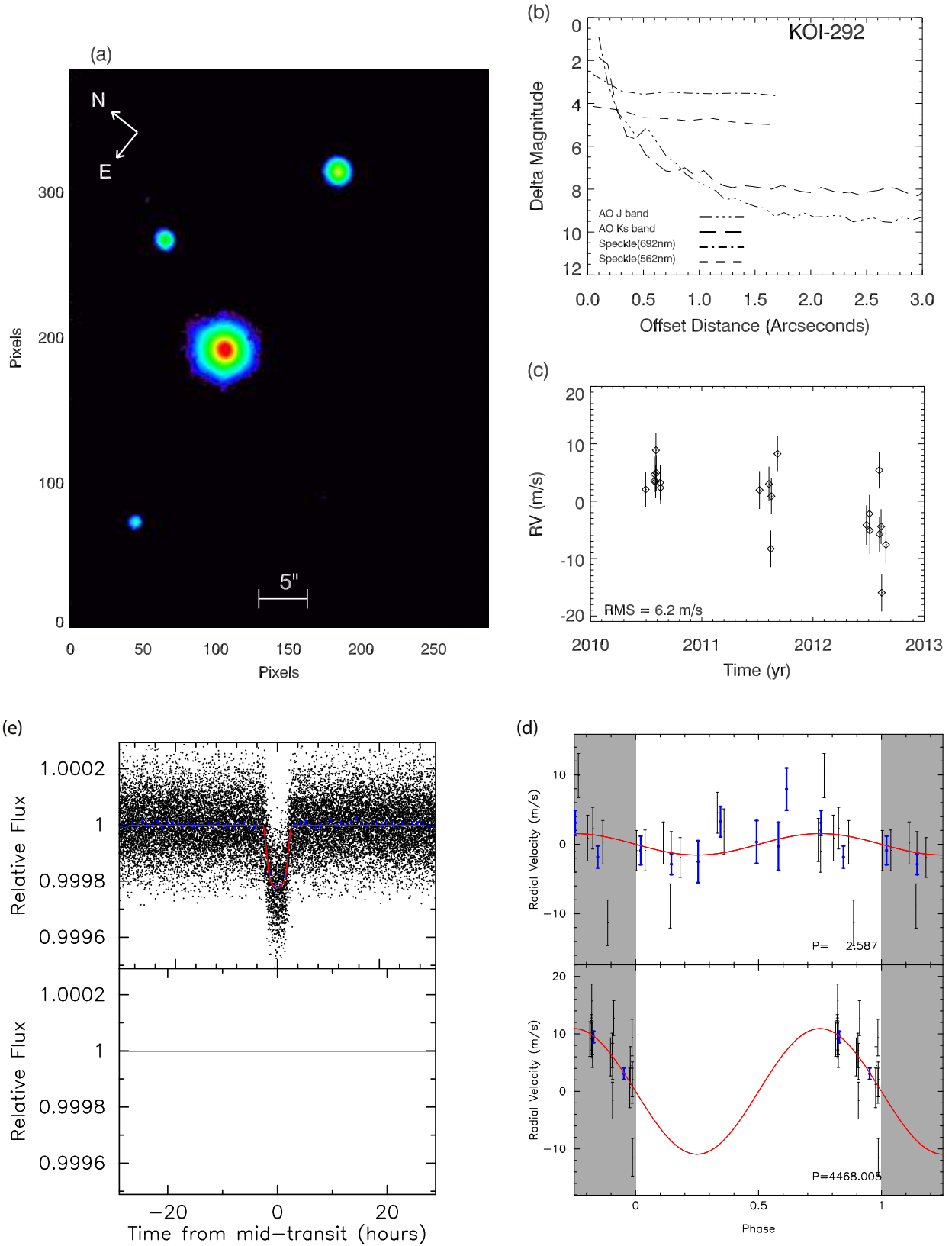


FIG. 38.— a) Keck-HIRES guider image. b) Companion star exclusion plot, c) RV time series, d) Phase folded RV curves for each planet e) Phase folded light curve for the transiting planet, and for the non-transiting planet, the light curve phase folded to the non-transiting planet period, showing lack of a transit.

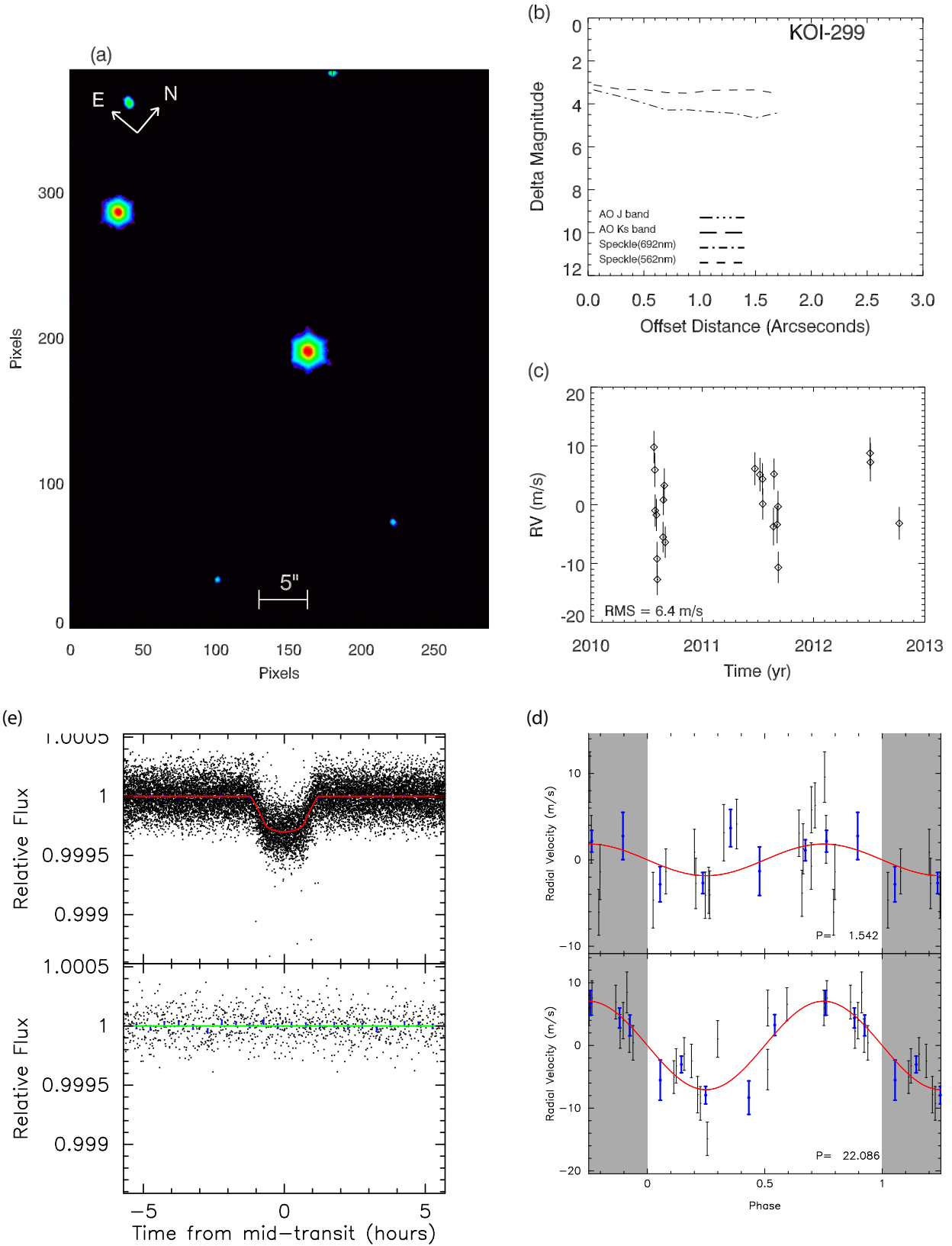


FIG. 39.— a) Keck-HIRES guider image. b) Companion star exclusion plot, c) RV time series, d) Phase folded RV curves for each planet e) Phase folded light curve for the transiting planet, and for the non-transiting planet, the light curve phase folded to the non-transiting planet period, showing lack of a transit.

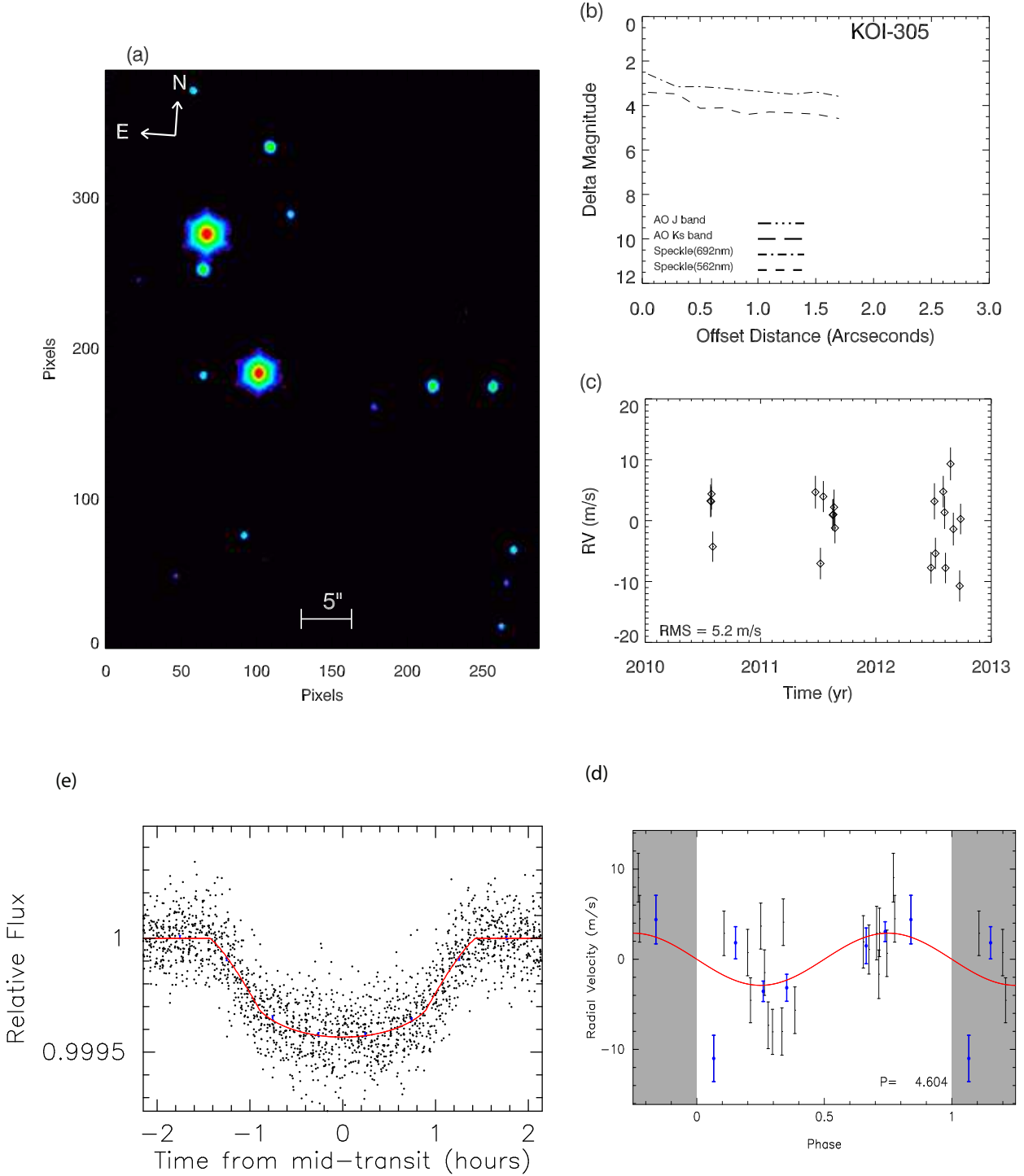


FIG. 40.— a) Keck-HIRES guider image. The southern of the two brightest stars is the KOI. b) Companion star exclusion plot, c) RV time series, d) Phase folded RV curves for each planet e) Phase folded light curve for the transiting planets.

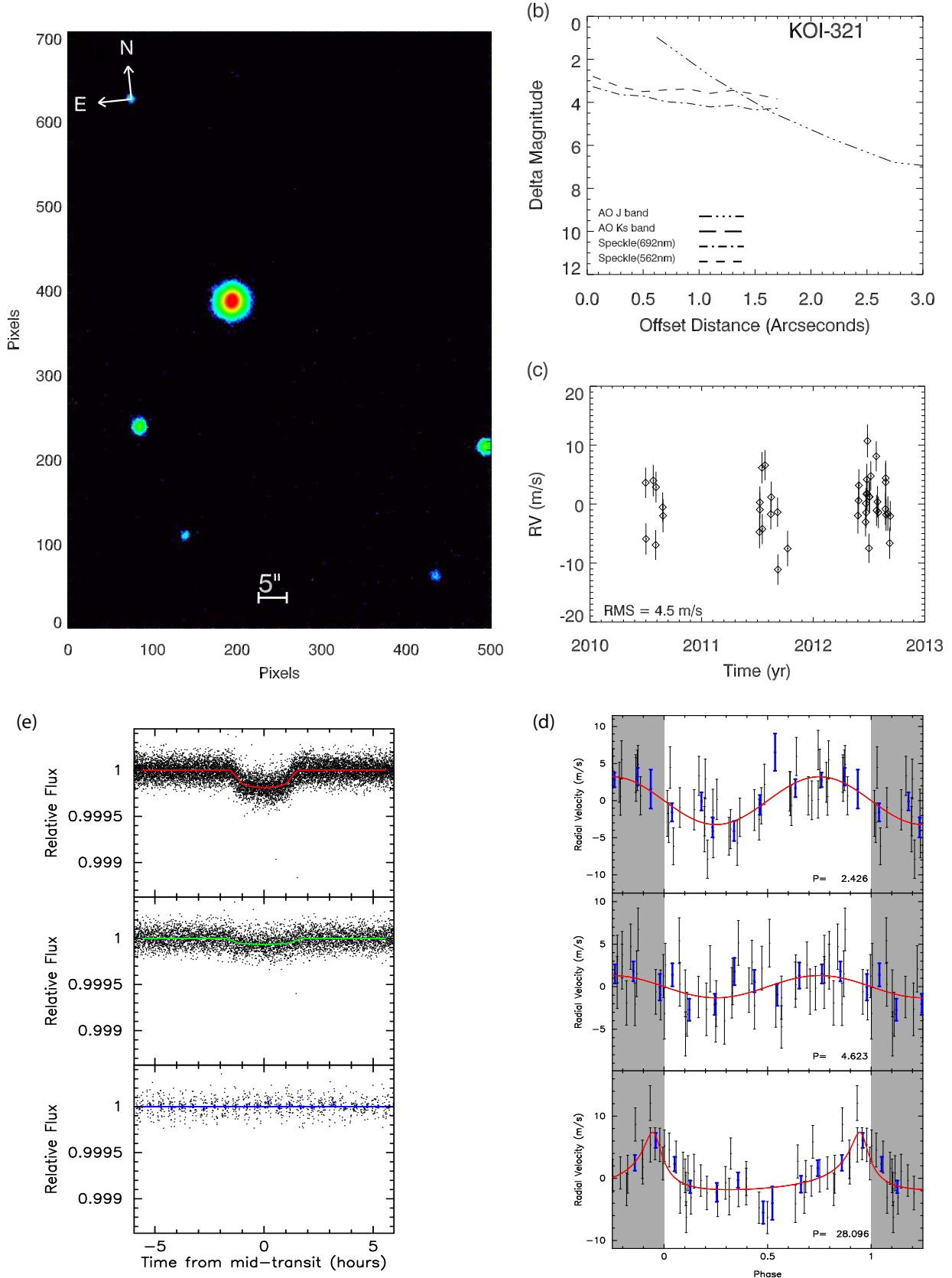


FIG. 41.— a) Keck-HIRES guider image. b) Companion star exclusion plot, c) RV time series, d) Phase folded RV curves for each planet e) Phase folded light curve for the transiting planets, and for the non-transiting planet, the light curve phase folded to the non-transiting planet period, showing lack of a transit.

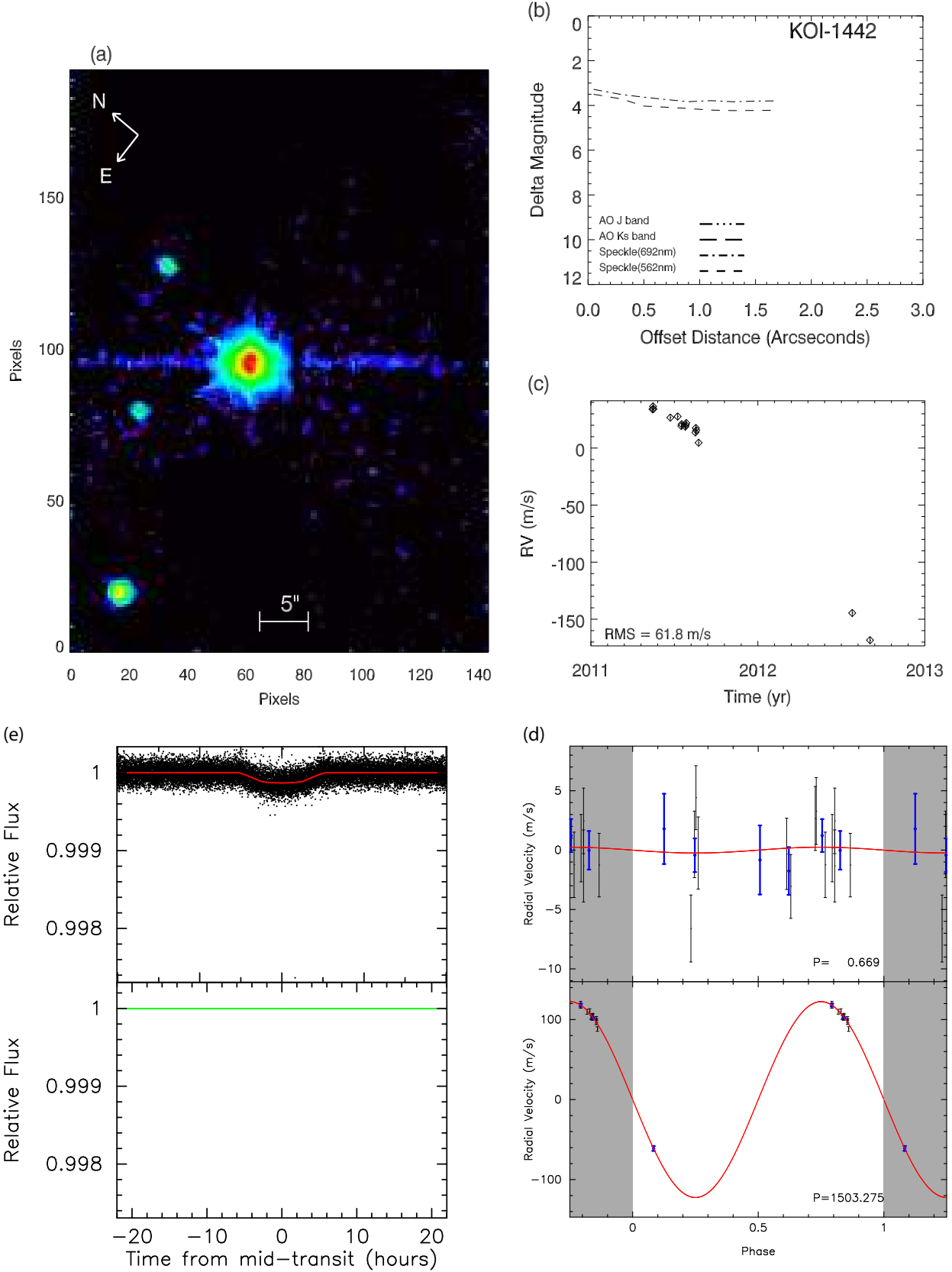


FIG. 42.— a) Keck-HIRES guider image. b) Companion star exclusion plot, c) RV time series, d) Phase folded RV curves for each planet e) Phase folded light curve for the transiting planets, and for the non-transiting planet, the light curve phase folded to the non-transiting planet period, showing lack of a transit.

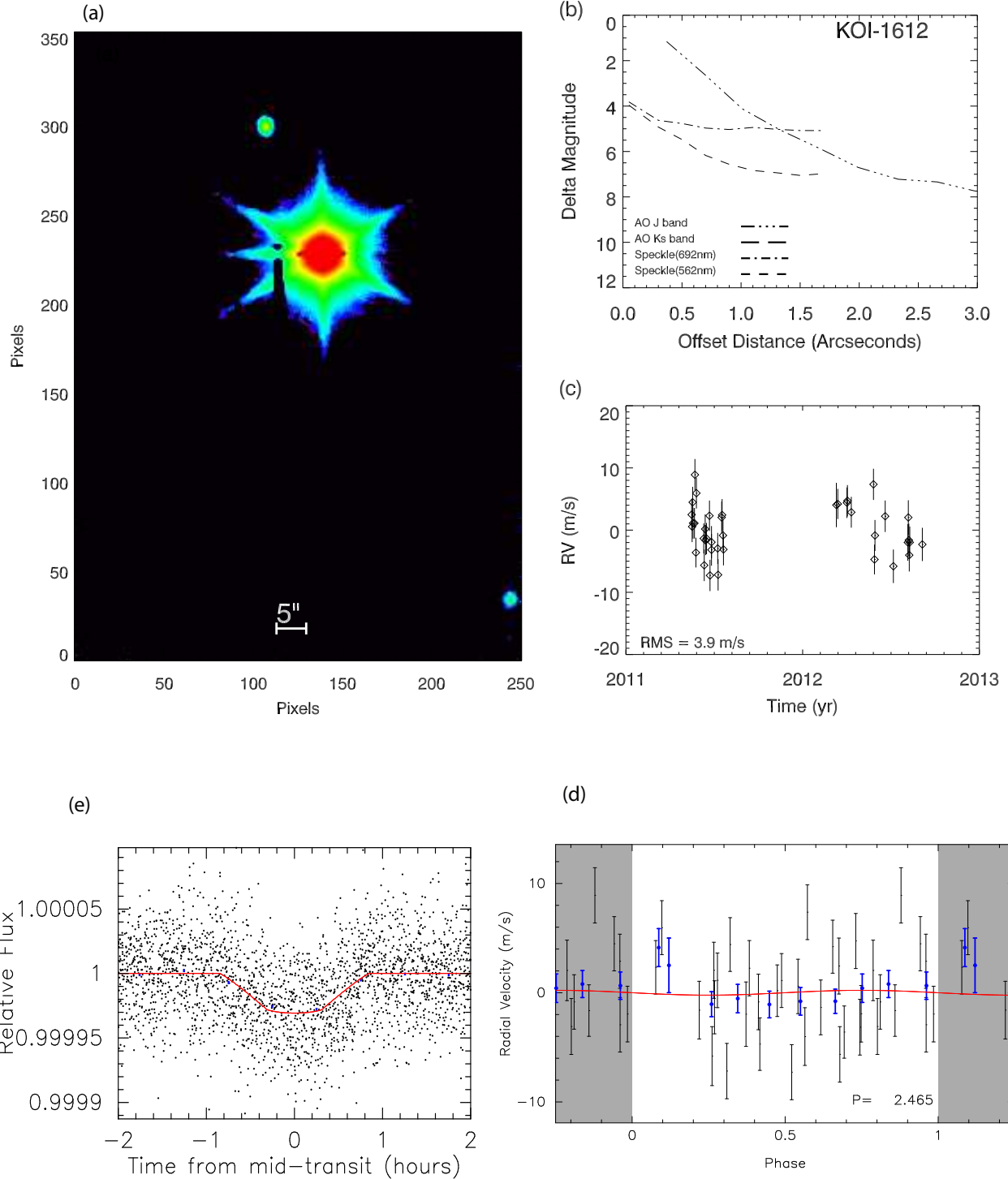


FIG. 43.— a) Keck-HIRES guider image. b) Companion star exclusion plot, c) RV time series, d) Phase folded RV curves for each planet e) Phase folded light curve for the transiting planets, and for the non-transiting planet, the light curve phase folded to the non-transiting planet period, showing lack of a transit.

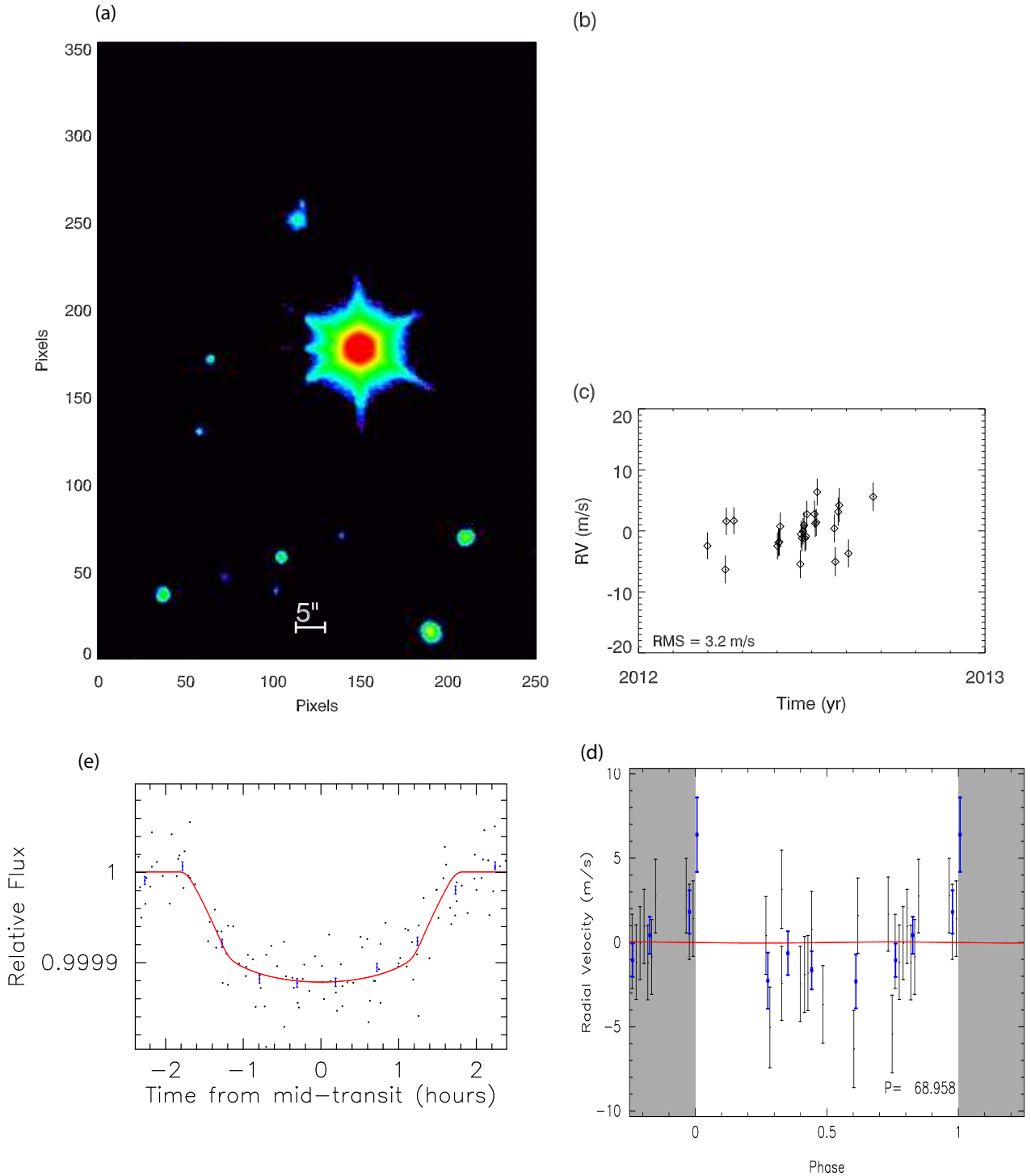


FIG. 44.— a) Keck-HIRES guider image. b) Companion star exclusion plot, c) RV time series, d) Phase folded RV curves for each planet e) Phase folded light curve for the transiting planets, and for the non-transiting planet, the light curve phase folded to the non-transiting planet period, showing lack of a transit.

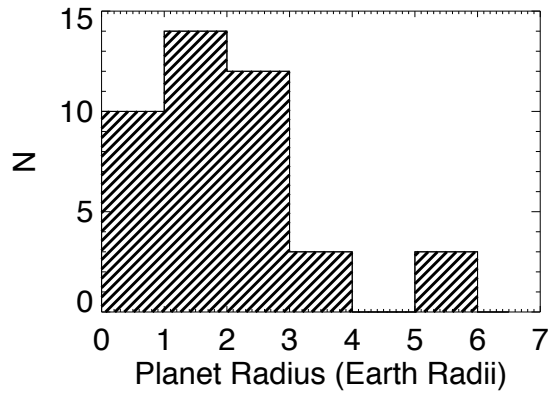


FIG. 45.— A histogram of Planet Radii

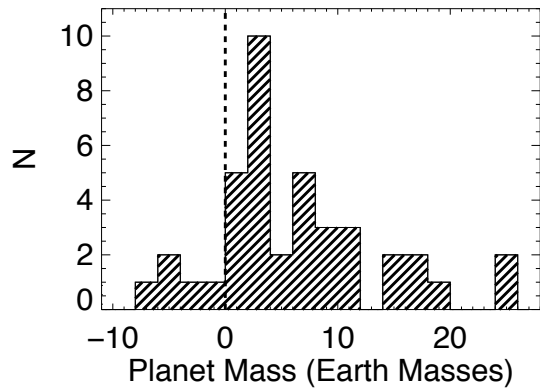


FIG. 46.— A histogram of Planet Masses

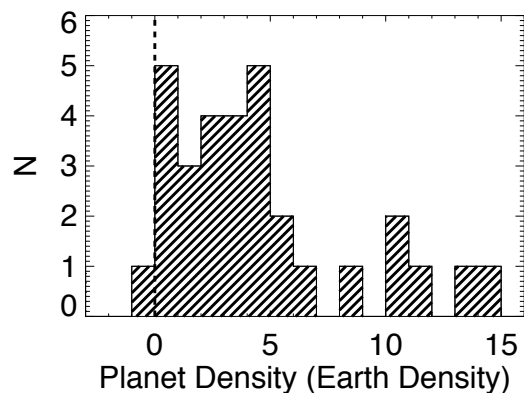


FIG. 47.— A histogram of Planet Densities

TABLE 1
 STELLAR PARAMETERS

KOI	KIC	RA	Dec	Teff (K)	Stellar $\log g$	[Fe/H]	Mstar (M_{\odot})	Rstar (R_{\odot})	$v \sin i$ (km s $^{-1}$)	Kepler Mag	Age (Gyr)	Sour
k00041	6521045	19:25:32.6	41:59:24	5825 ± 75	4.125 ± 0.03	0.02 ± 0.10	1.08 ± 0.06	1.49 ± 0.04	3.7	11.20	6.46	AS
k00069	3544595	19:25:40.3	38:40:20	5669 ± 75	4.468 ± 0.03	-0.18 ± 0.10	0.91 ± 0.06	0.92 ± 0.02	0.5	9.93	5.05	AS
k00082	10187017	18:45:55.8	47:12:28	4903 ± 44	4.607 ± 0.03	0.08 ± 0.04	0.80 ± 0.02	0.74 ± 0.02	0.5	11.49	1.41	SME
k00104	10318874	18:44:46.7	47:29:49	4781 ± 78	4.590 ± 0.04	0.34 ± 0.04	0.81 ± 0.03	0.76 ± 0.03	0.5	12.90	1.41	SME
k00108	4914423	19:15:56.2	40:03:52	5845 ± 88	4.162 ± 0.04	0.07 ± 0.11	1.09 ± 0.07	1.44 ± 0.04	2.5	12.29	5.70	AS
k00116	8395660	20:03:27.3	44:20:15	5858 ± 98	4.407 ± 0.14	-0.12 ± 0.10	1.00 ± 0.06	1.04 ± 0.17	0.3	12.88	4.83	SME
k00122	8349582	18:57:55.7	44:23:52	5699 ± 74	4.171 ± 0.04	0.30 ± 0.10	1.08 ± 0.08	1.41 ± 0.04	0.7	12.35	5.63	AS
k00123	5094751	19:21:34.2	40:17:05	5952 ± 75	4.211 ± 0.04	-0.08 ± 0.10	1.04 ± 0.06	1.32 ± 0.04	1.0	12.36	5.73	AS
k00148	5735762	19:56:33.4	40:56:56	5194 ± 43	4.487 ± 0.05	0.17 ± 0.04	0.88 ± 0.02	0.89 ± 0.05	0.5	13.04	3.14	SME
k00153	12252424	19:11:59.4	50:56:39	4725 ± 44	4.636 ± 0.03	0.05 ± 0.04	0.75 ± 0.02	0.69 ± 0.02	0.4	13.46	6.89	SME
k00244	4349452	19:06:33.2	39:29:16	6270 ± 79	4.278 ± 0.03	-0.04 ± 0.10	1.19 ± 0.06	1.31 ± 0.02	9.5	10.73	11.00	AS
k00245	8478994	18:56:14.2	44:31:05	5417 ± 75	4.567 ± 0.05	-0.32 ± 0.07	0.80 ± 0.07	0.77 ± 0.03	0.5	9.70	5.66	AS
k00246	11295426	19:24:07.7	49:02:24	5793 ± 100	4.282 ± 0.02	0.12 ± 0.04	1.08 ± 0.05	1.24 ± 0.02	0.5	10.00	9.36	AS
k00261	5383248	19:48:16.7	40:31:30	5690 ± 43	4.421 ± 0.08	0.04 ± 0.04	1.00 ± 0.02	1.02 ± 0.09	0.5	10.30	2.34	SME
k00283	5695396	19:14:07.4	40:56:32	5685 ± 44	4.417 ± 0.08	0.12 ± 0.04	1.02 ± 0.02	1.03 ± 0.10	0.4	11.52	3.66	SME
k00292	11075737	19:09:18.3	48:40:24	5779 ± 44	4.430 ± 0.08	-0.20 ± 0.04	0.94 ± 0.03	0.98 ± 0.09	0.5	12.87	8.42	SME
k00299	2692377	19:02:38.8	37:57:52	5539 ± 43	4.341 ± 0.10	0.18 ± 0.04	0.99 ± 0.02	1.11 ± 0.12	0.5	12.90	2.79	SME
k00305	6063220	19:49:24.9	41:18:00	4782 ± 115	4.605 ± 0.05	0.18 ± 0.04	0.79 ± 0.03	0.73 ± 0.04	0.5	12.97	1.47	SME
k00321	8753657	19:27:23.5	44:58:05	5538 ± 44	4.409 ± 0.02	0.18 ± 0.04	1.07 ± 0.04	1.07 ± 0.02	0.4	12.52	5.84	AS
k01442	11600889	19:04:08.7	49:36:52	5476 ± 46	4.426 ± 0.06	0.04 ± 0.00	1.00 ± 0.02	1.01 ± 0.07	2.0	12.52	7.47	SME
k01612	10963065	18:59:08.6	48:25:23	6104 ± 74	4.294 ± 0.03	-0.20 ± 0.10	1.08 ± 0.07	1.23 ± 0.03	3.1	8.77	6.68	AS
k01925	9955598	19:34:43.0	46:51:09	5460 ± 75	4.499 ± 0.03	0.08 ± 0.10	0.92 ± 0.06	0.89 ± 0.02	2.0	9.44	6.80	AS

TABLE 2
 PLANET PROPERTIES AND ORBITAL PARAMETERS

KOI	Period (days)	Radius (R_{\oplus})	Mass (M_{\oplus})	Planet Density (g cm^{-3})	K (m s^{-1})	Stellar density (g cm^{-3})	Impact Parameter	a/Rstar	Epoch (BJD- 2454900)
41.01	12.8159	2.2 ± 0.05	0.85 ± 4.0	0.35 ± 1.65	0.18 ± 0.8	0.44 ± 0.01	0.05 ± 0.04	0.013550	55.94713
41.02	6.88705	1.3 ± 0.04	7.34 ± 3.2	14.25 ± 6.33	1.90 ± 0.8	0.44 ± 0.01	0.54 ± 0.02	0.008094	66.17797
41.03	35.3331	1.6 ± 0.05	-5.31 ± 7.0	-5.57 ± 7.47	-0.79 ± 1.0	0.44 ± 0.01	0.75 ± 0.01	0.009926	86.98031
69.01	4.72674	1.5 ± 0.03	2.59 ± 2.0	4.17 ± 3.29	1.05 ± 0.8	1.64 ± 0.01	0.20 ± 0.02	0.014927	67.92580
69.10	>1131	...	>715	...	>47
82.01	16.1457	2.2 ± 0.07	8.93 ± 2.0	4.68 ± 1.12	2.77 ± 0.6	2.76 ± 0.09	0.30 ± 0.03	0.027639	67.75384
82.02	10.3117	1.2 ± 0.04	3.80 ± 1.8	13.27 ± 6.46	1.37 ± 0.6	2.76 ± 0.09	0.22 ± 0.05	0.014682	67.07920
82.03	27.4536	0.9 ± 0.03	8.12 ± 2.9	68.23 ± 25.45	2.11 ± 0.8	2.76 ± 0.09	0.57 ± 0.03	0.010963	78.02565
82.04	7.07142	0.6 ± 0.02	-2.45 ± 1.5	-72.00 ± 43.86	-1.00 ± 0.6	2.76 ± 0.09	0.06 ± 0.05	0.007228	72.98486
82.05	5.28696	0.5 ± 0.02	0.41 ± 1.6	23.29 ± 94.93	0.19 ± 0.7	2.76 ± 0.09	0.06 ± 0.06	0.005800	68.84920
104.01	2.50806	3.5 ± 0.15	10.84 ± 1.4	1.45 ± 0.26	6.11 ± 0.8	2.90 ± 0.23	0.85 ± 0.01	0.042380	67.99980
104.10	821 ± 3	...	3239 ± 202	...	263.34 ± 13.9
108.01	15.9654	3.4 ± 0.09	18.69 ± 4.7	2.23 ± 0.59	3.73 ± 0.9	0.52 ± 0.02	0.72 ± 0.01	0.021500	75.17614
108.02	179.612	5.1 ± 0.14	-22.54 ± 14.3	-0.76 ± 0.49	-2.01 ± 1.3	0.52 ± 0.02	0.44 ± 0.02	0.032766	228.32581
116.01	13.5708	2.5 ± 0.32	10.44 ± 3.2	3.28 ± 1.56	2.71 ± 0.8	1.38 ± 0.15	0.69 ± 0.03	0.022113	69.27837
116.02	43.8445	2.6 ± 0.33	11.17 ± 5.8	3.10 ± 2.07	1.95 ± 1.0	1.38 ± 0.15	0.28 ± 0.13	0.022676	84.93360
116.03	6.16486	0.8 ± 0.11	0.15 ± 2.8	1.26 ± 26.26	0.05 ± 0.9	1.38 ± 0.15	0.39 ± 0.15	0.007258	68.64035
116.04	23.9802	0.9 ± 0.13	-13.34 ± 4.4	-77.00 ± 39.75	-2.84 ± 0.9	1.38 ± 0.15	0.45 ± 0.11	0.008362	80.53263
122.01	11.5231	3.4 ± 0.09	13.0 ± 2.9	1.71 ± 0.37	3.36 ± 0.6	0.54 ± 0.02	0.74 ± 0.01	0.022166	64.96841
123.01	6.48163	2.4 ± 0.07	1.3 ± 5.4	0.3 ± 2.2	0.29 ± 1.8	0.65 ± 0.02	0.58 ± 0.02	0.016434	55.97755
123.02	21.2227	2.5 ± 0.07	2.22 ± 7.8	0.65 ± 2.30	0.43 ± 1.5	0.65 ± 0.02	0.16 ± 0.08	0.017432	70.57250
148.01	4.77800	1.9 ± 0.10	3.94 ± 2.1	3.23 ± 1.84	1.62 ± 0.9	1.98 ± 0.13	0.17 ± 0.11	0.019318	57.06113
148.02	9.67395	2.7 ± 0.14	14.61 ± 2.3	4.01 ± 0.91	4.74 ± 0.7	1.98 ± 0.13	0.38 ± 0.05	0.027892	58.33925
148.03	42.8961	2.0 ± 0.11	7.93 ± 4.6	5.08 ± 3.12	1.57 ± 0.9	1.98 ± 0.13	0.20 ± 0.11	0.021021	79.06554
148.10	972 ± 8	...	657 ± 25	...	45.83 ± 0.8
153.01	8.92507	2.2 ± 0.06	-5.7 ± 5.2	-5.0 ± 2.7	-2.72 ± 1.5	2.71 ± 0.08	0.56 ± 0.02	0.029135	72.71374
153.02	4.75400	1.8 ± 0.05	7.1 ± 3.3	6.6 ± 3.0	2.36 ± 1.5	2.71 ± 0.08	0.08 ± 0.06	0.024190	61.54630
153.10	16.0 ± 0.8	...	30 ± 4	...	9.64 ± 1.1
244.01	12.7204	5.2 ± 0.09	24.60 ± 5.7	0.90 ± 0.21	5.63 ± 1.3	0.75 ± 0.01	0.88 ± 0.00	0.036409	111.52730
244.02	6.2385	2.7 ± 0.05	9.6 ± 4.20	2.50 ± 1.10	2.80 ± 1.2	0.75 ± 0.01	0.54 ± 0.01	0.018950	104.70541
244.10	123 ± 2	...	89.90 ± 13.7	...	9.67 ± 1.5
245.01	39.7922	1.9 ± 0.06	-5.98 ± 4.1	-4.56 ± 3.17	-1.33 ± 0.9	2.46 ± 0.04	0.53 ± 0.01	0.023068	108.24950
245.02	21.3020	0.8 ± 0.03	3.35 ± 4.0	44.33 ± 53.60	0.92 ± 1.1	2.46 ± 0.04	0.43 ± 0.02	0.008909	124.83685
245.03	13.3675	0.3 ± 0.02	-0.42 ± 2.8	-70.00 ± 490.00	-0.14 ± 0.9	2.46 ± 0.04	0.48 ± 0.13	0.003828	117.04171
246.01	5.39875	2.3 ± 0.02	7.89 ± 2.4	3.06 ± 0.92	2.50 ± 0.8	0.79 ± 0.01	0.48 ± 0.01	0.017383	106.85783
246.02	9.60504	1.0 ± 0.02	2.18 ± 3.5	10.77 ± 17.29	0.57 ± 0.9	0.79 ± 0.01	0.77 ± 0.01	0.007455	69.38025
246.10	579 ± 17	...	283 ± 11	...	19.86 ± 0.8
261.01	16.2385	2.7 ± 0.22	8.46 ± 3.4	2.26 ± 1.11	2.10 ± 0.8	1.54 ± 0.25	0.54 ± 0.07	0.023967	104.01897
283.01	16.0920	2.4 ± 0.20	16.13 ± 3.5	6.00 ± 1.98	3.95 ± 0.8	1.44 ± 0.21	0.79 ± 0.02	0.021263	103.59795
283.02	25.5169	0.8 ± 0.07	17.02 ± 4.6	150.00 ± 56.93	3.58 ± 0.9	1.44 ± 0.21	0.27 ± 0.16	0.007394	87.42342
292.01	2.58664	1.5 ± 0.13	3.51 ± 1.9	5.44 ± 3.48	1.65 ± 0.9	1.53 ± 0.31	0.41 ± 0.16	0.013803	104.84121
292.10	>789	...	>344	...	>25
299.01	1.54168	2.0 ± 0.22	3.55 ± 1.6	2.18 ± 1.21	1.82 ± 0.8	1.12 ± 0.34	0.56 ± 0.14	0.016377	103.54328
299.10	22.09 ± 0.04	...	32.49 ± 4.8	...	6.90 ± 0.9
305.01	4.60358	1.5 ± 0.08	6.15 ± 1.3	10.90 ± 2.82	2.91 ± 0.6	2.86 ± 0.23	0.21 ± 0.13	0.018475	104.83893
321.01	2.42629	1.4 ± 0.03	6.35 ± 1.4	11.82 ± 2.70	2.89 ± 0.6	1.12 ± 0.02	0.10 ± 0.06	0.012285	103.45680
321.02	4.62332	0.8 ± 0.03	2.71 ± 1.8	24.39 ± 16.13	1.00 ± 0.6	1.12 ± 0.02	0.36 ± 0.06	0.007261	65.37438
321.10	28.10 ± 0.07	...	21.81 ± 4.4	...	4.38 ± 0.9
1442.01	0.669310	1.1 ± 0.02	0.06 ± 1.2	0.29 ± 5.70	0.05 ± 0.9	1.38 ± 0.16	0.25 ± 0.15	0.010414	67.13162
1442.10	>1100	...	>3330	...	>205
1612.01	2.46502	0.8 ± 0.03	0.48 ± 3.2	4.42 ± 29.82	0.20 ± 1.3	0.82 ± 0.01	0.92 ± 0.01	0.006136	65.67928
1925.01	68.9584	1.2 ± 0.03	2.69 ± 6.2	8.88 ± 20.60	0.45 ± 1.0	1.81 ± 0.00	0.90 ± 0.01	0.012223	112.08151

TABLE 3
FALSE POSITIVE PROBABILITIES

KOI	P _{EB}	P _{HEB}	P _{BGEB}	P _{BGPL}	P _{PL}	FPP
41.01	5.46e-12	1.14e-09	2.57e-05	6.68e-08	0.31	2.57e-05
41.02	9.75e-14	2.32e-07	1.06e-04	2.26e-06	0.12	1.08e-04
41.03	8.74e-15	5.41e-05	3.13e-04	1.06e-05	0.19	3.77e-04
69.01	1.50e-06	5.73e-09	8.77e-12	1.99e-12	0.16	1.50e-06
82.01	8.56e-08	1.18e-03	9.18e-07	3.92e-08	0.31	1.18e-03
82.02	2.16e-15	2.81e-05	1.48e-05	8.10e-06	0.09	5.11e-05
82.03	1.89e-21	2.45e-04	2.39e-03	4.62e-05	0.03	2.68e-03
82.04	1.48e-14	6.66e-05	2.41e-02	1.08e-03	0.00	2.52e-02
82.05	1.17e-05	1.46e-04	3.55e-02	7.21e-03	0.00	4.29e-02
104.01	4.82e-03	1.00e-01	1.01e-05	6.28e-07	0.21	1.05e-01
108.01	2.91e-09	2.58e-05	2.71e-08	3.74e-08	0.23	2.59e-05
108.02	3.52e-09	2.02e-02	1.12e-08	1.16e-10	0.08	2.02e-02
116.01	6.44e-08	3.15e-03	2.33e-05	1.77e-06	0.31	3.17e-03
116.02	1.19e-07	1.36e-03	7.35e-05	5.88e-09	0.31	1.44e-03
116.03	3.56e-11	3.66e-06	2.28e-03	4.85e-04	0.02	2.77e-03
116.04	3.78e-08	4.77e-04	3.47e-03	1.24e-06	0.04	3.95e-03
122.01	1.08e-06	3.57e-06	3.08e-08	3.78e-08	0.23	4.72e-06
123.01	1.21e-07	7.16e-10	6.76e-06	5.16e-06	0.31	1.20e-05
123.02	1.01e-11	1.05e-08	1.40e-07	3.00e-07	0.31	4.50e-07
148.01	1.03e-06	1.43e-05	1.04e-05	2.46e-07	0.29	2.60e-05
148.02	8.88e-08	9.00e-05	9.24e-08	3.40e-11	0.27	9.01e-05
148.03	3.90e-10	6.96e-04	2.05e-05	3.95e-07	0.31	7.17e-04
153.01	5.35e-08	1.03e-03	1.60e-06	1.61e-06	0.31	1.03e-03
153.02	1.28e-07	2.66e-05	6.11e-06	2.20e-06	0.25	3.51e-05
244.01	3.32e-05	1.02e-02	1.94e-08	4.68e-19	0.08	1.02e-02
244.02	4.10e-08	1.40e-04	2.01e-13	4.36e-15	0.31	1.40e-04
245.01	5.08e-09	1.48e-03	5.45e-09	1.69e-17	0.27	1.48e-03
245.02	2.56e-11	7.40e-05	6.29e-04	3.30e-05	0.02	7.36e-04
246.01	4.11e-07	3.76e-08	1.64e-07	3.63e-10	0.31	6.12e-07
246.02	4.36e-13	1.53e-03	2.45e-03	1.26e-04	0.07	4.11e-03
283.01	4.43e-08	3.21e-03	2.62e-05	1.04e-08	0.31	3.23e-03
283.02	1.00e-18	7.37e-04	1.26e-03	1.14e-04	0.02	2.11e-03
292.01	2.57e-07	5.26e-13	1.09e-05	4.39e-06	0.15	1.55e-05
299.01	2.14e-07	3.94e-09	2.61e-05	8.95e-06	0.28	3.53e-05
305.01	7.03e-08	4.17e-05	4.00e-05	3.58e-06	0.15	8.54e-05
321.01	1.88e-08	2.71e-11	9.28e-05	2.96e-05	0.15	1.22e-04
321.02	9.70e-10	8.75e-07	3.07e-04	7.38e-04	0.03	1.05e-03
1442.01	2.52e-12	4.59e-33	3.85e-06	4.80e-05	0.07	5.18e-05
1612.01	4.95e-04	8.67e-04	3.74e-01	1.76e-02	0.02	3.93e-01
1925.01	4.25e-05	1.68e-02	6.16e-02	1.22e-03	0.09	7.96e-02

TABLE 4
RADIAL VELOCITIES FOR KOI-0041

BJD – 2450000	Radial Velocity (m s ⁻¹)	Uncertainty (m s ⁻¹)	R' _{HK}
4989.010954	-4.46	3.73	-5.028
5042.015300	-11.82	3.81	-5.034
5042.022823	-9.46	3.86	-5.028
5042.030068	-6.02	3.77	-5.041
5042.842452	-3.45	3.63	-5.041
5042.849778	8.90	3.75	-5.014
5044.044453	5.07	3.73	-5.034
5044.051871	3.30	3.77	-5.014
5044.059302	0.62	3.73	-5.028
5048.909978	-7.17	3.93	-5.014
5073.846868	-1.39	3.70	-5.041
5074.844066	0.39	3.59	-5.034
5075.868856	3.61	3.67	-5.028
5076.756808	6.56	3.65	-5.021
5077.894672	-9.78	3.64	-5.048
5078.934772	-3.54	3.71	-5.014
5079.962974	-0.23	3.71	-5.041
5081.002505	-3.08	3.55	-4.953
5082.982668	2.99	3.77	-5.041
5312.060754	-1.25	2.78	-5.041
5400.916085	2.42	2.62	-5.109
5760.064528	-1.11	2.51	-5.041
5760.958645	3.39	2.56	-5.041
5761.876117	5.12	2.48	-5.048

TABLE 4 — *Continued*

BJD – 2450000	Radial Velocity (m s ⁻¹)	Uncertainty (m s ⁻¹)	R' _{HK}
5762.912248	6.33	2.42	-5.041
5763.870182	5.01	2.45	-5.034
5791.871645	-1.99	2.47	-5.048
5793.996566	-2.77	2.55	-5.070
5795.012741	-12.15	3.13	-5.085
5796.793068	1.87	2.42	-5.021
5797.853511	5.06	2.41	-5.041
5798.773192	1.43	2.37	-5.048
5807.741761	2.21	2.55	-5.070
5808.840217	-5.33	2.61	-5.028
5809.749926	2.75	2.45	-5.048
5810.749216	4.68	2.42	-5.041
5811.865319	6.67	2.40	-5.041
5814.757203	2.23	2.47	-5.048
6109.979987	4.30	2.46	-5.055
6110.856162	0.99	2.59	-5.055
6111.867315	0.32	2.56	-5.055
6112.888295	4.29	2.49	-5.055
6113.851194	1.74	2.65	-5.117
6114.900100	3.51	2.56	-5.034
6115.897107	7.42	2.53	-5.048
6173.889875	-1.85	2.47	-5.055
6177.929359	-7.30	3.07	-5.048
6178.805849	1.60	2.44	-5.048
6209.725678	-0.93	2.55	-5.063

TABLE 5
RADIAL VELOCITIES FOR KOI-69

BJD – 2450000	Radial Velocity (m s ⁻¹)	Uncertainty (m s ⁻¹)	R' _{HK}
5044.067242	-12.90	2.73	-4.983
5045.039518	-19.29	2.85	-4.972
5074.010142	-11.01	2.44	-4.972
5075.008297	-13.22	2.45	-4.983
5075.985757	-11.06	2.43	-4.972
5077.017498	-14.77	2.48	-4.994
5078.016299	-16.70	2.47	-4.972
5078.943562	-14.89	2.44	-4.972
5079.935707	-13.23	2.39	-4.972
5080.753597	-7.78	2.38	-4.972
5080.792010	-9.66	2.44	-4.966
5081.769317	-8.65	2.59	-4.966
5081.776018	-10.64	2.71	-4.977
5082.741078	-6.95	2.47	-4.966
5083.753822	-6.48	2.43	-4.966
5084.751762	-5.96	2.39	-4.961
5373.033115	-2.16	2.41	-4.977
5377.938646	-2.78	2.38	-4.966
5696.963643	12.83	2.57	-4.977
5697.938827	9.94	2.42	-4.977
5698.937161	7.95	2.45	-4.972
5700.017234	14.34	2.39	-4.972
5723.039490	7.80	2.47	-4.977
5759.820878	6.04	2.51	-4.983
5760.863548	12.19	2.43	-4.972
5762.926837	6.74	2.40	-4.983
5768.842459	11.17	2.44	-4.983
5807.767167	16.08	2.47	-5.005
6110.033656	19.10	2.50	-4.972
6115.033413	22.14	2.45	-4.977
6148.820507	28.18	2.56	-4.972
6174.837273	22.79	2.36	-4.972

TABLE 6
RADIAL VELOCITIES FOR KOI-82

BJD – 2450000	Radial Velocity (m s ⁻¹)	Uncertainty (m s ⁻¹)	R'_{HK}
5312.078536	-5.59	2.39	-4.586
5373.830100	-0.92	2.40	-4.618
5402.922434	-4.08	2.31	-4.658
5414.824561	2.83	2.30	-4.625
5428.776770	-0.60	2.33	-4.644
5431.766490	-4.13	2.30	-4.644
5439.774551	0.28	2.27	-4.484
5440.884419	3.01	2.31	-4.667
5752.082671	-1.28	2.41	-4.573
5752.923634	-0.57	2.54	-4.594
5752.940613	-0.33	2.60	-4.587
5759.888028	1.25	2.33	-4.586
5760.825411	-2.10	2.32	-4.601
5787.782634	7.80	2.32	-4.598
5788.796321	8.08	2.32	-4.604
5794.989286	-5.42	2.47	-4.561
5795.870970	-1.38	2.32	-4.563
5809.768343	-1.66	2.31	-4.633
5810.766141	-0.21	2.29	-4.636
5811.846830	0.54	2.28	-4.617
5814.775163	2.23	2.31	-4.594
6110.049088	2.21	2.41	-4.626
6110.877659	1.30	2.33	-4.604
6111.885201	-1.67	2.32	-4.603
6112.910601	4.16	2.36	-4.581
6113.892412	4.91	2.38	-4.610
6115.097881	3.01	2.60	-4.624
6133.877339	-3.08	2.34	-4.620
6134.913293	-9.37	2.37	-4.624
6141.045454	1.27	2.40	-4.630
6144.835181	0.78	2.37	-4.636
6145.835817	3.49	2.27	-4.630
6166.822306	-10.67	2.46	-4.671
6172.780889	-1.06	2.42	-4.641
6208.797480	9.06	2.41	-4.580

TABLE 7
RADIAL VELOCITIES FOR KOI-104

BJD – 2450000	Radial Velocity (m s ⁻¹)	Uncertainty (m s ⁻¹)	R'_{HK}
5377.841906	-65.50	2.75	-4.638
5378.934287	-54.36	2.96	-4.616
5379.961656	-66.73	3.07	-4.701
5433.761242	-11.72	2.60	-4.685
5434.927884	-16.61	2.80	-4.656
5438.852111	1.55	3.20	-4.857
5438.881509	9.99	2.98	-4.756
5465.829854	28.56	3.26	-4.424
5521.729851	56.90	3.14	-4.966
5697.049110	99.24	2.93	-4.601
5698.037021	80.44	2.80	-4.686
5699.034699	97.68	3.26	-4.671
5699.997226	93.70	2.79	-4.560
5723.980007	85.68	2.97	-4.577
5733.960824	77.25	2.90	-4.567
5734.920790	82.12	2.76	-4.591
5738.849308	77.70	2.87	-4.471
5759.912267	66.97	3.05	-4.873
5760.882081	58.78	2.79	-4.654
5789.922472	43.45	2.89	-4.946
5790.939908	28.25	2.81	-4.635
5798.969403	26.80	2.79	-4.600
5809.956676	33.38	2.82	-4.730
5810.845889	26.81	2.67	-4.586
6077.025088	-285.15	2.79	-4.576
6115.875911	-184.39	2.73	-4.547
6135.066858	-166.59	3.17	-4.581
6147.946195	-136.85	3.03	-4.585
6176.762087	-90.03	2.85	-4.573

TABLE 7 — *Continued*

BJD – 2450000	Radial Velocity (m s ⁻¹)	Uncertainty (m s ⁻¹)	R'_{HK}
5073.968560	-4.76	6.71	-4.999

TABLE 8
RADIAL VELOCITIES FOR KOI-108

BJD – 2450000	Radial Velocity (m s ⁻¹)	Uncertainty (m s ⁻¹)	R'_{HK}
5074.938879	-12.07	6.64	-4.999
5077.005648	-7.20	7.06	-5.054
5079.991586	-2.46	6.66	-5.054
5080.982908	-3.87	6.66	-4.836
5082.902081	5.64	6.67	-4.999
5084.913610	5.06	6.63	-4.986
5134.787135	-6.19	3.33	-5.012
5131.104615	-2.59	2.84	-5.006
5321.997726	7.95	2.89	-5.006
5377.875117	-0.31	2.90	-5.006
5378.838317	-0.52	3.00	-5.026
5402.987989	4.71	2.91	-5.026
5411.034645	0.12	2.90	-5.006
5425.916614	-3.17	2.93	-5.012
5433.844314	4.34	2.78	-4.986
5440.822218	-2.76	2.70	-5.006
5794.030378	3.36	3.14	-5.046
5809.900772	-4.82	2.70	-4.999

TABLE 9
RADIAL VELOCITIES FOR KOI-116

BJD – 2450000	Radial Velocity (m s ⁻¹)	Uncertainty (m s ⁻¹)	R'_{HK}
5133.897351	9.29	4.06	-4.783
5373.958416	6.52	3.03	-4.948
5379.001449	1.61	3.29	-4.966
5380.025601	-7.92	2.98	-4.960
5433.918565	-3.61	3.02	-4.920
5439.876430	-2.17	3.07	-4.960
5441.023521	-4.05	3.23	-4.978
5734.085379	0.06	3.14	-4.960
5752.894726	6.75	3.20	-4.960
5759.992485	-0.07	3.27	-4.978
6111.910098	2.89	3.16	-4.948
6113.987149	1.15	3.32	-4.990
6115.949113	4.10	3.11	-4.960
6133.944504	5.29	3.24	-4.966
6138.981896	-5.09	3.04	-4.960
6144.975318	4.26	3.35	-4.954
6145.858923	4.94	3.06	-4.954
6147.834465	-0.29	3.30	-4.960
6151.043480	-4.99	3.19	-4.948
6152.041410	-14.82	3.46	-5.003
6153.049571	-3.34	3.56	-5.074
6166.790534	-4.91	3.15	-4.948
6173.825374	0.14	3.12	-4.966
6178.784524	-8.28	3.07	-4.966
6207.805559	8.16	3.34	-4.948

TABLE 10
RADIAL VELOCITIES FOR KOI-122

BJD – 2450000	Radial Velocity (m s ⁻¹)	Uncertainty (m s ⁻¹)	R'_{HK}
5073.994534	-2.19	6.81	-5.002

TABLE 10 — *Continued*

BJD – 2450000	Radial Velocity (m s ⁻¹)	Uncertainty (m s ⁻¹)	R'_{HK}
5075.946624	3.90	6.80	-4.991
5076.769704	-0.63	6.72	-4.974
5079.919778	2.64	6.81	-5.014
5080.930639	-8.02	6.81	-5.014
5081.929904	-4.97	6.79	-4.996
5082.942536	-7.91	6.78	-5.002
5083.865170	-3.44	6.76	-5.014
5084.842177	-3.48	6.71	-4.968
5131.064246	-9.40	2.50	-4.991
5318.098919	4.62	2.67	-4.991
5377.020314	8.40	2.53	-4.985
5400.944047	-0.41	2.80	-5.008
5405.939014	3.36	2.57	-4.996
5411.002552	5.55	2.49	-4.974
5411.896640	11.00	2.65	-4.979
5427.839158	-2.81	2.59	-5.008
5428.800667	0.84	2.49	-4.996
5434.798117	-2.08	2.44	-4.996
5439.834670	-2.72	2.42	-5.008
5486.806230	-2.87	2.86	-5.026
5697.081519	4.67	2.68	-5.039
5698.069331	2.09	2.60	-5.033
5699.066159	-1.67	2.63	-5.045
5700.096380	1.79	2.65	-5.033
5738.817453	-3.66	2.67	-5.014
5791.763490	4.17	2.48	-4.963
5797.013255	1.95	2.77	-5.045
5809.927350	-2.30	2.47	-5.014
5814.898557	3.18	2.52	-5.026
6152.011007	1.33	2.64	-4.985

TABLE 11
RADIAL VELOCITIES FOR KOI-123

BJD – 2450000	Radial Velocity (m s ⁻¹)	Uncertainty (m s ⁻¹)	R'_{HK}
5074.992468	7.66	7.12	-5.014
5075.969200	6.70	7.11	-5.007
5076.849395	9.48	7.05	-4.994
5080.956368	-10.35	7.11	-5.021
5082.920913	6.64	7.13	-4.994
5083.964085	5.57	7.21	-5.000
5084.949365	7.55	7.11	-4.994
5170.755814	-7.51	3.49	-5.000
5314.059619	-6.09	2.80	-5.007
5321.104302	-1.74	2.85	-5.021
5343.073868	-10.93	2.97	-5.028
5344.098191	-6.20	3.10	-5.028
5372.963165	-0.29	3.02	-5.007
5378.870526	-0.34	2.97	-5.021
6166.844942	-5.35	2.91	-4.994

TABLE 12
RADIAL VELOCITIES FOR KOI-148,KEPLER-48

BJD – 2450000	Radial Velocity (m s ⁻¹)	Uncertainty (m s ⁻¹)	R'_{HK}
5074.026507	-1.31	12.26	-4.879
5075.032090	-1.48	12.21	-4.859
5076.799857	-2.81	12.08	-4.873
5077.955169	1.14	12.19	-4.865
5077.975134	-8.53	12.17	-4.879
5312.106882	38.33	3.16	-4.873
5377.908091	18.04	2.79	-4.848
5381.054562	31.24	2.83	-4.876
5407.078286	32.63	2.97	-4.820

TABLE 12 — *Continued*

BJD – 2450000	Radial Velocity (m s ⁻¹)	Uncertainty (m s ⁻¹)	R'_{HK}
5414.941524	18.40	2.73	-4.813
5434.897144	6.44	2.55	-4.840
5438.783842	24.56	2.77	-4.810
5438.811770	25.55	2.92	-4.813
5787.843659	-55.28	2.86	-4.818
5793.775124	-59.11	2.85	-4.833
5796.821157	-48.12	2.63	-4.810
5797.947000	-49.70	2.66	-4.828
5799.028618	-53.15	2.90	-4.818
5807.829071	-49.37	2.92	-4.835
5810.977776	-48.64	2.89	-4.833
5811.953784	-53.35	2.60	-4.843
5814.865587	-52.15	2.75	-4.843
6115.912076	16.62	3.13	-4.791
6141.025441	12.07	3.22	-4.840
6145.890599	36.27	3.17	-4.851
6164.829375	48.32	3.11	-4.825
6173.848569	37.85	2.91	-4.848
6208.750960	33.64	3.07	-4.810

TABLE 13
RADIAL VELOCITIES FOR KOI-153

BJD – 2450000	Radial Velocity (m s ⁻¹)	Uncertainty (m s ⁻¹)	R'_{HK}
5314.091538	-7.08	2.97	-5.018
5373.884706	-5.21	3.08	-5.060
5376.896191	-9.70	3.07	-5.175
5378.901697	-4.04	3.05	-5.028
5381.020292	-8.27	3.16	-5.133
5428.828387	-6.66	3.00	-5.084
5435.804603	10.57	3.16	-5.257
5437.846080	-7.31	3.55	-4.945
5437.882874	-10.84	3.39	-5.098
5697.110582	20.09	3.43	-4.815
5698.004879	17.39	3.05	-4.830
5699.002293	4.43	3.27	-4.731
5700.066664	15.06	3.20	-4.949
5735.002572	-3.16	3.13	-5.084
5752.830942	-4.22	3.23	-5.013
5761.058504	8.01	2.99	-5.065
5789.952972	-4.86	3.20	-5.023
5792.017851	-0.80	2.95	-5.052
5796.872421	11.64	3.06	-5.076
5811.816797	7.82	3.02	-5.079
6110.983363	-5.14	3.32	-5.149
6112.973425	-15.97	3.34	-5.098
6144.037413	-0.53	3.27	-5.152
6147.014037	-4.98	3.29	-4.965

TABLE 14
RADIAL VELOCITIES FOR KOI-244,KEPLER-25

BJD – 2450000	Radial Velocity (m s ⁻¹)	Uncertainty (m s ⁻¹)	R'_{HK}
5367.102834	-7.68	4.28	-5.183
5376.963016	3.26	3.89	-5.195
5377.950450	-2.78	3.73	-5.172
5433.941912	14.54	4.22	-5.258
5696.949358	12.64	3.97	-5.207
5697.952294	2.17	4.29	-5.219
5698.948910	-4.71	3.98	-5.219
5700.027670	10.59	4.03	-5.207
5734.052698	-1.17	3.67	-5.195
5735.986640	-13.52	3.84	-5.207
5739.049628	-2.81	4.63	-5.195

TABLE 14 — *Continued*

BJD – 2450000	Radial Velocity (m s ⁻¹)	Uncertainty (m s ⁻¹)	R'_{HK}
5751.935799	-16.11	3.97	-5.195
5752.793676	-18.65	3.70	-5.183
5759.966063	5.85	3.59	-5.195
5760.809525	-4.73	3.78	-5.183
5761.102651	-4.29	3.67	-5.183
5762.100290	5.63	4.10	-5.207
5762.110117	1.44	3.86	-5.219
5762.118219	-13.47	5.07	-5.161
5762.891494	-3.59	3.28	-5.207
5763.840742	-8.05	3.75	-5.195
5768.852800	-8.83	3.90	-5.219
5769.943894	8.72	4.09	-6.789
5782.065146	-6.14	4.58	-5.301
5787.762931	-0.92	4.28	-5.232
5788.938209	-5.17	3.93	-5.219
5789.798064	1.01	4.21	-5.245
5789.804939	3.83	4.57	-5.245
5790.755601	-3.04	3.81	-5.232
5791.933168	-0.39	3.94	-5.245
5792.767270	3.70	3.76	-5.245
5794.925518	17.95	4.26	-5.272
5796.893200	16.45	3.96	-5.245
5798.759251	3.79	3.96	-5.258
5806.789430	14.91	3.97	-5.272
5808.797455	20.19	3.80	-5.258
5810.734832	7.34	4.10	-5.258
5814.927264	15.10	4.13	-5.272
5903.699358	10.63	4.06	-5.258
6079.872621	-1.44	4.36	-5.333
6080.109747	4.40	4.07	-5.207
6114.852234	3.40	4.35	-5.161
6134.929891	-11.23	3.95	-5.219
6139.028357	-3.47	4.17	-5.207
6145.944136	-0.85	4.72	-5.207
6147.806840	-5.67	4.06	-5.219
6148.839914	-6.37	4.43	-5.232
6152.962700	16.32	4.35	-5.245
6163.794337	22.99	4.15	-5.232
6194.822303	6.48	4.58	-5.258
5803.3364	10.11	16.00	0
5809.5034	25.41	19.00	0
5810.4814	-10.69	25.00	0
5811.3940	-4.09	12.00	0
5828.2935	-5.79	10.00	0
5855.2837	-9.89	19.00	0
5857.2627	-15.39	17.00	0
5877.6963	4.21	16.00	0
5878.2544	1.01	16.00	0
5879.2661	-14.69	16.00	0
5882.3022	13.81	16.00	0
5883.2764	20.81	15.00	0

TABLE 15
RADIAL VELOCITIES FOR KOI-245,KEPLER-37

BJD – 2450000	Radial Velocity (m s ⁻¹)	Uncertainty (m s ⁻¹)	R'_{HK}
5313.086400	3.47	2.46	-4.972
5319.116525	1.15	2.61	-4.980
5376.949842	0.14	2.45	-5.008
5396.019973	2.18	2.53	-4.990
5400.968136	8.98	2.39	-5.116
5425.934247	1.79	2.27	-5.023
5433.932956	-0.32	2.28	-5.013
5723.052494	-1.50	2.46	-4.959
5723.100134	-1.99	2.41	-4.954
5768.862142	3.46	2.29	-5.013
5769.817056	1.64	2.35	-5.013
5770.858798	2.72	2.36	-4.976
5782.046825	-1.33	2.38	-5.038
5782.900841	-1.14	2.38	-5.003

TABLE 15 — *Continued*

BJD – 2450000	Radial Velocity (m s ⁻¹)	Uncertainty (m s ⁻¹)	R'_{HK}
5787.754366	-4.12	2.34	-5.013
5788.994542	-5.71	2.40	-5.028
5789.882547	0.50	2.40	-5.023
5790.747253	-4.64	2.34	-5.023
5791.748658	-2.62	2.39	-5.023
5792.759449	-0.45	2.34	-5.013
5794.938166	-0.70	2.37	-5.028
5795.758577	-2.35	2.47	-5.043
5796.781113	-3.02	2.38	-5.003
5797.783521	-3.02	2.32	-5.003
5798.751068	-10.90	2.40	-4.999
6098.081597	3.20	2.52	-4.938
6115.057869	-0.46	2.46	-4.976
6148.956270	2.18	2.29	-4.959
6163.786571	3.90	2.38	-4.918
6164.745854	5.34	2.36	-4.907
6166.810249	-2.70	2.46	-4.910
6168.007627	2.90	2.50	-4.938
6174.952383	0.01	2.40	-4.907

TABLE 16
RADIAL VELOCITIES FOR KOI-246,KEPLER-68

BJD – 2450000	Radial Velocity (m s ⁻¹)	Uncertainty (m s ⁻¹)	R'_{HK}
5313.081849	-5.12	2.49	-5.144
5319.109464	-9.10	2.62	-5.190
5322.050550	-11.70	2.35	-5.162
5372.982740	-10.23	2.31	-5.162
5377.929044	-9.43	2.34	-5.153
5381.000211	-16.88	2.39	-5.162
5396.962763	-14.13	2.49	-5.144
5412.922534	-18.00	2.33	-5.171
5426.913366	-15.73	2.35	-5.119
5431.784060	-9.91	2.33	-5.144
5434.870088	-22.45	2.32	-5.111
5434.876488	-23.61	2.32	-5.111
5435.931255	-18.79	2.40	-5.162
5436.968463	-14.77	2.61	-5.190
5436.974551	-19.87	2.62	-5.230
5437.940359	-14.12	2.41	-5.119
5437.949792	-13.75	2.36	-5.103
5438.991420	-15.27	2.38	-5.153
5439.002623	-14.98	2.44	-5.136
5439.923524	-18.57	2.34	-5.111
5439.931556	-20.18	2.38	-5.127
5440.971227	-17.20	2.35	-5.119
5440.980301	-21.42	2.36	-5.136
5455.809962	-21.93	2.35	-5.080
5490.829645	-17.44	2.43	-5.088
5672.026425	18.28	2.28	-5.162
5672.998402	14.81	2.36	-5.171
5673.995774	19.03	2.41	-5.153
5696.973926	21.92	2.36	-5.144
5697.964434	24.04	2.47	-5.144
5698.962303	17.42	2.37	-5.153
5722.994969	22.72	2.43	-5.171
5724.033632	27.40	2.48	-5.171
5728.900947	24.01	2.48	-5.299
5734.064071	25.48	2.40	-5.171
5734.951047	26.17	2.39	-5.162
5735.974739	24.85	2.36	-5.162
5739.034181	24.50	2.45	-5.171
5751.796956	18.86	2.43	-5.162
5752.104703	18.05	2.40	-5.200
5752.778961	15.95	2.43	-5.162
5759.975172	19.01	2.40	-5.153
5761.076467	22.15	2.31	-5.153
5761.841845	15.94	2.35	-5.200
5763.032747	19.27	2.35	-5.220
5763.851041	15.29	2.36	-5.153

TABLE 16 — *Continued*

BJD – 2450000	Radial Velocity (m s ⁻¹)	Uncertainty (m s ⁻¹)	R'_{HK}
5782.907862	15.64	2.40	-5.171
5795.024254	7.62	2.52	-5.153
5814.735957	13.34	2.34	-5.095
6077.045184	-15.79	2.40	-5.181
6098.093799	-11.72	2.45	-5.171
6098.828990	-12.40	2.43	-5.144
6102.007905	-5.81	2.36	-5.162
6114.871876	-15.18	2.38	-5.153
6145.875413	-9.63	2.46	-5.136
6148.928774	-3.46	2.33	-5.111
6151.060872	-10.72	2.41	-5.127
6153.983044	-8.76	2.36	-5.095
6174.826576	-0.72	2.44	-5.088
6345.155209	17.66	2.43	-5.162

TABLE 17
RADIAL VELOCITIES FOR KOI-261

BJD – 2450000	Radial Velocity (m s ⁻¹)	Uncertainty (m s ⁻¹)	R'_{HK}
5405.030168	2.55	2.47	-4.755
5405.889943	2.32	2.34	-4.745
5413.976523	0.62	2.48	-4.739
5431.794557	3.78	2.30	-4.765
5436.986914	5.95	2.35	-4.793
5437.960924	3.00	2.26	-4.765
5437.971745	7.19	2.30	-4.762
5438.829298	3.66	2.31	-4.758
5439.855631	-3.95	2.31	-4.758
5455.819605	2.30	2.38	-4.758
5486.833994	1.19	2.42	-4.775
5542.714646	0.82	2.46	-4.769
5544.703444	-5.41	2.55	-4.576
5723.092577	0.86	2.58	-4.663
5787.903358	-3.39	2.50	-4.758
5795.035974	-4.74	2.41	-4.755
5795.835975	-3.78	2.57	-4.775
6099.033843	5.65	2.59	-4.708
6111.925286	-12.19	2.59	-4.742
6145.907599	-6.48	2.52	-4.782
6148.981644	5.12	2.64	-4.779
6152.067220	-1.91	2.53	-4.797
6163.805762	2.65	2.43	-4.782
6164.846196	2.79	2.45	-4.786
6175.877276	-4.53	2.47	-4.797
6176.894658	-8.24	2.49	-4.786

TABLE 18
RADIAL VELOCITIES FOR KOI-283

BJD – 2450000	Radial Velocity (m s ⁻¹)	Uncertainty (m s ⁻¹)	R'_{HK}
5433.868391	5.08	2.30	-4.824
5434.854201	4.86	2.31	-4.828
5440.950440	-2.54	2.37	-4.860
5471.813137	0.10	2.56	-4.856
5490.808418	-0.81	2.63	-4.856
5522.775891	-6.82	2.61	-4.864
5542.700150	5.54	2.67	-4.886
5724.012916	1.75	2.42	-4.928
5734.972723	-3.99	2.43	-4.904
5736.009887	-4.90	2.46	-4.900
5788.893783	7.50	2.58	-4.860
5795.941507	3.92	2.39	-4.844
6101.059779	1.30	2.50	-4.895
6110.960155	-0.31	2.58	-4.975
6115.924507	6.65	2.58	-4.891

TABLE 18 — *Continued*

BJD – 2450000	Radial Velocity (m s ⁻¹)	Uncertainty (m s ⁻¹)	R'_{HK}
6140.911995	-3.73	2.61	-4.895
6164.891469	-11.47	2.52	-4.975
6166.889764	-13.88	2.53	-4.928
6173.867998	10.24	2.46	-4.856
6175.860356	2.27	2.55	-4.840

TABLE 19
RADIAL VELOCITIES FOR KOI-292

BJD – 2450000	Radial Velocity (m s ⁻¹)	Uncertainty (m s ⁻¹)	R'_{HK}
5377.974537	2.05	3.02	-5.104
5405.869250	3.50	2.94	-5.120
5407.043984	4.70	3.08	-5.136
5410.952610	3.43	2.90	-5.120
5411.803603	8.88	2.95	-5.112
5412.865682	4.95	3.11	-5.128
5425.822700	3.24	3.03	-5.088
5426.931969	2.33	2.87	-5.088
5751.875319	1.94	3.30	-5.096
5782.969047	2.99	3.00	-5.120
5788.957075	-8.30	3.19	-5.096
5790.834867	0.86	3.14	-4.906
5810.874922	8.26	3.04	-5.096
6103.079865	-4.15	3.45	-5.154
6112.853787	-2.20	3.28	-5.136
6144.947724	5.39	3.18	-5.145
6145.924744	-5.74	3.05	-5.136
6151.014731	-4.42	3.03	-5.120
6153.016068	-15.95	3.28	***e2147
6166.911312	-7.58	3.21	-5.104

TABLE 20
RADIAL VELOCITIES FOR KOI-299

BJD – 2450000	Radial Velocity (m s ⁻¹)	Uncertainty (m s ⁻¹)	R'_{HK}
5404.011500	9.78	2.76	-4.788
5406.943814	5.91	2.90	-4.835
5407.871779	-1.02	2.75	-4.794
5411.927391	-1.76	2.74	-4.846
5413.947119	-9.22	2.91	-4.876
5414.852128	-12.73	2.66	-4.853
5433.792757	-5.53	2.61	-4.811
5434.771547	0.81	2.61	-4.831
5437.918288	3.25	2.92	-4.842
5440.852924	-6.40	2.67	-4.849
5735.034887	6.12	2.81	-4.748
5751.843073	5.10	2.87	-4.797
5760.040755	4.36	2.69	-4.785
5760.909806	0.13	2.67	-4.801
5796.002983	-3.74	3.22	-4.860
5797.816289	5.21	2.65	-4.831
5807.988113	-3.40	3.20	-4.320
5810.917683	-0.34	2.67	-4.811
5811.762281	-10.68	2.68	-4.804
6113.004738	8.75	2.69	-4.782
6114.053151	7.21	3.26	-4.966
6208.773499	-3.19	2.78	-4.814

TABLE 21
RADIAL VELOCITIES FOR KOI-305

BJD – 2450000	Radial Velocity (m s ⁻¹)	Uncertainty (m s ⁻¹)	R'_{HK}
5404.043451	3.25	2.69	-4.414
5405.840133	3.15	2.47	-4.610
5406.910870	4.38	2.58	-4.779
5410.923078	-4.28	2.49	-4.676
5736.069898	4.67	2.69	-4.712
5751.907376	-7.05	2.59	-4.624
5760.980986	3.95	2.55	-4.842
5790.878287	0.93	2.57	-4.648
5792.968210	1.01	2.57	-4.663
5795.056867	2.20	2.90	-4.644
5797.876148	-1.21	2.52	-4.628
6102.027398	-7.74	2.62	-4.590
6112.943513	3.17	2.97	-4.666
6116.071830	-5.38	2.58	-4.591
6140.890738	4.76	2.59	-4.579
6145.029741	1.35	2.72	-4.589
6147.892714	-7.78	2.50	-4.631
6163.884725	9.32	2.70	-4.531
6172.829726	-1.39	2.69	-4.593
6192.868451	-10.73	2.57	-4.573
6195.854351	0.27	2.51	-4.559

TABLE 22
RADIAL VELOCITIES FOR KOI-321

BJD – 2450000	Radial Velocity (m s ⁻¹)	Uncertainty (m s ⁻¹)	R'_{HK}
5379.033747	3.62	2.57	-4.945
5380.109093	-5.92	2.66	-4.980
5403.979414	3.99	2.68	-5.007
5411.834541	-6.94	2.54	-5.029
5412.898763	2.87	2.63	-5.012
5434.825372	-0.53	2.52	-5.085
5435.909173	-1.98	2.82	-5.085
5751.813315	-4.74	2.76	-5.001
5752.852880	-0.94	2.96	-4.996
5752.868470	0.29	2.73	-4.975
5759.839971	6.17	2.66	-4.950
5760.936394	-4.23	2.58	-4.965
5769.859474	6.60	2.56	-5.041
5788.839547	-1.72	2.59	-5.059
5789.984420	1.17	2.63	-5.066
5810.791430	-1.37	2.51	-5.078
5811.920824	-11.11	2.59	-5.126
5843.811883	-7.55	3.01	-5.148
6073.925432	-1.96	3.05	-4.960
6075.917333	0.60	3.09	-5.001
6076.992302	3.17	2.75	-4.960
6098.855454	-3.04	2.44	-4.918
6099.985448	0.10	2.62	-4.941
6101.029734	-1.44	2.59	-4.950
6101.872764	1.69	2.61	-4.936
6103.050119	4.15	2.68	-4.941
6104.059437	1.79	2.72	-4.985
6105.064136	10.72	2.80	-4.980
6109.955028	-7.50	2.49	-4.970
6111.022468	1.20	2.73	-4.965
6111.941178	1.24	2.53	-4.905
6115.999606	4.75	2.51	-5.001
6133.832918	8.11	2.57	-5.035
6134.888536	-1.09	2.63	-5.035
6138.008915	0.39	2.66	-5.035
6140.863836	-1.40	2.69	-5.041
6163.843324	-0.84	2.72	-5.085
6164.774988	4.40	2.57	-5.085
6166.003960	-1.82	2.71	-5.059
6171.983117	-1.63	2.94	-5.085
6177.836688	-6.64	2.67	-5.078
6179.763596	-2.02	2.56	-5.119

TABLE 23 — *Continued*

BJD – 2450000	Radial Velocity (m s ⁻¹)	Uncertainty (m s ⁻¹)	R'_{HK}
5697.018217	34.02	2.91	-5.038
5698.101339	36.49	2.96	-5.049
5699.097179	34.25	3.00	-4.969
5736.037333	26.71	3.03	-5.108
5752.051431	27.67	2.81	-5.072
5760.015457	19.32	2.69	-5.084
5760.776641	20.94	2.75	-5.090
5768.875006	18.75	2.68	-5.141
5769.798374	20.24	2.80	-5.176
5770.841452	21.93	2.76	-5.128
5790.914061	13.69	2.83	-5.078
5791.889570	17.63	2.69	-5.090
5792.876920	15.57	2.69	-5.072
5797.899896	4.69	2.82	-5.102
6133.912806	-144.55	3.04	-5.066
6172.849950	-168.36	2.95	-5.044

TABLE 24
RADIAL VELOCITIES FOR KOI-1612

BJD – 2450000	Radial Velocity (m s ⁻¹)	Uncertainty (m s ⁻¹)	R'_{HK}
5698.087742	2.49	2.50	-4.992
5699.127102	0.56	2.49	-4.972
5700.112050	4.47	2.48	-5.006
5700.943498	1.12	2.50	-5.013
5703.924719	1.10	2.47	-5.035
5704.886679	8.90	2.53	-5.013
5706.894189	-3.62	2.39	-5.028
5707.890606	5.94	2.47	-5.051
5723.104987	-1.35	2.43	-5.020
5724.114372	-5.66	2.54	-5.028
5726.075420	0.17	2.36	-5.067
5727.023738	-1.65	2.36	-5.051
5728.890788	-1.36	2.51	-5.178
5734.956730	2.31	2.45	-5.051
5736.051585	-7.29	2.52	-5.051
5739.066041	-3.17	2.55	-5.043
5739.075902	-1.94	2.59	-5.059
5751.924655	-2.95	2.50	-5.059
5752.784580	-7.19	2.53	-5.059
5760.075266	2.04	2.57	-5.035
5761.082387	2.43	2.56	-5.059
5762.898826	-0.86	2.54	-5.075
5763.857299	-3.11	2.56	-5.075
6000.139475	4.20	2.43	-5.043
6019.033769	4.40	2.46	-5.020
6020.045352	4.72	2.52	-5.013
6028.005633	2.87	2.48	-4.985
6073.886610	7.36	2.51	-5.051
6075.968379	-4.72	2.40	-5.075
6076.937976	-0.86	2.49	-5.059
6098.068823	2.23	2.53	-5.067
6115.023931	-5.82	2.70	-5.075
6144.877583	-1.98	2.95	-5.101
6145.901440	2.03	2.77	-5.092
6146.966014	-1.61	2.64	-5.101
6147.817037	-4.03	2.64	-5.119
6148.853184	-1.97	2.55	-5.110
6174.848128	-2.30	2.67	-5.138

TABLE 25 — *Continued*

BJD – 2450000	Radial Velocity (m s ⁻¹)	Uncertainty (m s ⁻¹)	R'_{HK}
---------------	---	-------------------------------------	------------------

TABLE 25
RADIAL VELOCITIES FOR KOI-1925

BJD – 2450000	Radial Velocity (m s ⁻¹)	Uncertainty (m s ⁻¹)	R'_{HK}
6000.146032	-2.45	2.20	-5.061
6019.055308	-6.34	2.29	-5.045
6020.099174	1.57	2.23	-5.024
6028.041949	1.66	2.20	-5.029
6073.949745	-2.48	2.23	-5.019
6075.094428	-1.92	2.25	-5.024
6075.977029	-1.84	2.23	-5.024
6076.946404	0.74	2.27	-5.014
6098.057089	-5.45	2.30	-5.096
6098.838256	-0.55	2.20	-5.061
6099.909720	-1.19	2.21	-5.061
6100.930048	-0.06	2.16	-5.061
6101.982553	0.93	2.20	-5.056
6102.956964	-1.21	2.21	-5.050
6103.963911	-0.88	2.22	-5.050
6104.981934	2.73	2.18	-5.061
6113.020955	2.76	2.21	-5.034
6113.831179	1.20	2.23	-5.045
6114.839891	1.39	2.24	-5.029
6115.860558	6.37	2.21	-5.045
6133.923304	0.39	2.31	-5.061
6134.962073	-5.06	2.39	-5.078
6138.035933	3.13	2.32	-5.067
6148.866212	-3.70	2.30	-5.056
6174.857241	5.59	2.36	-5.045

REFERENCES

- Adams, E. R., Ciardi, D. R., Dupree, A. K., Gautier, III, T. N., Kulesa, C., & McCarthy, D. 2012, AJ, 144, 42
- Albrecht, S., Winn, J. N., Marcy, G. W., Howard, A. W., Isaacson, H., & Johnson, J. A. 2013, ArXiv e-prints
- Argabright, V. S., et al. 2008, in Society of Photo-Optical Instrumentation Engineers (SPIE) Conference Series, Vol. 7010, Society of Photo-Optical Instrumentation Engineers (SPIE) Conference Series
- Ballard, S., et al. 2013, ArXiv e-prints
- Barclay, T., et al. 2013, Nature, 494, 452
- Batalha, N. M., et al. 2010, ApJ, 713, L103
- . 2011, ApJ, 729, 27
- . 2013, ApJS, 204, 24
- Bonfils, X., et al. 2012, A&A, 546, A27
- Borucki, W. J., et al. 2010, Science, 327, 977
- . 2011, ApJ, 736, 19
- Borucki, W. J., et al. 2013, Science
- Bruntt, H., et al. 2012, MNRAS, 423, 122
- Bryson, S. T., et al. 2013, ArXiv e-prints
- Buchhave, L. A., et al. 2012, Nature, 486, 375
- Caldwell, D. A., et al. 2010, ApJ, 713, L92
- Charbonneau, D., et al. 2009, Nature, 462, 891
- Chiang, E., & Laughlin, G. 2012, ArXiv e-prints
- Chubak, C., Marcy, G., Fischer, D. A., Howard, A. W., Isaacson, H., Johnson, J. A., & Wright, J. T. 2012, ArXiv e-prints
- Claret, A., & Bloemen, S. 2011, A&A, 529, A75
- Cochran, W. D., et al. 2011, ApJS, 197, 7
- Demarque, P., Woo, J., Kim, Y., & Yi, S. K. 2004, ApJS, 155, 667
- Demory, B.-O., et al. 2011, A&A, 533, A114
- . 2013, ArXiv e-prints
- Désert, J.-M., Charbonneau, D., Fressin, F., & Torres, G. 2012, in American Astronomical Society Meeting Abstracts, Vol. 219, American Astronomical Society Meeting Abstracts #219, 414.02
- Fabrycky, D. C., et al. 2012, ArXiv e-prints
- Figueira, P., Pont, F., Mordasini, C., Alibert, Y., Georgy, C., & Benz, W. 2009, A&A, 493, 671
- Fischer, D. A., & Valenti, J. 2005, ApJ, 622, 1102
- Fortney, J. J., Marley, M. S., & Barnes, J. W. 2007, ApJ, 659, 1661
- Fressin, F., et al. 2013, ApJ, 766, 81
- Gautier, III, T. N., et al. 2010, ArXiv e-prints
- Gilliland, R. L., et al. 2013, ApJ, 766, 40
- Gillon, M., et al. 2007, A&A, 472, L13
- Goldreich, P., Lithwick, Y., & Sari, R. 2004, ARA&A, 42, 549
- Hartman, J. D., et al. 2011, ApJ, 728, 138
- Hayward, T. L., Brandl, B., Pirger, B., Blacken, C., Gull, G. E., Schoenwald, J., & Houck, J. R. 2001, PASP, 113, 105
- Horch, E. P., Veillette, D. R., Baena Gallé, R., Shah, S. C., O’Rielly, G. V., & van Altena, W. F. 2009, AJ, 137, 5057
- Howard, A., Marcy, G., & the *Kepler* team. 2011, ArXiv e-prints
- Howard, A. W., et al. 2010, Science, 330, 653
- . 2012, ApJS, 201, 15
- Howell, S. B., Everett, M. E., Sherry, W., Horch, E., & Ciardi, D. R. 2011, AJ, 142, 19
- Huber, D., et al. 2013, ArXiv e-prints
- Ida, S., & Lin, D. N. C. 2010, ApJ, 719, 810
- Isaacson, H., & Fischer, D. 2010, ApJ, 725, 875
- Jenkins, J. M., et al. 2010a, ApJ, 713, L120
- . 2010b, ApJ, 713, L87
- Johnson, J. A., Butler, R. P., Marcy, G. W., Fischer, D. A., Vogt, S. S., Wright, J. T., & Peek, K. M. G. 2007, ApJ, 670, 833
- Johnson, J. A., Howard, A. W., Bowler, B. P., Henry, G. W., Marcy, G. W., Wright, J. T., Fischer, D. A., & Isaacson, H. 2010, PASP, 122, 701
- Kolbl, R., & Marcy, G. 2013, ArXiv e-prints
- Latham, D. W., & Buchhave, L. A. 2012, in American Astronomical Society Meeting Abstracts, Vol. 220, American Astronomical Society Meeting Abstracts #220, 306.03
- Lawrence, A., et al. 2007, MNRAS, 379, 1599
- Lissauer, J. J., et al. 2012, ApJ, 750, 112
- . 2013, ArXiv e-prints
- Lopez, E. D., Fortney, J. J., & Miller, N. 2012, ApJ, 761, 59
- Mandel, K., & Agol, E. 2002, ApJ, 580, L171
- Maness, H. L., Marcy, G. W., Ford, E. B., Hauschildt, P. H., Shreve, A. T., Basri, G. B., Butler, R. P., & Vogt, S. S. 2007, PASP, 119, 90
- Marcy, G. W., & Butler, R. P. 1992a, PASP, 104, 270
- . 1992b, PASP, 104, 270
- Marcy, G. W., et al. 2008, Physica Scripta Volume T, 130, 014001
- Mayor, M., et al. 2011, ArXiv e-prints
- Morbidelli, A. 2013, Dynamical Evolution of Planetary Systems, ed. T. D. Oswalt, L. M. French, & P. Kalas, 63
- Mordasini, C., Alibert, Y., Klahr, H., & Henning, T. 2012, A&A, 547, A111
- Morton, T. D. 2012, ApJ, 761, 6
- Morton, T. D., & Johnson, J. A. 2011, ApJ, 738, 170
- Muirhead, P. S., Hamren, K., Schlawin, E., Rojas-Ayala, B., Covey, K. R., & Lloyd, J. P. 2012, ApJ, 750, L37
- Petigura, E., Marcy, G. W., & Howard, A. 2013, in American Astronomical Society Meeting Abstracts, Vol. 221, American Astronomical Society Meeting Abstracts, 216.05
- Queloz, D., et al. 2009, A&A, 506, 303
- Rogers, L. A., Bodenheimer, P., Lissauer, J. J., & Seager, S. 2011, ApJ, 738, 59
- Rogers, L. A., & Seager, S. 2010a, ApJ, 712, 974
- . 2010b, ApJ, 716, 1208
- Santerne, A., et al. 2012, A&A, 545, A76
- Seager, S., Kuchner, M., Hier-Majumder, C. A., & Militzer, B. 2007, ApJ, 669, 1279
- Steffen, J. H., et al. 2012, MNRAS, 421, 2342
- . 2013, MNRAS, 428, 1077
- Torres, G., Fischer, D. A., Sozzetti, A., Buchhave, L. A., Winn, J. N., Holman, M. J., & Carter, J. A. 2012, ApJ, 757, 161
- Torres, G., Winn, J. N., & Holman, M. J. 2008, ApJ, 677, 1324
- Torres, G., et al. 2011, ApJ, 727, 24
- Troy, M., & Chanian, G. 2003, Appl. Opt., 42, 3745
- Valenti, J. A., & Fischer, D. A. 2005, ApJS, 159, 141
- Valenti, J. A., & Piskunov, N. 1996, A&AS, 118, 595
- Van Cleve, J. E., & Caldwell, D. A. 2009, Kepler Instrument Handbook (KSCI-19033).
- Weiss, L. M., et al. 2013, ArXiv e-prints
- Wu, H., et al. 2010, in Society of Photo-Optical Instrumentation Engineers (SPIE) Conference Series, Vol. 7740, Society of Photo-Optical Instrumentation Engineers (SPIE) Conference Series
- Wu, Y., & Lithwick, Y. 2012, ArXiv e-prints
- Wurm, G., Trieloff, M., & Rauer, H. 2013, ArXiv e-prints
- Yi, S., Demarque, P., Kim, Y.-C., Lee, Y.-W., Ree, C. H., Lejeune, T., & Barnes, S. 2001, ApJS, 136, 417
- Zeng, L., & Sasselov, D. D. 2013, ArXiv e-prints
- Zeng, L., & Seager, S. 2008, PASP, 120, 983